


# PRODUCTION OF CEMENTED TUNGSTEN CARBIDE ALLOYS USING ZINC RECYCLED TUNGSTEN CARBIDE TOOL GRADE SCRAP METAL

Jaquiline Tatenda Kurasha

A dissertation submitted to the Faculty of Engineering and the Built Environment, University of the Witwatersrand, Johannesburg, in fulfilment of the requirements for the degree of Masters of Science in Engineering.

Johannesburg, 2017

## DECLARATION

I declare that this dissertation is my own unaided work. It is being submitted to the Degree of Master of Science in Engineering to the University of the Witwatersrand, Johannesburg. It has not been submitted before for any degree or examination to any other university.

……...

Jaquiline Tatenda Kurasha

……. day of……..year……

**ABSTRACT**

This dissertation presents the zinc recycling of tool grade cemented tungsten scrap material generated during commercial production at Pilot Tools Pty Ltd (South Africa), production of powders and alloys from the zinc recycled materials, and evaluation of the properties of the recycled and un-recycled powders and alloys. Tool grade cemented tungsten carbide inserts were subjected to the zinc recycled process under controlled conditions. Tungsten carbide, cubic (TiC, TaC, NbC, TiCN) carbides and Co were recovered from the recycled scrap material. Two recycled alloys, R and RA, and two un-recycled alloys NS and N were produced following the conventional powder metallurgy route. Alloy R was made from 100 % zinc recycled powder with stoichiometric adjustment of C only, and alloy RA was made from 100% zinc recycled powder with stoichiometric adjustment of C and Co. Alloy N was produced under the same conditions as the recycled alloys R and RA, while alloy NS was produced at commercial level at Pilot Tools Pty Ltd (South Africa) using un-recycled powders. The alloy properties were evaluated following standard procedures for hardmetals. When the zinc recycled material was mechanically disintegrated, about 70 % of the recycled material was recovered as fine powder, while 30% was recovered as coarse oversize particles. The oversize particles were quite tough due to a high Co content, and it was difficult to disintegrate them through milling or repeated zinc recycling. The recycled powders took twice as much time to mill to the desired size as the new un-recycled powders, and had predominantly angular particles, while the new powders had smaller more rounded particles. A cubic free layer (CFL) was formed in all the alloys during sintering, although the recycled alloys R and RA had a narrower CFL compared to the new alloys NS and N. The recycled alloys R and RA had carbide grain size, carbide contiguity, binder mean free path, hardness, fracture toughness and wear rate which were generally within the same ranges as the new un-recycled alloys.

## DEDICATION

This work is dedicated to the loving memory of my late father, Mr Leonard Madzimure, my mother Mrs Phelis Madzimure, my husband Sheuneni Kurasha, and my two sons Nyasha and Ndinashe, who supported me throughout my years of study.

**ACKNOWLEDGEMENTS**

My sincere gratitude is extended to:

- **Associate Prof. Natasha Sacks**, for suggesting the project, and patiently supervising, mentoring, and advising me throughout the research project.
- **Pilot Tools (Pty) Ltd**, for providing the scrap material, the zinc recycling equipment, powders and the majority of the equipment used for the characterisation work. Special mention goes to Dr. C.S. Freemantle, Mr. Jaco, and all the laboratory staff (Ms. Amanda Mtonjeni, Ms. Shumani Magaba, Ms Boipelo Phete and Mr. Tshepo Tshoma).
- **iThemba Labs, Somerset West, South Africa**, for providing equipment, assistance and guidance on all the micro-PIXE test work. Special mention goes to Dr. M. Topic, Prof. C. Pineda-Vargas and Dr. C. Mtshali.
- **DST-NRF Centre of Excellence in Strong Materials, South Africa** for supporting me financially for my research and providing a bursary.
- **School of Chemical and Metallurgical Engineering, University of the Witwatersrand** for affording me the opportunity to study, and Postgraduate students Ms. Fortunate Moyo and Ms. Dineo Lioma as well as the rest of the Postgraduate students from the 7th Floor Postgraduate Office for all their support and friendship.
- **My Family;** Husband, Mr. Sheuneni Kurasha, and our two boys Nyasha and Ndinashe for their unwavering support throughout my studies, and my sister Mrs. Joyline Mawunze**,** for holding fort while I was away from home.

**TABLE OF CONTENTS**

DECLARATION…….....i

ABSTRACT ……..ii

DEDICATION……iii

ACKNOWLEDGEMENTS……iv

TABLE OF CONTENTS…….v

LIST OF FIGURES……....xi

LIST OF TABLES……...xvii

LIST OF SYMBLOYS…….xix

**1 Introduction……1**

1.1 Aims and objectives of the research……3

1.2 Structure of the dissertation..……..3

**2 Literature review…….....5**

2.1 Cemented tungsten carbide grades……..5

2.1.1 Straight grade cemented tungsten carbides……..5

2.1.2 Tool grade cemented tungsten carbides……...6

2.2 Production of cemented tungsten carbide……8

2.2.1 Milling…….8

2.2.2 Granulation……..9

2.2.3 Consolidation……..9

2.2.4 Dewaxing……...10

2.2.5 Pre-sintering……...10

2.2.6 Sintering……10

2.2.6.1 Solid state sintering……10

2.2.6.2 Liquid phase sintering……11

2.3 Cemented tungsten carbide recycling……12

2.3.1 Zinc recycling process……13

2.3.2 Cold stream process…….....14

2.3.3 Chemical recycling processes……15

2.4 Properties of cemented tungsten carbides…….16

2.4.1 Microstructural properties……..16

2.4.1.1 Major phases……..16

2.4.1.2 Eta (η) phase…….....17

2.4.1.3 Carbide grain size…….....18

2.4.1.4 Carbide contiguity……..18

2.4.1.5 Binder mean free path…….....19

2.4.2 Physical and mechanical properties……...19

2.4.2.1 Hardness…….19

2.4.2.2 Fracture toughness…….20

2.4.3 Magnetic properties……21

2.4.3.1 Coercive force ($H_c$)……21

2.4.3.2 Magnetic saturation (CoM)……21

2.4.4 Effects of trace elements.....22

2.4.5 Abrasive wear resistance...…….23

**3 Experimental Procedure……..26**

3.1 Introduction……26

3.2 Zinc recycling…….26

3.3 Processing of recycled inserts…….....27

3.4 Processing of the oversize materials……..27

3.4.1 Milling……27

3.4.2 Vickers hardness……28

3.4.3 Scanning Electron Microscope (SEM) analysis…….……28

3.4.4 Micro-Proton Induced X-ray Emission (PIXE) analysis……...28

3.4.5 Zinc recycling of oversize materials……..29

3.5 Processing of the recycled powder…….....29

3.5.1 Inductively Coupled Plasma-Optical Emission Spectrometry……...29

3.5.2 Powder stoichiometric adjustments……30

3.6 Benchmark powders……...31

3.7 Powder characterization…….....31

3.7.1 Chemical analysis……...31

3.7.2 Powder morphology and phase analyses……....32

3.8 Powder compaction and sintering……..32

3.9 Characterization of sintered alloys…….33

3.9.1 Percentage shrinkage……..33

3.9.2 Density and porosity……..……34

3.9.3 Magnetic properties ……...……35

3.9.3.1 Magnetic Saturation (CoM)……...35

3.9.3.2 Coercivity ($H_c$)……...35

3.9.4 Sample preparation…….36

3.9.5 Microstructural analysis..……..……..37

3.9.5.1 Optical microscopy……..……..37

3.9.5.2 Carbide grain size ($d_c$)……37

3.9.5.3 Carbide contiguity (C)……38

3.9.5.4 Binder mean free path ($\lambda_{Co}$)……...38

3.9.6 Elemental and phase analysis…….39

3.9.7 Mechanical properties…….....39

3.9.7.1 Vickers Hardness…….....39

3.9.7.2 Rockwell hardness…….40

3.9.7.3 Fracture toughness…….40

3.9.7.4 Slurry abrasion tests...……41

**4 Results……...44**

4.1 Introduction……44

4.2 Zinc recycling…….44

4.3 Recycled oversize particles characterization……46

4.4 Recycled powder characterization…….54

4.4.1 Green density of compacted powders……74

4.5 Characterization of sintered alloys…….74

4.5.1 Microstructural characterization……75

4.5.2. Physical properties…….88

4.5.3 Mechanical properties…….....89

**5 Discussion……101**

5.1 Introduction…….....101

5.2 Zinc recycling……...101

5.3 Powder characterization……...102

5.4 Sintered alloy characterization…….105

**6 Conclusions……112**

6.1 Zinc recycling……...112

6.2 Comparison of recycled and un-recycled powders……..112

6.4 Characterization of sintered alloys……...113

**7 Recommendations……..…114**

**References……...115**

**Appendices……..124**

Appendix A: Characterization of recycled oversize particles……..124

Appendix B: Particle size distribution of milled powders……...126

Appendix C: Characterization of green compacts……...127

Appendix D: Characterization of sintered samples…….128

Appendix E: Silica sand characterization……131

Appendix F: Raw data of mass loss in slurry abrasion tests……....133

## LIST OF FIGURES

**Figure 2.1** Influence of TiC and TaC on the high temperature transverse rupture strength of WC-10 wt% Co cemented carbides [**7**] ……..…….7

**Figure 2.2** The zinc recycling process flow sheet [**31, 34**]……...14

**Figure 2.3** Schematic diagram of two-body and three-body abrasive wear [**62**]…….24

**Figure 3.1** Tool grade inserts in a graphite crucible……..……...26

**Figure 3.2** Crack geometry of Palmqvist cracks [**75**]……....41

**Figure 3.3** (a) Slurry abrasion test rig and (b) schematic diagram of the slurry abrasion test rig [**72**]. In both (a) and (b), A is the pump, B is the rubber lined cylinder, C is the loading arm and D (not shown in (a)) is the test specimen……....43

**Figure 4.1** (a) Optical image of tool grade insert(i) before recycling and (ii) after recycling, showing an increase in volume and peeling of the surface layer. (b) FESEM micrograph of the insert after zinc recycling showing different layers from the surface (left) into the inner (right) section……44

**Figure 4.2** SEM micrographs of the (a) un-recycled insert, in which the grey WC, light grey mixed crystals, and the dark Co phases are distinct, and (b) the recycled material in which only the grey WC phase is distinct (the light grey areas are as a result of smeared powder particles during light grinding)…….45

**Figure 4.3** Optical images of (a) oversize particles and (b) tool grade insert before recycling (left) and after recycling (right). The oversize particles were predominantly from the surface layer of the inserts, as shown by bevels and grooves on the oversize particles…….46

**Figure 4.4** FESEM micrograph of oversize particle, showing agglomerated carbide particles…….47

**Figure 4.5** (a) FESEM micrograph of oversize particle, and FESEM elemental distribution maps of (b) $W_L$, (c) Co, (d) Ti, (e) Fe, (f) C, (g) $Ta_L$ and (h) Nb. All elements except Ti are generally evenly distributed…..……48

**Figure 4.6** (a) SEM micrograph of oversize particle. Micro-PIXE elemental distribution maps of (b) $W_L$, (c) Co, (d) Ti, (e) $Ta_L$ and (f) Nb. Yellow areas indicate regions of high concentration, and blue to dark areas show regions of low concentration of a given element.....50

**Figure 4.7** Material from the second zinc recycling session, showing a shiny outer layer and a dark core……51

**Figure 4.8** FESEM micrograph of the material subjected to a second recycling session, showing (A) light grey WC phase, (B) dark grey Co binder phase, and the (C) pores……52

**Figure 4.9** Micro-PIXE elemental distribution maps of (a) $W_L$, (b) Co, (c) Ti, (d) Fe, and (e) Zn. Yellow areas indicate regions of high concentration, and dark areas indicate regions of low concentration……..55

**Figure 4.10** (a) FESEM micrograph of material subjected to second recycling process, and FESEM elemental distribution maps of (b) $W_L$, (c) Co, (d) Ti, (e) $Ta_L$, (Nb, (g) C (h) Fe and (i) O. The material appears as if it was sintered, and concentration of Co in the material is quite apparent……...54

**Figure 4.11** Morphology of the recycled powder showing a wide particle size distribution of angular grains……..55

**Figure 4.12** Milling curves of powders (a) N, (b) R and (c) RA, showing longer milling times for the recycled powders R and RA compared to the virgin powder N……58

**Figure 4.13A** Particle size distribution of the virgin powders (a) NS and (b) N……59

**Figure 4.13B** Particle size distribution the zinc recycled powders (a) R and (b) RA……60

**Figure 4.14** Morphology of un-recycled powders (a) NS and (b) N showing isolated large angular particle, and recycled powders (c) R and (d) RA, showing predominantly large angular particles……62

**Figure 4.15** XRD plots of the powders showing WC, TiC, Co and FeO peaks……63

**Figure 4.16** Micro-PIXE elemental distribution maps on a 2.3 mm x 2.3 mm area in the virgin powder NS, showing the major elements (a) $W_L$, (b) Co, (c) Ti, (d) $Ta_L$ and (e) Nb, and impurities (f) Fe, (g) S, (h) Cr, (i) Mn, (j) Ca, (k) K and (l) Cl. Yellow areas indicate regions of high concentration and dark areas indicate region of low concentration of a given element……65

**Figure 4.17** Micro-PIXE elemental distribution maps on a 2.3 mm x 2.3 mm area in the virgin powder N, showing the major elements (a) $W_L$, (b) Co, (c) Ti, (d) $Ta_L$ and (e) Nb, and impurities (f) Fe, (g) S, (h) Cr, (i) Mn, (j) Ni and (k) Ca. Yellow areas indicate regions of high concentration and dark areas indicate region of low concentration of a given element……..66

**Figure 4.18** Micro-PIXE elemental distribution maps on a 2.3 mm x 2.3 mm area in the recycled powder R, showing the major elements (a) $W_L$, (b) Co, (c) Ti, (d) $Ta_L$ and (e) Nb, and impurities (f) Fe, (g) S, (h) Cr, (i) Mn, (j) Ni and (k) Ca and (l) Cl. Yellow areas indicate regions of high concentration and dark areas indicate region of low concentration of a given element……67

**Figure 4.19** Micro-PIXE elemental distribution maps on a 2.3 mm x 2.3 mm area in the recycled powder RA, showing the major elements (a) $W_L$, (b) Co, (c) Ti, (d) $Ta_L$ and (e) Nb, and impurities (f) Fe, (g) S, (h) Cr, (i) Mn, (j) Ni and (k) Ca and

(l) Zn. Yellow areas indicate regions of high concentration and dark areas indicate region of low concentration of a given element…….68

**Figure 4.20** Micro-PIXE elemental distribution maps on a 86 μm x 86 μm area in the virgin powder NS, showing the major elements (a) $W_L$, (b) Co, (c) Ti, (d) $Ta_L$ and (e) Nb, and impurities (f) Fe, (g) S, (h) Cr, (i) Mn, (j) Ni, (k) K and (l) Ca. Yellow areas indicate regions of high concentration and dark areas indicate region of low concentration of a given element……70

**Figure 4.21** Micro-PIXE elemental distribution maps on a 86 μm x 46 μm area in the virgin powder N, showing the major elements (a) $W_L$, (b) Co, (c) Ti, (d) $Ta_L$ and (e) Nb, and impurities (f) Fe, (g) S, (h) Cr, (i) Mn and (j) Ni. Yellow areas indicate regions of high concentration and dark areas indicate region of low concentration of a given element……..71

**Figure 4.22** Micro-PIXE elemental distribution maps on a 86 μm x 86 μm area in the recycled powder R, showing the major elements (a) $W_L$, (b) Co, (c) Ti, (d) $Ta_L$ and (e) Nb, and impurities (f) Fe, (g) S, (h) Cr, (i) Mn, (j) Ni and (k) K and (l) Ca. Yellow areas indicate regions of high concentration and dark areas indicate region of low concentration of a given element……72

**Figure 4.23** Micro-PIXE elemental distribution maps on a 86 μm x 61 μm area in the recycled powder RA, showing the major elements (a) $W_L$, (b) Co, (c) Ti, (d) $Ta_L$ and (e) Nb, and impurities (f) Fe, (g) S, (h) Cr, (i) Mn, (j) Ni and (k) Zn. Yellow areas indicate regions of high concentration and dark areas indicate regions of low concentration of a given element……...73

**Figure 4.24** FESEM micrographs of (a) NS, (b) N, (c) R and (d) RA, showing the light WC phase and the dark Co binder……75

**Figure 4.25** FESEM micrographs showing the cubic free layer in (a) NS, (b) N, (c) R and (d) RA. The arrows indicate the thickness of the cubic free layer in each sample……77

**Figure 4.26** XRD patterns for alloys NS, N, R and RA showing the WC, TiC and Co peaks…….78

**Figure 4.27 (**a) Optical micrograph of alloy NS, and PIXE distribution maps of major elements (b) Tungsten ‘L’ ($W_L$), (c) Co, (d) Ti, (e) Tantalum ‘L’ ($Ta_L$), and

(f) Nb, and impurities (g) Fe, (h) Cr, (i) Mn, (j) Ni and (k) S. Yellow areas indicate regions of high concentration and dark areas indicate regions of low concentration of a given element……...81

**Figure 4.28 (**a) Optical micrograph of alloy N, and PIXE distribution maps of major elements (b) Tungsten 'L' ($W_L$), (c) Co, (d) Ti, (e) Tantalum 'L' ($Ta_L$), and (f) Nb, and impurities (g) Fe, (h) Cr, (i) Mn, (j) Ni and (k) S. Yellow areas indicate regions of high concentration and dark areas indicate regions of low concentration of a given element……...82

**Figure 4.29 (**a) Optical micrograph of alloy R, and PIXE distribution maps of major elements (b) Tungsten 'L' ($W_L$), (c) Co, (d) Ti, (e) Tantalum 'L' ($Ta_L$), and(f) Nb, and impurities (g) Fe, (h) Cr, (i) Mn, (j) Ni, (k) S and (l) Zn. Yellow areas indicate regions of high concentration and dark areas indicate regions of low concentration of a given element……..83

**Figure 4.30 (**a) Optical micrograph of alloy RA, and PIXE distribution maps of (b) Tungsten 'L' ($W_L$), (c) Co, (d) Ti, (e) Tantalum 'L' ($Ta_L$), (f) Nb, (g) Fe, (h) Cr, (i) Mn, (j) Ni, (k) S and (l) Zn. Yellow areas indicate regions of high concentration and dark areas indicate regions of low concentration of a given element……..84

**Figure 4.31** PIXE analysis of selected points on Ti maps, 1: in the CFL, 2: just below the CFL 3 and 4: into the bulk. Image sequence is (a) selected points in alloy NS, (b) selected points in alloy N, (c) selected points in alloy R, and (d) selected points in alloy RA……85

**Figure 4.32** Plot of Co and Ti contents from the CFL (origin) into the bulk (right), showing an inverse linear relationship between the Co and Ti contents moving from the CFL to just below the CFL…….86

**Figure 4.33** Cumulative mass during slurry abrasion test……91

**Figure 4.34** Variation of wear rate during slurry abrasion test…….92

**Figure 4.35** Average wear rates of the alloys……93

**Figure 4.36** FESEM images of wear scars of unrecycled alloys (a) NS and (b) N, and recycled alloys (c) R and (d) RA (100x) after slurry abrasion test. Alloys N and RA show more wear compared to NS and R……..94

**Figure 4.37** FESEM images of wear scars after slurry abrasion test of un-recycled alloy NS showing (a) general loss of surface material (100x), (b) small groves from ductile binder displacement (2000x), (c) micro-polishing of large WC grains (5000x), (d) WC grain pull-out (10000x) (e) carbide grain disintegration (20000x), and (f) micro-cracking of WC grains (20000x)……95

**Figure 4.38** FESEM wear scars after slurry abrasion test of un-recycled alloy N showing (a) general loss of surface material (100x), (b) pits as a result of grain pull-out (2000x), (c) carbide grain disintegration (5000x), (d) micro-cracking of carbide grains (10000x) (e) micro-polishing of carbide grains (20000x), and (f) carbide grain pull-out (20000x)…….96

**Figure 4.39** FESEM images of wear scars after slurry abrasion test of recycled alloy R showing (a) general loss of surface material (100x), (b) small grooves from ductile binder displacement (2000x), (c) small pits from material displacement (5000x), (d) micro-polishing of carbide grains (10000x), (e) micro-cracking of carbide grains (15000x), and (f) carbide grain pull-out (20000x)…….97

**Figure 4.40** FESEM images of wear scars after slurry abrasion test of recycled alloy RA showing (a) general loss of surface material (100x), (b) pits from material displacement (2000x), (c) carbide grain pull-out (5000x), (d) carbide grain disintegration (10000x), (e) carbide grain fragments (10000x), and (f) micro-cracking of carbide grains (20000x)……98

**Figure 4.41** FESEM micrographs of the cross sections of the worn surfaces after slurry abrasion of (a) NS, (b) N, (c) R and (d) RA. The micrographs show grain pull-out and binder removal during slurry abrasion……..99

**LIST OF TABLES**

**Table 2.1** Physical and mechanical properties of selected hardmetals [**13**]……..20

**Table 2.2** Occurrence of trace elements in cemented carbides [**53**]……..22

**Table 3.1** Grinding and polishing procedure…….36

**Table 3.2** Slurry abrasion test parameters…….42

**Table 4.1** EDS analysis results for recycled and un-recycled insert…….45

**Table 4.2** EDS and micro-PIXE analysis results for oversize particles……49

**Table 4.3** EDS analysis of the material subjected to a second recycling process……52

**Table 4.4** ICP-OES analysis of recycled powder…….....56

**Table 4.5** Milling data for powders N, R and RA……..57

**Table 4.6** $D_{10}$, $D_{50}$ and $D_{90}$ values for the milled powders……60

**Table 4.7** ICP-OES Analysis results for the powders...……61

**Table 4.8** EDS analysis results for the powders……63

**Table 4.9** Micro-PIXE elemental analysis of powders…….64

**Table 4.10** Green densities of compacted powders……...74

**Table 4.11** EDS analysis of sintered alloys……...76

**Table 4.12** CFL width and EDS analysis results……...77

**Table 4.13** Mean carbide grain size, carbide contiguity and binder mean free path of sintered alloys……79

**Table 4.14** Cobalt and titanium content in the CFL (point 1) and just below the CFL (point 2) respectively……..……...86

**Table 4.15** Micro-PIXE elemental composition of the alloys……...87

**Table 4.16** Physical properties of sintered alloys……..89

**Table 4.17** Hardness and fracture toughness values for the sintered alloys……..90

**Table 4.18** EDS analysis comparison on the surface of the alloys before and after slurry abrasion……..100

**LIST OF SYMBOLS**

| | | |
|---|---|---|
| FESEM | - | Field Emission Scanning Electron Microscope |
| EDS | - | Energy Dispersive X-Ray Spectroscopy |
| BSE | - | Back Scattered Electrons, |
| PIXE | - | Proton Induced X-ray Emission |
| XRD | - | X-Ray Diffraction |
| ICP-OES | - | Inductively Couple Plasma Optical Emission Spectroscopy |
| $K_{IC}$ | - | Fracture toughness |
| HV | - | Vickers Hardness |
| $H_c$ | - | Coercivity |
| CoM | - | Magnetic cobalt (Magnetic Saturation) |
| hr(s) | - | Hours |
| min(s) | - | Minute(s) |
| μm | - | Micron |
| wt% | - | Weight per cent |
| °C | - | degrees Celsius |
| KPa | - | Kilo Pascals |
| MeV | - | milli-electron volts |
| pA | - | pico-amperes. |

# 1 Introduction

Tungsten carbide-cobalt (WC-Co) based materials, also known as hardmetals, are widely used as cutting tools and drill bit inserts in the mining and manufacturing industries. In many of these applications, the WC-Co alloys will contain small additions of carbides such as TiC, TaC and NbC to improve machinability of steels [1]. These types of alloys are commonly known as 'tool grade' cemented carbides. According to the 2016 US Geological Survey [2], cobalt production exceeds its consumption, resulting in market surplus and price reduction. However, the same cannot be said for the world tungsten reserves, which are expected to be exhausted in less than 40 years [3]. Hence there is a critical need to develop and optimize the recycling of tungsten carbide scrap metal products, to produce the tungsten required to sustain the industrial demand for cemented carbide cutting tools.

At least two classes of hardmetal scrap exist, namely, scrap that is generated once the cutting tool has either failed in service or reached the end of its lifespan, and scrap that is generated during the production of the cutting tools. In the second category, it is possible for large quantities of tools to be rejected during production, for example, due to incorrect dimensional tolerances or cracks. Since this class of scrap materials will not generate any income to offset the production costs, companies may be able to recover some of these costs by recycling the scrapped materials and then incorporating them back into the production line. In the current research project, recycling of the second class of scrap material was investigated.

There are several methods, direct and indirect, which can be employed in cemented tungsten carbide recycling. Direct recycling methods transform the scrap directly into a product of commercial value, which can be re-used in

production. Zinc recycling and cold stream process are examples of direct recycling methods [4, 5]. Indirect methods involve chemical modification of the cemented tungsten carbide scrap, producing a compound that is in a different form, for example, an oxide. Chemical recycling processes fall under this method [6]. All recycling methods are hinged on stringent environmental and conservation policies, which demand recycling techniques that are economically viable and ecologically friendly. Direct recycling methods do not use any chemicals or water solutions, and generally consume less energy than indirect recycling methods [5]. All components are typically recovered and can be reused without any waste products [4]. The recovery rate for the zinc recycling process, a direct recycling method, is quite high, and is currently deemed to be the most successful recycling method for the tungsten carbide industry [7].

In this research project, the recovery of tungsten, cubic (TiC, TaC, NbC) carbides and cobalt from cemented carbide tool grade scrap material using the zinc recycling process was explored. The recovered material was reused as raw material in the production of tool grade alloys. In typical industrial applications, commercial products are produced using powder blends comprising at most 50-70% recycled powders [6]. In this study, the alloys were produced using 100% recycled powders to assess commercial production possibilities. The powders and alloys produced from the recycled materials were characterized and compared to powders and alloys produced from new materials in order to determine the success of the zinc recycling process. To the author's knowledge, this was the first time that the zinc recycling process was applied to this specific tool grade scrap material, and the first time that sintered alloys were produced using 100% recycled powders. Therefore, this study, based on the proposed methodology, was expected to make the following contributions to scientific knowledge:

- Provide new information to contribute to the knowledge base on the recycling of tungsten carbide tool grade materials.

- Provide an avenue for financial savings for companies if the recycling process can be successfully applied to the production scrap.

## 1.1 Aims and objectives of the research

The aim of this research was to produce commercially suitable tungsten carbide tool grade alloys using 100% zinc recycled powders recovered from tool grade scrap metal. This aim was achieved through the following objectives:

- Applying the zinc recycling process to tool grade cemented carbide scrap metal to recover tungsten, cobalt and mixed crystal (TiC, TaC, NbC) carbide powders.
- Characterizing the recycled carbide powders and comparing the properties to those of new, un-recycled carbide powders.
- Manufacturing sintered tool grade alloys using the recycled and new powders.
- Characterizing and comparing the sintered recycled and unrecycled tool grade alloys in terms of microstructure, physical, magnetic, mechanical and wear properties.

## .2 Structure of the dissertation

This dissertation is structured as follows: Chapter 1 presents and explains the background and significance of the research work undertaken. Chapter 2 reviews published literature on cemented tungsten carbide recycling, with particular attention being paid to the zinc recycling process, cemented tungsten carbide production, and the material properties of hardmetals. The materials, equipment and experimental procedures followed to recover the tool grade constituent

materials from the zinc recycling process, to produce alloys from recycled and un-recycled powders, and to evaluate the various material properties are presented in Chapter 3. Chapter 4 presents the test results and analyses, which are then discussed in Chapter 5. The conclusions drawn from the research work are presented in Chapter 6, while Chapter 7 provides the recommendations for future work. The final sections provide a list of all cited references, and the relevant appendices.

# 2 LITERATURE REVIEW

This chapter reviews the grades of cemented tungsten carbides, the production and recycling processes of these materials, as well as the physical, mechanical and wear properties of the alloys. Particular attention will be paid to the zinc recycling process as it was employed in the current research project.

## 2.1 Cemented tungsten carbide grades

Cemented tungsten carbides, also known as hardmetals, are a group of hard, wear resistant, refractory materials in which the hard, strong carbide particles (WC, TiC, TaC, NbC) are cemented together by a tough, ductile binder (Co, Ni, Fe) [7]. The resultant combination of hardness and toughness makes cemented carbides ideal materials for rock drilling inserts, metal cutting tools, and wear resistant parts such as wire drawing dies [8-10]. Generally, hardmetals can be classified into two broad classes, namely straight grades and tool grades; the latter being the subject of investigation in the current project [11].

### 2.1.1 Straight grade cemented tungsten carbides

Straight grade cemented carbides mainly consist of two phases, WC and Co, where the cobalt content varies from 3 to 13 wt% for cutting applications, and can be as high as 30 wt% in wear resistant parts [11]. The average carbide grain size in straight grades varies from sub-micron to 30 μm. Alternative binder materials can be found from the iron group metals, particularly nickel and iron, or a combination of these metals, and are typically used for corrosion resistant alloys [7]. Straight grade cemented carbides are also often referred to as un-alloyed grades, cast iron cutting grades, or edge-wear resistant grades [11].

### 2.1.2 Tool grade cemented tungsten carbides

Tool grade cemented carbides derive their name from the fact that they are mainly used for cutting tool applications. To produce tool grade alloys, straight grade WC-Co alloys are modified by the addition of cubic carbides of titanium, tantalum, niobium, chromium, vanadium and molybdenum [11]. Such additions produce various hardmetals which have improved high temperature properties like oxidation resistance, hot hardness, hot strength and diffusion resistance against iron alloys [7, 11]. These superior properties have made tool grade cemented carbides successful in the cutting tools industry.

The microstructure of the tool grade alloys consists of three phases, the hexagonal WC (α phase), cubic mixed crystal carbides (γ phase), and a binder (β phase). Research has shown that the formation of the γ phase during sintering occurs through the reactions below [7]:

$$TiC + (Ta, Nb)C + WC \longrightarrow \gamma\,[(Ti, Ta, Nb, W)]C \quad \text{(Equation 2.1)}$$

$$(Ti, Ta, Nb, W)C + WC \longrightarrow \gamma\,[(Ti, Ta, Nb, W)]C \quad \text{(Equation 2.2)}$$

$$(Ti, Ta, Nb, W)C \longrightarrow \gamma\,[(Ti, Ta, Nb, W)]C + \alpha\,(WC) \quad \text{(Equation 2.3).}$$

Cubic carbide additions play various roles in hardmetals. Barbatti *et al* [12] found that some cubic carbide additions increase oxidation resistance at high temperatures. Titanium carbide in particular, causes a passivation effect on the surface of the cemented carbide by the formation of $TiO_2$. It also reduces the tendency to weld to chips during machining. However, it has been shown to reduce the room temperature transverse rupture strength [13]. Tantalum carbide increases the room temperature strength [13]. The effect of TiC and TaC additions

on the elevated temperature transverse rupture strength of two cemented carbide grades is shown in Figure 2.1. The figure shows that the transverse rupture strength decreases with increase in the amount of cubic carbide additions (TiC/TaC) as well as increase in temperature. However, the difference in transverse rapture strength for the two alloys narrows at temperatures above 800$^{o}$C.

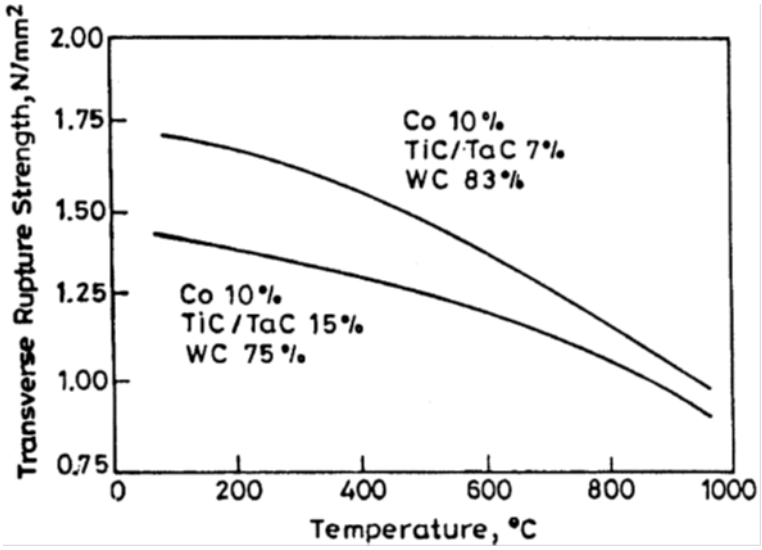



**Figure 2.1** Influence of TiC and TaC on the high temperature transverse rupture strength of WC-10 wt% Co cemented carbides [7].

Cubic carbide additions such as $Cr_2C_3$, VC, TaC and NbC inhibit grain growth during sintering, which results in fine grained cemented carbides with improved strength and hardness [14-17]. Vanadium carbide has been shown to be the most effective grain growth inhibitor, followed by $Cr_3C_2$, NbC and TaC respectively. However, when selecting a grain growth inhibitor, considerations such as corrosion resistance and hot hardness are often considered [18].

Titanium carbonitride can be added to tool grade cemented tungsten carbides to modify the surface layer of cutting inserts, which increases the thermal and chemical stability of the tools during high speed metal cutting [19, 20]. Sintering a TiCN containing cemented tungsten carbide in a vacuum results in a Co-rich tough surface, also known as a Cubic Free Layer (CFL), which extends the lifespan of coated hardmetals due to the increased toughness beneath the coating [19-21]. Decomposition of the nitride or carbonitride in a vacuum sintering atmosphere is believed to promote the thermodynamic coupling of outward diffusion of nitrogen and inward diffusion of Ti, as well as other cubic carbide formers like Ta and Nb. In response to the inward diffusion of Ti as well as the lower affinity for nitrogen, Co and WC diffuse towards the surface layer [19-24]. Because of the superior properties derived from cubic carbide additions, tool grade cemented carbides have found increased use in the cutting tool industry.

## 2.2 Production of cemented tungsten carbide

The general production procedure for cemented tungsten carbide alloys includes milling, granulation, green consolidation, de-waxing, pre-sintering, sintering and post sintering operations. Each of these steps is carefully controlled to produce final products which have the desired microstructure and performance requirements for specific applications [14].

### 2.2.1 Milling

Milling is the initial stage in the production process, and is done with milling binders such as wax or polyethylene glycol (PEG) for lubrication purposes and green strength of powder compacts [7]. Intensive milling is done to crush the initial carbide crystallites to the desired size, and to blend the various components,

such that every carbide particle is adequately coated by the binder material [14, 25]. Milling also ensures the even distribution of the binder material to avoid large binder islands in the sintered product [26]. Carbide mixtures are wet milled using rotary, vibratory or attrition mills, with rotary mills such as ball mills being commonly used [7, 25].

### 2.2.2 Granulation

Granulation is done to coarsen the milled powder to improve the powder apparent density, and to reduce inter-particle friction [7]. This process produces free flowing spherical powder agglomerates. The most common granulation method is spray drying, where hot inert gas impinges on the carbide slurry, resulting in uniform, nearly spherical free flowing powder aggregates [7, 14]. Granulation can also be carried out by pressing the dried powder into billets, which are later disintegrated by applying a light compressive force, to produce coarse granules. A third granulation method makes use of a rotating inclined granulation table, onto which powder is continuously fed and carried upwards to the highest point, after which it moves down the table with a rolling motion [7, 14].

### 2.2.3 Consolidation

Green consolidation provides shape and imparts dimensional control [7]. The green compacts are produced by pressing the loose powder granules into die moulds using external pressure. Compacts are pressed sufficiently to allow for shrinkage during sintering, and subsequent grind-off. Consolidation is facilitated by adding paraffin wax or PEG, which is later removed by de-waxing before sintering.

### 2.2.4 De-waxing

De-waxing is done by volatilization of the paraffin wax or PEG from the compact by the application of heat, above the melting point, but below the decomposition temperature of the lubricant, in hydrogen or in a vacuum [7]. The complex PEG decomposes into CO, $H_2O$, $CO_2$ and $CH_4$.

### 2.2.5 Pre-sintering

Pre-sintering is a heat treatment stage that is done to strengthen compacts for subsequent operations such as machining, drilling, slicing and grinding [25]. This stage is not necessary when components do not require processing before sintering. Some degree of sintering takes place during the pre-sintering stage.

### 2.2.6 Sintering

Full densification of the tungsten carbide compacts is achieved during the sintering process, which largely depends on variables such as the sintering atmosphere, sintering temperature and time, heating and cooling rate, and the presence of impurities [7]. Uphadyaya [7] suggests that the sintering process takes place in two broad stages, namely solid state sintering and liquid state sintering.

#### 2.2.6.1 Solid state sintering

During solid state sintering, more than 50 % densification is achieved below the eutectic temperature of the pseudo-binary WC-Co system [27]. Surface diffusion

of Co and agglomeration of the WC particles occur due to surface tension. As temperatures increase, the open porosity still present in the compact reduces the oxygen levels. At temperatures above 1000 $^{o}$C, finer carbide particles start to dissolve in the binder, and grain growth of coarser WC particles starts at about 1200 $^{o}$C [7]. In Ti containing grades, it was observed that Co diffusion to the carbide surface takes place during solid state sintering [7].

#### 2.2.6.2 Liquid phase sintering

Complete densification is achieved in this stage due to enhanced atomic diffusion in the presence of the liquid phase, and densification is driven by the reduction in surface energy [7]. German [27] suggested that liquid phase sintering takes place in three broad stages. The initial stage involves fluid flow and rearrangement of the carbide particles. Rapid densification takes place due to the capillary force on the solid particles by the liquid soon after liquid formation. According to Kingery [28], 35 wt % liquid is necessary for complete densification.

The second stage involves the solution-precipitation process, where densification is associated with grain shape accommodation via Oswald ripening [27]. Due to smaller liquid content, the solution-precipitation process is slower [29]. Pores are either completely filled, or stabilised by the trapped internal atmosphere. A rigid skeleton is formed, which slows further densification. The final stage is the microstructural coarsening stage, which determines the carbide grain size and distribution, grain shape and binder phase distribution. These microstructural changes influence properties such as wear resistance, strength, fracture toughness and magnetic properties [7]. The rigid skeleton prevents complete pore elimination, and Nelson et al [30] has shown that pores are completely enclosed when 90 % density is reached. If the trapped gas is insoluble, the pores shrink

until a balance between the surface energy and the excess pressure is reached, which then results in a porosity of about 0.2 % [30].

## 2.3 Cemented tungsten carbide recycling

Cemented carbide scrap comes in several forms [7]. These include hard scrap, which is typically worn out cutting tips, buttons, bits, and hot rolls which accumulate from industrial use. Soft scrap is collected from discarded pre-sintered parts, powders collected from the machining of pre-sintered parts, and from parts rejected for various reasons such as cracks, or tools not meeting specifications. This type of scrap is usually directly incorporated back into the production line. The final form of scrap is grinding sludges, dust collector fines, and floor sweepings.

In preparation for recycling, scrap has to be sorted and prepared for the particular recycling process. Ideally, scrap has to be cleaned by removing oil, grease and any other dirt present. Brazing and coatings have to be removed in order to minimize contamination of the recycled material. Sorting into the various commercial carbide grades must also be done to facilitate the recycling process. Some scrap has to undergo size reduction so that a high yield may be attained from the recycling process [7].

There are several methods to reclaim tungsten carbide and cobalt, which are either direct or indirect. Direct recycling methods transform the scrap directly to a product of commercial value, which can be re-used in production [4, 5]. The zinc recycling and cold stream process are direct recycling methods. Indirect methods involve chemical modification of the cemented carbide scrap, producing a compound that is in a different form, for example, an oxide [6]. The binder leach

process, nitrate process, oxidation in molten alkaline medium and the sodium hypochlorite process, are some of the indirect recycling methods [7].

### 2.3.1 Zinc recycling process

In the zinc recycling process, molten zinc is used to treat the carbide scrap by forming a molten intermetallic compound, $CoZn_{13,}$ with the binder material, thereby breaking the bonds between the carbide and the binder. The molten zinc attacks the carbide scrap very rapidly, particularly at temperatures from 750$^{o}$C to 800$^{o}$C and above. The Zn is then distilled from the mixture using a vacuum typically less than 7 KPa, above 800$^{o}$C [3, 31]. The distilled zinc is condensed in the cooler part of the furnace, and complete distillation of the zinc is typically done in about 15 hours [7]. The zinc recycling process enables the recovery of refractory carbides, such as the carbides of tungsten, titanium, tantalum and niobium, as well as the binder material, such as cobalt and nickel in an unaltered state [31]. The product from the zinc recycling process, the carbide matrix and binder material, can be readily ground to the original carbide particle size [32]. The zinc recycling process and parameters are summarised in Figure 2.2, based on information by Barnard *et al* [31]. The zinc recycling process is usually a batch wise process in which several crucibles are loaded with tungsten carbide scrap and molten zinc [33]. Banard *et* al [31] suggests that it is possible to recover most the components in the zinc recycling process.

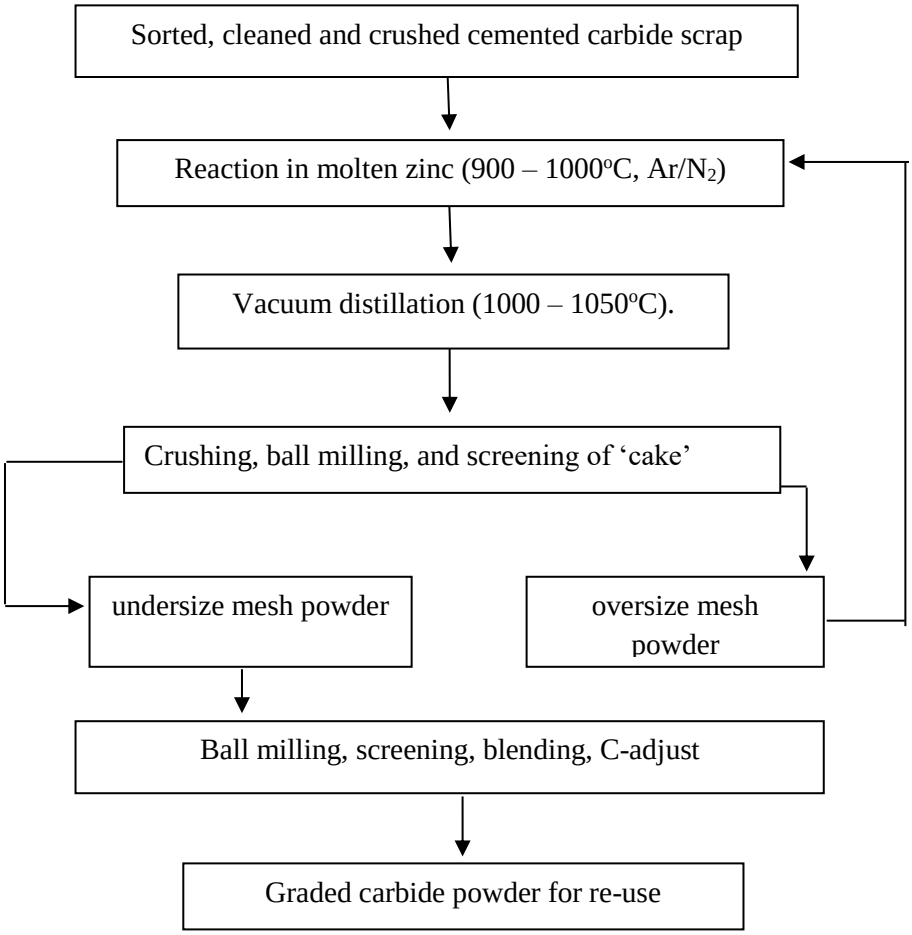



**Figure 2.2** The zinc recycling process flow sheet [31, 34].

### 2.3.2 Cold stream process

The cold stream process is another direct recycling method which recovers the scrap in the original form. It is a purely mechanical method that involves size reduction of the cemented carbide scrap, by injecting the carbide scrap into a high velocity gas stream that directs the particles against a hard target of tungsten carbide [25, 35]. First, the scrap has to be milled to reduce it to a coarse powder, which shatters on impact to progressively reduce the particle size [35]. The powder is taken through a series of classifiers, with the oversize particles taken

back to the blasting chamber. The recovery rate of the cold stream process is about 90 to 92 % [32]. This process does not work well with tough carbides, high in binder content, as they are not easily broken. It also suffers from incomplete carbide separation from the binder material. The product is classified according to size and recycled in order to recover significant amounts of the desired particle size. The resultant product often has oxygen and iron contamination, which contribute to impurities in the powder. Expensive equipment is required for this process [35].

### 2.3.3 Chemical recycling processes

The chemical recycling processes subject the carbide scrap to chemical modification. These processes result in the formation of intermediate products, which are then processed to obtain the pure metals [4]. There are several chemical recycling processes, including the binder leach, nitrate, and sodium hypochlorite processes, and oxidation in a molten alkali medium.

Cemented carbide materials can also be recycled by treatment with a vapour phase mixture of chlorine, carbon monoxide and sulphur gases [35]. There is no limit to the carbide scrap that can be used, and recycled raw material with high purity levels can be produced [3]. Generally, chemical recycling methods are slow, as time is required to break down the chemically unreactive cemented carbide. Special equipment is required to handle the aggressive chemicals and gases, and to recover the dissolved binder [35]. Large quantities of chemicals and energy are used in these processes, which result in environmental challenges pertaining to waste disposal [36]. The processes are profitable when recycling on a large scale [3]. Additionally, some chemical methods are restricted to recycling of sludges and fine material [37, 38].

## 2.4 Properties of cemented tungsten carbides

This section summarises the general microstructural, physical, mechanical, magnetic and wear properties of cemented tungsten carbides.

### 2.4.1 Microstructural properties

The microstructure of cemented tungsten carbide has a direct influence on material properties and engineering performance. Many factors contribute to the microstructure formation in cemented tungsten carbides. These include the basic chemical composition of the various phases, the degree of inter-solubility of carbides, excess or deficiency of carbon, composition variation due to segregation and diffusion, and processing technology [7].

#### 2.4.1.1 Major phases

The WC phase, which is the major phase, exhibits an anisotropic crystal structure, and appears as flat triangular prisms with truncated edges [39]. Deformation of these crystals can occur during milling. Elements such as Mo often result in the shape changing to more irregular acicular and platelet carbide grains [40]. Cubic carbides such as TaC, TiC and NbC have rounded grains, and show a 'cored' structure on etching. The binder phase, usually Co, appears as a continuous thin film that separates the carbide particles, with high Co concentrations at the carbide grain boundaries [41]. Inadequate milling can result in large Co pools in the microstructure, which may cause porosity [42, 43]. Co distribution is also affected by the carbon content, with Co flowing to the low-carbon areas especially during heating to sintering temperatures [44].

Precipitates of non-metallic impurities, graphite, carbides and intermetallic compounds are also often found in the binder phase. In addition, pores can be present in the microstructure of the cemented carbides. Pores can be caused by impurities, inhomogeneity due to insufficient comminution and mixing, and a low carbon content which results in the formation of the brittle eta phase, preventing the binder phase from filling out the carbide skeleton and entrapped gases [7].

#### 2.4.1.2 Eta (η) phase

Carbon deficiency in the WC-Co alloys results in the formation of eta (η) phase, a ternary compound of W, Co and C, which is a brittle phase [7]. There are two forms of eta phase which are indistinguishable physically, namely $M_6C$, which range from $Co_{3.2}W_{2.8}C$ to $Co_2W_4C$ [45] and $M_{12}C$ which has a fixed composition of $Co_6W_6C$ [46]. Extreme carbon deficiency results in the formation of eta phase at the sintering temperature. With minor carbon deficiency levels, eta phase forms on cooling through the reaction shown in equation 2.4:

$$WC + \text{liquid} \longrightarrow WC + \eta + \text{liquid} \qquad \text{(Equation 2.4)}$$

This reaction forms the eta phase in isolated areas, identified by rounded and partially dissolved WC grains, where considerable volumes of WC and the binder phase are locally consumed during the formation of the eta phase [7]. Further cooling may result in the peritectic decomposition of eta phase through the reaction shown in equation 2.5, with the final quantity of eta phase retained at room temperature dependent on the carbon content and the cooling rate [47]. Minor carbon deficiencies may lead to complete disappearance of eta phase, while higher carbon deficiencies result in retained eta phase irrespective of cooling rate [7].

$$\text{Liquid} + \eta \longrightarrow \text{WC} + \beta \qquad \text{(Equation 2.5)}$$

### 2.4.1.3 Carbide grain size

The sintered carbide grain size depends on the powder processing conditions, for example the starting particle size of the WC powder [48]. When the starting particle size is small, milling merely separates the powder aggregates of fine particles, and hence the carbide grain growth kinetics during sintering are slow. For a large starting particle size, milling results in severely fragmented WC particles which have high surface energy, and the carbide grain growth kinetics during sintering are fast [48]. Composition also influences grain growth. For instance, slight increase in the carbon content results in more rapid grain growth [49, 50]. The addition of transition metal carbides such as VC inhibits grain growth.

### 2.4.1.4 Carbide contiguity

Gurland [51] defined contiguity as the fraction of the total internal surface area of a phase that is shared by particles of the same phase. Carbide contiguity is therefore a measure of the degree of contact between carbide grains. By definition, contiguity varies between zero and one. In cemented tungsten carbides, contiguity tends to zero as the Co volume fraction tends to one, and vice versa [52]. Contiguity decreases with binder content because the probability of the spatial coincidence of carbides decreases with an increase in binder content [51].

#### 2.4.1.5 Binder mean free path

Binder mean free path is defined as the measure of the thickness of the binder layer between carbide grains, and is the arithmetic mean of the distance from one carbide-binder interface to the other. It increases with an increase in binder content and carbide grain size [7].

### 2.4.2 Physical and mechanical properties

The physical properties of cemented tungsten carbides combine the physical properties of ceramics and the electronic properties of metals [53]. This results in materials which have high hardness and strength, as well as high thermal and electrical conductivities. Cemented tungsten carbides also have high melting points and high thermal and chemical stability [13]. The mechanical properties of cemented tungsten carbides primarily depend on the cobalt content and carbide grain size. Some of the physical and mechanical properties of selected hardmetals are summarized in Table 2.1, while a brief review of hardness and toughness is also provided.

#### 2.4.2.1 Hardness

Table 2.1 shows the Vickers hardness values for selected cemented carbide alloy compositions. Alloy hardness decreases as the cobalt content increases [32, 53], due to the soft and ductile nature of cobalt. Literature [54] suggests that the hot hardness of cemented tungsten carbides decreases with temperature, although there are some contradictions on the temperature ranges in which the hardness is

significantly compromised. Hardness and compressive strength have been shown to decrease with increasing grain size [18, 32].

**Table 2.1** Physical and mechanical properties of selected hardmetals [13].

| **Composition in wt%** | | | | | |
|---|---|---|---|---|---|
| WC | 94 | 85.3 | 75 | 78.5 | 60 |
| Other carbides (TiC, TaC, NbC) | - | 2.7 | - | 10 | 31 |
| Co | 6 | 12 | 25 | 11.5 | 9 |
| **Properties** | | | | | |
| Density/ $gcm^{-3}$ | 14.9 | 14.2 | 12.9 | 13 | 10.6 |
| Hardness/ $HV_{30}$ | 1580 | 1290 | 780 | 1380 | 1560 |
| Bend Strength/ MPa | 2000 | 2450 | 2900 | 2250 | 1700 |
| Elastic modulus/ GPa | 630 | 580 | 470 | 560 | 520 |
| Fracture toughness/ MPa $m^{1/2}$ | 9.6 | 12.7 | 14.5 | 10.9 | 8.1 |
| Thermal Conductivity/ $Wm^{-1}K^{-1}$ | 80 | 65 | 50 | 60 | 25 |
| Thermal expansion coefficient x $10^{-6}K^{-1}$ | 5.5 | 5.9 | 7.5 | 6.4 | 7.2 |

### 2.4.2.2 Fracture toughness

Fracture toughness is a measure of the material's resistance to crack propagation, and is independent of the specimen size and geometry [7]. There are several methods which can be used to determine fracture toughness, with the Palmqvist method [55] being commonly used for cemented carbides. Fracture toughness increases with increasing binder content, mean carbide grain size and binder mean free path, and decreases with an increase in carbide contiguity. Carbon deficiency results in the formation of the brittle eta phase during sintering, while excess carbon results in free carbon precipitation, and both cases reduce fracture toughness, although the effect is more pronounced in carbon deficient alloys [7].

### 2.4.3 Magnetic properties

Cemented tungsten carbides are ferromagnetic at room temperature due to the presence of ferromagnetic binder materials [7]. Non-destructive quality tests for cemented carbides have been developed based on the magnetic properties of the binder phase, as they provide information about the microstructure.

#### 2.4.3.1 Coercive force ($H_C$)

The coercive force is the strength of the magnetic field which is required to demagnetize a fully magnetized cemented carbide sample [56]. Coercivity decreases with an increase in cobalt content and carbide grain size [57], and increases with an increase in the amount of tungsten [57, 58] and carbon content [59].

#### 2.4.3.2 Magnetic saturation (CoM)

Magnetic saturation (CoM) is the maximum magnetization of cemented carbide that can be achieved when the material is subjected to a strong magnetic field [56]. It is also an indirect measure of the degree to which the binder is saturated with carbon, and decreases with an increase of tungsten in solid solution in the cobalt [56, 58]. Generally, a decrease in magnetic saturation values often indicate the presence of eta phase in the cemented carbide [47].

### 2.4.4 Effects of trace elements

Trace elements may influence the microstructural and mechanical properties of cemented tungsten carbides [53]. During the various production stages, other elements often find their way into the material, where the majority are introduced during the powder processing steps. Arronson [53] investigated the effects of some elements typically found in tungsten carbides, which are listed in Table 2.2.

**Table 2.2** Occurrence of trace elements in cemented carbides [53].

| Occurrence of trace elements in cemented carbide | Typical elements |
|---|---|
| Solid solution in the binder phase | Cr, Mo, Mn, Fe, Ni, platinum group metals, Al, P, Si |
| Solid solution in WC | Mo |
| Cubic MX phase | Ti, Zr, Hf, V, Ta, Cr, Mo, B, N, O |
| Oxides, silicates, phosphates, etc. | Li, Na, K, Ma, Ca, Al, Si, P, O |
| Sulphides | Alkaline and rare earth metals, S |

The first group of elements form solid solutions with the binder phase, and some of these elements have desirable effects, and are therefore added intentionally. Nickel, chromium and the platinum group metals, for instance, improve the corrosion resistance in some applications. Molybdenum is the only element that forms a solid solution in WC, and it promotes grain growth during sintering. Hence its quantities are limited to 0.1 wt% to avoid adverse effects which are associated with undesirable grain growth, such as decrease in hardness and wear resistance [53].

Iron can be present in the carbide in considerable amounts without negatively affecting the carbide properties [53]. Iron and nickel are often introduced during ball milling when using stainless steel vessels and attrition mills. The group of elements which form oxides, silicates, phosphates and sulphides is the one of particular importance. These elements give rise to non-metallic inclusions and porosity, which lower the transverse rapture strength of the carbide alloys [53]. Trace elements such as Ca, Al, and Si often find their way into the carbide powders as residues from ore processing. Non-metallic trace elements such as O, N, and H come from different sources during processing, while S and P often come from the starting raw materials [7]. Sulphur usually originates from carbon black, which is used to carburize the tungsten. Most of these trace elements are concentrated in the binder phase. The silicate and oxygen often result in the formation of CO, which contributes to pore formation as it is partially liberated [7].

### 2.4.5 Abrasive wear resistance

Cemented carbides are used in wear resistant applications such as metal cutting, drilling, blasting and metal forming dies due to their high hardness and wear resistance [51]. In some of these applications, cemented carbides are subjected to wear as a result of contact with hard particles, resulting in abrasion, which is the wear property of interest in the current research study.

Wear by abrasion is the removal or displacement of material by hard particles forced against and sliding along a surface [61]. Abrasive wear can be two-body, where the hard particles are protuberances that act on the counterface, or three-body, where the hard particles roll and slide freely between two sliding surfaces [62]. Figure 2.3 shows the schematic diagrams of two-body and three-body abrasive wear. The wear rate depends on the ratio between the hardness of the

abrasive material and the hardness of the abraded surface. A ratio less than 1.2 results in soft abrasion, while hard abrasion is experienced when the ratio is more than 1.2 [61].

The wear mechanism in abrasion is usually a combination of plastic flow and brittle fracture, and depends on the fracture toughness of the abraded surface [7]. It is a generally accepted fact that the abrasive wear resistance of hardmetals is highly dependent on the hardness, Co content and carbide grain size of the hardmetal. The lower the Co content, and the smaller the carbide grain size, the higher the hardness of the alloy and the higher the abrasive wear resistance [51, 63, 64].

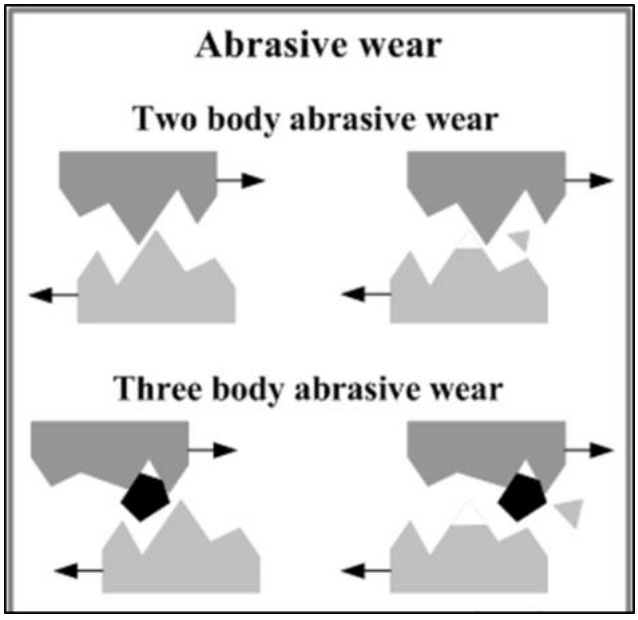



**Figure 2.3** Schematic diagram of two-body and three-body abrasive wear [62].

A short mean free path in the abraded surface results in high wear resistance [65, 66]. The presence of TaC and NbC in the cemented carbide increases the abrasion wear resistance [67], as well as the high temperature resistance to deformation.

The brittle eta phase as well as free carbon precipitation weaken the cemented carbides, and are detrimental to the abrasive wear properties of the alloys.

# 3 Experimental Procedure

## 3.1 Introduction

This chapter describes the experimental procedures that were followed to produce the zinc recycled powders, the sintered alloys and the tests carried out to evaluate the physical, mechanical, microstructural and wear properties of the alloys.

## 3.2 Zinc recycling

Tool grade cemented carbide cutting inserts which were scrapped due to incorrect dimensional tolerances during commercial production at Pilot Tools Pty Ltd (South Africa) were used in this research project. Two separate batches of inserts, weighing two kilograms each were placed into graphite crucibles, as shown in Figure 3.1.



**Figure 3.1:** Tool grade inserts in a graphite crucible.

Zinc with 99.9% purity was added to the crucible in a weight ratio of zinc to binder material of 10:1 [31]. The crucibles were placed into a furnace, which was evacuated and filled with argon. The temperature was raised to 930 $^{o}$C and held for 24 hours to allow for the molten zinc to penetrate the scrap material. The temperature was then raised to 960 $^{o}$C and a vacuum was introduced to distil the zinc out over a period of 36 hours. The conditions were selected based on the original patent by Barnard *et al* [31]. The zinc was collected in the condensation zone of the furnace and cooled for reuse. The furnace was then turned off and the load gradually cooled to room temperature.

## 3.3 Processing of recycled inserts

To assess the effect of the zinc recycling process on the microstructure of the inserts, a sample from the recycled inserts, carefully handled because it was fragile, was mounted in PolyFast resin and lightly ground using a Piatto 1200 grinding disc to flatten the surface. Microstructural analysis was done using a Carl Zeiss Sigma field emission scanning electron microscope (FESEM) at 15 keV in the backscattered mode (BSE). The remainder of the recycled inserts were manually crushed in a steel container using a steel headed hammer. The crushed material was sieved using a 1000 μm sieve to separate the powder, henceforth referred to as recycled powder, and coarse oversize material.

## 3.4 Processing of the oversize material

### 3.4.1 Milling

To further disintegrate them, the oversize particles were introduced into a 1 kg capacity tungsten carbide lined mill along with 18.6 % by weight ethanol, and were milled for 36 hours. A WC-Co milling media to recycled material ratio of

6:1 was used. The particle size reduction was checked periodically during milling. At the end of the milling cycle, the oversize material did not show a significant reduction in particle size. The ethanol was decanted from the material, which was then dried and subjected to characterization tests.

### 3.4.2 Vickers hardness

Some of the oversize samples were mounted in thermosetting resin and polished to 1 μm surface finish following the standard polishing procedure described in section 3.8.6. The polished oversize samples were subjected to a Vickers hardness test using an automatic Mitutoyo Vickers hardness machine. An indenting load of 30 kg and a 10 second dwell time was used according to ISO 3878 [68]. Five indentations were done to determine the average hardness of the sample.

### 3.4.3 Scanning electron microscope (SEM) analysis

The microstructure of the oversize material was analysed using the FESEM at 15 keV in the BSE mode. Energy dispersive x-ray spectroscopy (EDS) and elemental mapping were done at 20 keV.

### 3.4.4 Micro-proton induced x-ray emission (PIXE) analysis

Two-dimensional surface elemental distribution analyses of the major elements, impurities and trace elements was carried out using proton induced X-Ray emission (PIXE) technique, in which a proton beam with a lateral resolution size of 3 μm was employed, hence the name micro-PIXE. A 3 MeV focused proton

beam of approximately 3.5 μm x 3.5 μm lateral resolution was raster scanned over selected micro-areas on the sample surface using an electrostatic scanning coil. The beam current was kept at approximately 100 - 200 pA. Scanned areas were typically analysed in a square pattern of up to a maximum of 128 x 128 pixels, with a dwell time of 10 ms/pixel. The PIXE and proton backscattering spectra were acquired simultaneously as event-by-event data files, using a Si (Li) X-ray detector positioned at a take-off angle of 135 $^{o}$C and shielded with a 125 μm beryllium (Be) filter. The PIXE count rate was kept below 1000 counts/second to avoid pulse pile-up and to achieve satisfactory counting statistics. The accumulated PIXE spectra were reconstructed and analysed off-line using the Geo-PIXE II V 6.4 software package, and the Dynamic Analysis Method [69].

### 3.4.5 Zinc recycling of oversize materials

The oversize materials were subjected to a second recycling run under the same conditions described in section 3.2, for further disintegration. After the second recycling run, the oversize particles were agglomerated into a mass which was difficult to disintegrate. Therefore, no further processing could be done. The resultant recycled material was subjected to the characterization tests described in sections 3.4.3 and 3.4.4.

## 3.5 Processing of the recycled powder

### 3.5.1 Inductively coupled plasma optical emission spectrometry (ICP-OES) analysis

In preparation for the inductively coupled plasma-optical emission spectrometry (ICP-OES) elemental analysis, milling was carried out to homogenize the recycled powder. A 100-g capacity stainless steel ball mill was used, and the

powder was milled along with 18.6 % by weight ethanol. A powder to milling media ratio of 1:3 was used for a milling duration of 2 hours, after which the powder was dried in an MRC vacuum oven at 80 $^{o}$C. The recycled powder was digested in 5 % aqua regia in 30% hydrogen peroxide. The chemical composition of the recycled powder was then analysed using a Thermo Electron ICAP 6300 radial inductively coupled plasma spectrometer utilizing iTeva (Thermo electron) software.

### 3.5.2 Powder stoichiometric adjustments

The ICP-OES analyses of the recycled powder indicated low carbon (C) and cobalt (Co) contents. The recycled powder was separated into two batches of 500 g each. One batch was subjected to a stoichiometric C adjustment, where 0.73 wt % of graphite powder was added. The second batch was subjected to both stoichiometric C and Co adjustment, where 0.73 wt % graphite powder was added, and 1.4 wt % Co powder was added to attain the required amount of 6.6 wt % Co for the commercial grade. Henceforth, the powder which had stoichiometric adjustment of C only will be referred to as R, and the powder which had the stoichiometric C and Co adjustment will be referred to as RA.

The two powder batches were then milled separately in 1 kg capacity ball mills with a 1:6 ball-to-powder ratio until a particle size of approximately 1.7-1.8 μm was achieved. During milling (total duration of 17 hours) particle size analysis was done periodically using a Microtrac S3500 laser diffraction particle size analyser. For these measurements, the powder samples were dispersed in distilled water which had sodium hexametaphosphate as a dispersant. Milling curves were generated for each of the powders. After milling, the powders were dried using an MRC vacuum oven at 80 $^{o}$C until all the ethanol had evaporated. The dried powders were sieved using a 425 μm sieve to break down the powder cakes which

had formed during drying. This resulted in fine powders which had almost evenly sized agglomerates.

## 3.6 Benchmark powders

A third powder batch, henceforth referred to as N, comprising of a blend of new, virgin powders of WC, TiC, TiCN, TaC, NbC and Co, was also milled and dried under the same conditions described in section 3.5.2. Powder N was included in the research study to provide a benchmark comparison for the two recycled powder batches. A fourth powder batch, henceforth referred to as NS, was obtained from commercially blended powder which is used to produce the cutting inserts at Pilot Tools Pty Ltd. The cutting tools which were subjected to the zinc recycling process were produced from powder NS, hence powder NS was also included for benchmarking purposes.

## 3.7 Powder characterization

### 3.7.1 Chemical analysis

The chemical composition of the four powders was analysed using the inductively coupled plasma optical emission (ICP-OES) method. To facilitate the analysis, 20 g samples were taken from each of the four powders, and the polymeric binders were burnt out at 450 $^{o}$C for 2 hrs in a GCA vacuum furnace at 867 mbar. The powders were separately digested in 5 % aqua regia in 30% hydrogen peroxide. The chemical composition was then analysed using a Thermo Electron ICAP 6300 radial inductively coupled plasma spectrometer utilizing iTeva (Thermo electron) software.

### 3.7.2 Powder morphology and phase analyses

The powder morphology was studied using the Carl Zeiss FESEM at 15 keV in the BSE mode. The EDS was used for elemental composition analysis at 20 keV. Phase identification was done using a BRUKER D2 X-ray diffraction machine with Co-Kα radiation and PANalytical X'Pert High Score software. The x-ray diffraction data was collected for 2θ values between $10^o$ and $90^o$ with a $0.02^o$ step size at 40 kV and 40 mA.

## 3.8 Powder compaction and sintering

Two different types of samples were pressed from each of the four powders in preparation for sintering and subsequent testing. For the general materials characterization, green compacts were pressed using a Dorst press which has a 15 mm x 15 mm die. Approximately 8 g of milled powders was weighed using a digital scale and poured into the die and then pressed using a pressure of 5 tons. For the wear tests, 25 mm diameter cylindrical green compacts were pressed from 25 g of milled powder using an AB Alpha press at a pressure of 12 tons. All the samples were weighed using a Scalerite analytical balance, and the height of each sample was measured using a vernier callipers to facilitate the determination of dimensional changes after sintering. The green density of the square samples was determined according to the formula in equation 3.1, as detailed in ASTM B610-08 [70].

$$D_G = \frac{M}{WTL} \qquad \text{(Equation 3.1)}$$

where,

$D_G$ = green density of test specimen, $gcm^{-3}$

M = mass of green test specimen, g

W = width of green test specimen, cm

T = thickness of green test specimen, cm, and

L = length of green test specimen, cm.

The elemental distribution of major, impurity and trace elements in the green compacts was determined using micro-PIXE analysis, as described in section 3.4.4. To facilitate the analysis, the green compacts were first gently ground flat using a Piatto 1200 grinding disc. Sintering of the green compacts was done in an ULTRA-TEMP Sinter-HIP furnace at a temperature of 1510 $^{o}$C, followed by hot isostatic pressing (HIP).

## 3.9 Characterization of sintered alloys

### 3.9.1 Percentage shrinkage

The height of the samples was measured using a vernier callipers in order to determine the absolute dimensional change of the respective alloys according to equation 3.2, as detailed in the ASTM B610-08 standard [70].

$$\% \text{ Shrinkage} = \frac{L_T - L_D}{L_D} \times 100 \qquad \text{(Equation 3.2)}$$

where,

$L_T$ = height of green compact, mm

$L_D$ = height of sintered sample, mm.

### 3.9.2 Density and Porosity

The true density of the sintered samples was measured using a Shimadzu Scalerite AY120 scale, equipped with an automatic density suspension and reporting system, which operates on Archimedes' Principle according to ASTM 311-08 [71]. Open porosity was determined according to ASTM 373-88 [72]. To facilitate the accurate determination of the open porosity, three weights were determined for each sample, namely; dry mass ($W_1$), wet mass ($W_2$) and suspended mass ($W_3$), and were obtained as follows: Three samples from each batch of sintered samples were boiled in distilled water for 5 hours to eliminate bubbles from the sample surfaces. After boiling, the samples were weighed in air to obtain the wet mass ($W_2$), and then suspended in distilled water to obtain the suspended mass ($W_3$). After weighing, the samples were dried in a EcoTherm Labotec Furnace at 80 $^oC$ for 24 hours to eliminate all the moisture. Thereafter the samples were then weighed in air to obtain the dry mass ($W_1$). Volume percentage open porosity was determined from equation 3.3 [72].

$$\text{Volume percentage open porosity} = \frac{W2 - W1}{W2 - W3} \times 100 \quad \text{(Equation 3.3)}$$

### 3.9.3 Magnetic properties

#### 3.9.3.1 Magnetic Saturation (CoM)

The magnetic saturation of the sintered samples was measured using a Setaram Sigma-meter equipped with a Scout Pro SPU402 digital balance. The technique determines the amount of magnetic binder material (CoM), and measures the material's magnetic force when placed in a homogeneous magnetic field. The theoretical CoM was determined using equation 3.4 [58]. A comparison was made between the measured and theoretical values. If the measured value was less than the theoretical value, it indicates that W had dissolved in the Co solid solution [58].

$$\text{Theoretical CoM } (\mu Tm^3/kg) = 2.02 \times \text{wt \% Co} \quad \text{(Equation 3.4).}$$

#### 3.9.3.2 Coercivity ($H_c$)

Coercivity of the sintered samples was determined using a Dr. Forster-Koerzimat 1.095 Coercimeter according to standard ISO 3326 [73]. The coercimeter has a magnetic field generating unit, and a magnetic field measuring unit. Each sample was attached to a wooden holder and placed into the magnetic field generating unit. A strong magnetic field was applied to fully magnetize the sample, and then the magnetic field polarity was reversed to demagnetize the samples. This demagnetizing field was measured by the magnetic field measuring unit to give the coercive force ($H_c$).

### 3.9.4 Sample preparation

A Secotom-10 cutting machine with a 12 cm diamond coated cutting wheel was used to section the square samples to the desired sizes for the respective characterization tests. A wheel speed of 2000 rpm and a feed rate of 0.02 mm/s were used. The sectioned samples were mounted in Bakelite using a Leco Mounting Press at 250 bars and 180 $^{o}$C. Water was used as a coolant during the mounting cycle. A Struers LaboPol-5 machine was used for grinding and polishing; procedure as outlined in Table 3.1. The polished samples were etched for two minutes using Murakami's reagent, which was made from 10 g potassium hydroxide and 10 g potassium ferrocyanide dissolved in 100 ml distilled water. After etching, the samples were rinsed using running water, followed by ethanol, and then dried.

**Table 3.1** Grinding and polishing procedure.

| **Process** | **Step** | **Disc/cloth** | **Coolant/ lubricant** | **Speed (rpm)** | **Load/ (N)** | **Time (min)** |
|---|---|---|---|---|---|---|
| Grinding | 1 | 220 | Water | 350 | 35 | 10 |
| | 2 | 1200 | Water | 350 | 35 | 10 |
| Polishing | 1 | Plaran-9 μm | Diamaxx 9 μm diamond suspension and lubricant | 300 | 30 | 10 |
| | 2 | Daran 3μm | Diamaxx 3 μm diamond suspension and lubricant | 250 | 20 | 5 |
| | 3 | Napal 1μm | Diamaxx 1 μm diamond suspension and lubricant | 250 | 20 | 5 |

### 3.9.5 Microstructural analysis

#### 3.9.5.1 Optical microscopy

The etched samples were analysed using an Olympus SZ-X16 stereo optical microscope, equipped with a SC30 digital camera and AnaySIS 5.2 software at a magnification of 200x. This was done to establish if there was a functional gradient in the samples.

#### 3.9.5.2 Carbide grain size ($d_c$)

Micrographs were taken with the FESEM at 5000x magnification and were used to determine the average WC grain size according to Heyne's linear intercept method [7]. To determine the average grain size, 30 lines, 100 mm long, were randomly drawn on the micrographs. The number of carbide grains traversed by each line was counted and recorded, and the Heyn grain size ($d_c$), was determined from equation 3.5 [7].

$$d_c = \frac{L}{N} \qquad \text{(Equation 3.5)}$$

where,

L = the actual length of the line, and

N = the number of carbide grains traversed.

### 3.9.5.3 Carbide contiguity (C)

On the same set of lines drawn for grain size determination, carbide contiguity was determined from equation 3.6 [7].

$$C = \frac{2(N)\alpha\alpha}{2(N)\alpha\alpha + (N)\alpha\beta} \quad \text{(Equation 3.6)}$$

where,

C = contiguity

$(N)_{\alpha\alpha}$ = average number of intercepts per unit length with traces of carbide-carbide grain boundaries, and

$(N)_{\alpha\beta}$ = average number of intercepts per unit length with traces of carbide-binder interfaces.

### 3.9.5.4 Binder mean free path ($\lambda_{Co}$) and volume fraction ($V_{Co}$)

The binder mean free path was determined from equation 3.7 [51].

$$\lambda_{Co} = \frac{d_{WC}V_{Co}}{(1+C)V_{WC}} \quad \text{(Equation 3.7)}$$

where,

$\lambda_{Co}$ = binder mean free path, μm

$d_c$ = average carbide grain size, μm

$V_{Co}$ = volume fraction of the binder

$V_{WC}$ = carbide volume fraction = $(1 - V_{Co})$, and

C = carbide contiguity.

The binder volume fraction ($V_{Co}$) was determined from equation 3.8 [74].

$$V_{Co} = \frac{\frac{wt\ \%\ Co}{Density\ of\ Co}}{\frac{mass\ of\ sample}{Density\ of\ sample}} \qquad \text{(Equation 3.8)}$$

### 3.9.6 Elemental and phase analysis

The elemental distribution of the major elements, impurities and trace elements in the alloys was determined using micro-PIXE analysis, as detailed in 3.4.4. The phase present in the alloys were identified using XRD analysis, as described in section 3.7.2. The EDS technique was also used to provide complimentary elemental composition analyses.

### 3.9.7 Mechanical properties

#### 3.9.7.1 Vickers Hardness

Prior to testing, the residual stresses generated in the samples due to sample preparation were eliminated by subjecting the alloys to a stress relieving heat treatment at 800 $^{o}$C for 4 hrs [75]. Vickers macro-hardness was then determined using a Mitutoyo AVK-Co hardness tester with a 30 kg load applied for 10 seconds according to ISO 3878 [68]. Five indentations were made on each sample

to obtain the average macro-hardness. The indentations were adequately spaced to avoid the overlapping of the radial cracks. The Vickers hardness was calculated from equation 3.9 [76].

$$HV_{30} = \frac{1.854\ x\ 30kgf}{D^2} \qquad \text{(Equation 3.9)}$$

where,

D = average diameter of the diagonals, mm.

### 3.9.7.2 Rockwell hardness

To further confirm the hardness of the sintered samples, the Rockwell A hardness test was conducted using a Mitutoyo AKR-600 Rockwell-A machine, with a 60 kg load applied for 10 seconds according to ASTM E18-03E1 [77]. Five measurements were taken on each sample to determine the average hardness.

### 3.9.7.3 Fracture toughness

A Mitutoyo AVK-Co hardness tester with a 30 kg load applied for 10 seconds was used to make the diamond indentations which had radial cracks emanating from the corners of the diamond indentation. The FESEM was used to measure the lengths of the diagonals and the Palmqvist cracks emanating from the corners of the diamond indentation at 500x magnification, as illustrated in Figure 3.2.

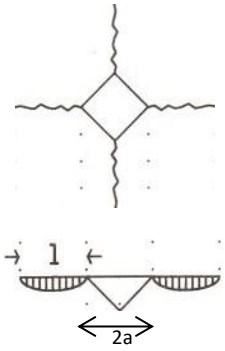



**Figure 3.2** Crack geometry of Palmqvist cracks [75].

Since the condition that $0.25 \leq \frac{l}{a} \leq 1.25$ was satisfied for all the samples, the fracture toughness was determined from the Warren and Matzke relationship [78], given in equation 3.10.

$$K_{Ic} = 0.0887 \left(\frac{HF}{4l}\right)^{1/2} \quad \text{(Equation 3.10)}$$

where,

$K_{Ic}$ = fracture toughness, $MPa.m^{1/2}$

H = hardness in GPa = $HV_{30}$ x 0.009807

F = applied force, N

l = average crack length, mm.

### 3.9.8. Slurry abrasion tests

Slurry abrasion testing was used in this research as a basis of comparison of the wear behaviour of the un-recycled and zinc recycled alloys. The tests were carried out using a modified ASTM G105 [79] slurry abrasion machine. Silica sand

which had angular morphology, an average hardness of 1084 ± 156 HV [80] and an average particle size of 606 µm was used as the abrasive medium.

The test set up is shown in Figure 3.3 and the test parameters are given in Table 3.2. Three samples from each of the four alloy grades were tested simultaneously to determine the average mass loss. The abrasive media comprised of a slurry, which was made from of 250 g silica sand and 2500 g distilled water. The slurry was circulated by a pneumatic pump at a pressure of 480 kPa. Prior to testing, the pump was run for at least two minutes in order to establish a steady flow of the slurry. During testing the samples were pressed onto a rotating rubbed lined cylinder by exerting a 6 kg load on the loading arm, denoted as C in Figure 3.3(a). To determine the mass loss, the test was stopped at 30 minute intervals, and the samples removed, thoroughly cleaned in an ultrasonic bath and then dried. Mass loss was measured using an analytical mass balance with a sensitivity of 0.1 mg. Worn surfaces in both planar and cross-sectional orientation were analysed using the FESEM at 15 keV in the BSE mode in order to determine the wear mechanism.

**Table 3.2** Slurry abrasion test parameters.

| **Test parameter** | |
|---|---|
| Slurry composition | 10 wt% $SiO_2$ particles in distilled water |
| Test load | 60N |
| Testing time | 4 hours |
| Mass loss measurements | 30 min intervals |
| Wheel speed | 100 rpm |

(a)




(b)

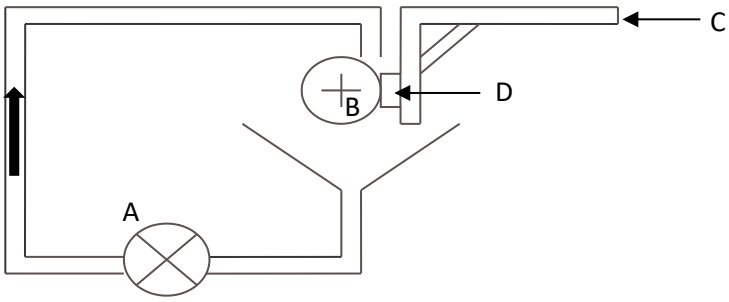



**Figure 3.3** (a) Slurry abrasion test rig and (b) schematic diagram of the slurry abrasion test rig [72]. In both (a) and (b), A is the pump, B is the rubber lined cylinder, C is the loading arm and D (not shown in (a)) is the test specimen.

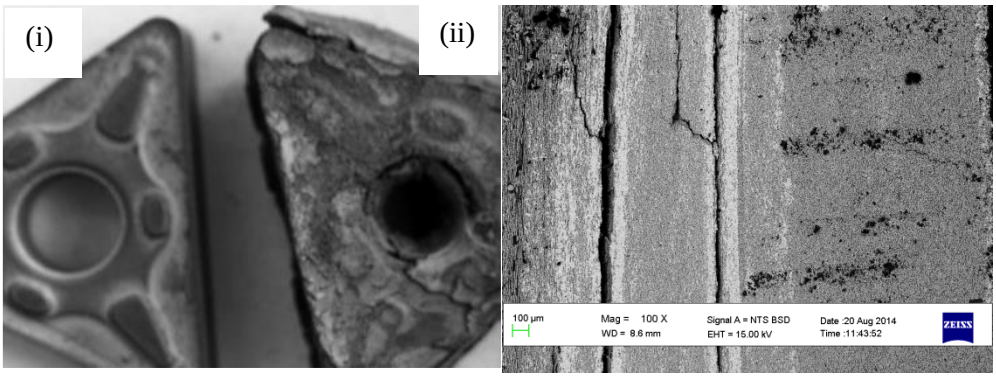
# 4. Results

## 4.1 Introduction

This chapter summarises the results from all the tests carried out. It presents the products from the zinc recycling process, powder milling data, as well as powder morphology and phase analyses. Results on microstructural analysis, physical and mechanical properties of the sintered alloys are also summarised.

## 4.2 Zinc Recycling

The recycled materials maintained their general insert shape, but showed a marked increase in volume, and a layered surface appearance. A comparison of the un-recycled and recycled insert is shown in Figure 4.1 (a), and the layers of a recycled insert are shown in Figure 4.1 (b).




(a) (b)

**Figure 4.1** (a) Optical image of tool grade insert (i) before zinc recycling, and (ii) after zinc recycling, showing an increase in volume and peeling of the surface layer. (b) FESEM micrograph of the zinc recycled material showing different layers from the surface (left) into the inner (right) section.

Figure 4.2 shows a comparison of the microstructure of the tool grade insert before and after zinc recycling. Table 4.1 lists the EDS analysis results, which shows that the un-recycled insert had more W (80 wt %), compared to the recycled (64.70 wt %). EDS also confirmed the grey phase as WC which had light grey mixed crystal carbides concentrated round the edges and the dark phase as the Co binder. The binder phase was quite distinct in the un-recycled insert, but was not visible in the recycled insert, indicating effective binder disintegration due to zinc recycling.

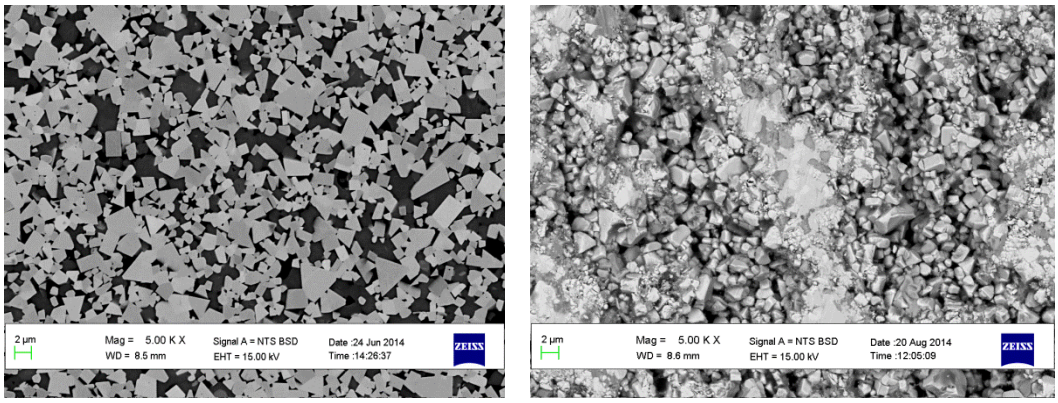



**Figure 4.2** FESEM micrographs of the (a) un-recycled insert, in which the grey WC, light grey mixed crystals, and the dark Co phases are distinct, and (b) the recycled material in which only the grey WC phase is distinct (the light grey areas are as a result of smeared powder particles during light grinding).

**Table 4.1** EDS analysis results for recycled and un-recycled insert.

| **Element** | **Recycled material/ wt %** | **Un-recycled insert/ wt %** |
|---|---|---|
| W | 64.70 | 80.33 |
| Co | 6.57 | 7.03 |
| Ti | 4.51 | 5.09 |
| O | 7.07 | - |

Crushing the zinc recycled inserts yielded about 70% fine powder with average particle size of 8 ± 3 μm and 30 % coarse oversize particles which were about 3 mm in diameter. The characterization of the recycled powders and the oversize particle is presented in the following two sections.

## 4.3 Recycled Oversize Particles Characterisation

A closer inspection of the oversize particles indicated that the particles were a product of the outer surface of the original inserts, as shown in Figure 4.3. The Vickers hardness test on the oversize particles yielded an average hardness of 653.3 ± 66.4 $HV_{30}$. Appendix A provides the recorded $HV_{30}$ values.

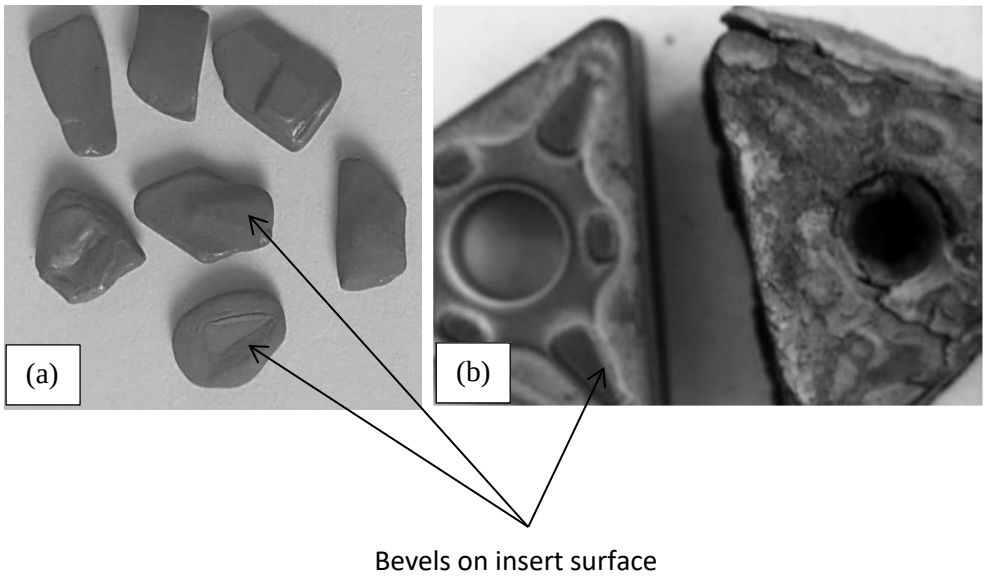



**Figure 4.3** Optical images of (a) oversize particles and (b) the tool grade inserts before recycling (left) and after recycling (right). The oversize particles were predominantly from the surface layer of the inserts, as shown by bevels and grooves on the oversize particles.

Figure 4.4 shows the microstructure of the recycled oversize particles. The EDS PIXE analysis results for the recycled oversize particle are shown in Table 4.2, and confirm that the carbide particles were agglomerated together by a thin Co film which is not readily visible in the micrograph. Figure 4.5 shows the EDS elemental distribution maps of the major elements in the oversize particles. All elements except Ti were almost uniformly distributed in the oversize particles.

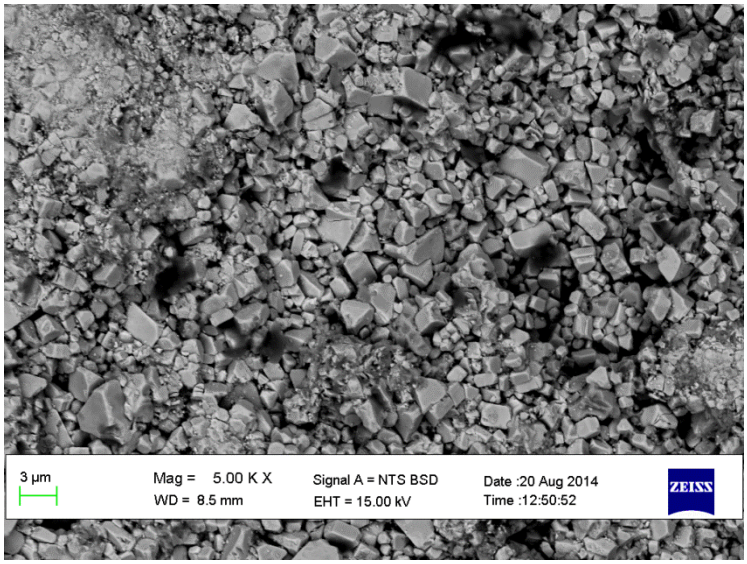



**Figure 4.4** FESEM micrograph of oversize particle, showing agglomerated carbide particles.

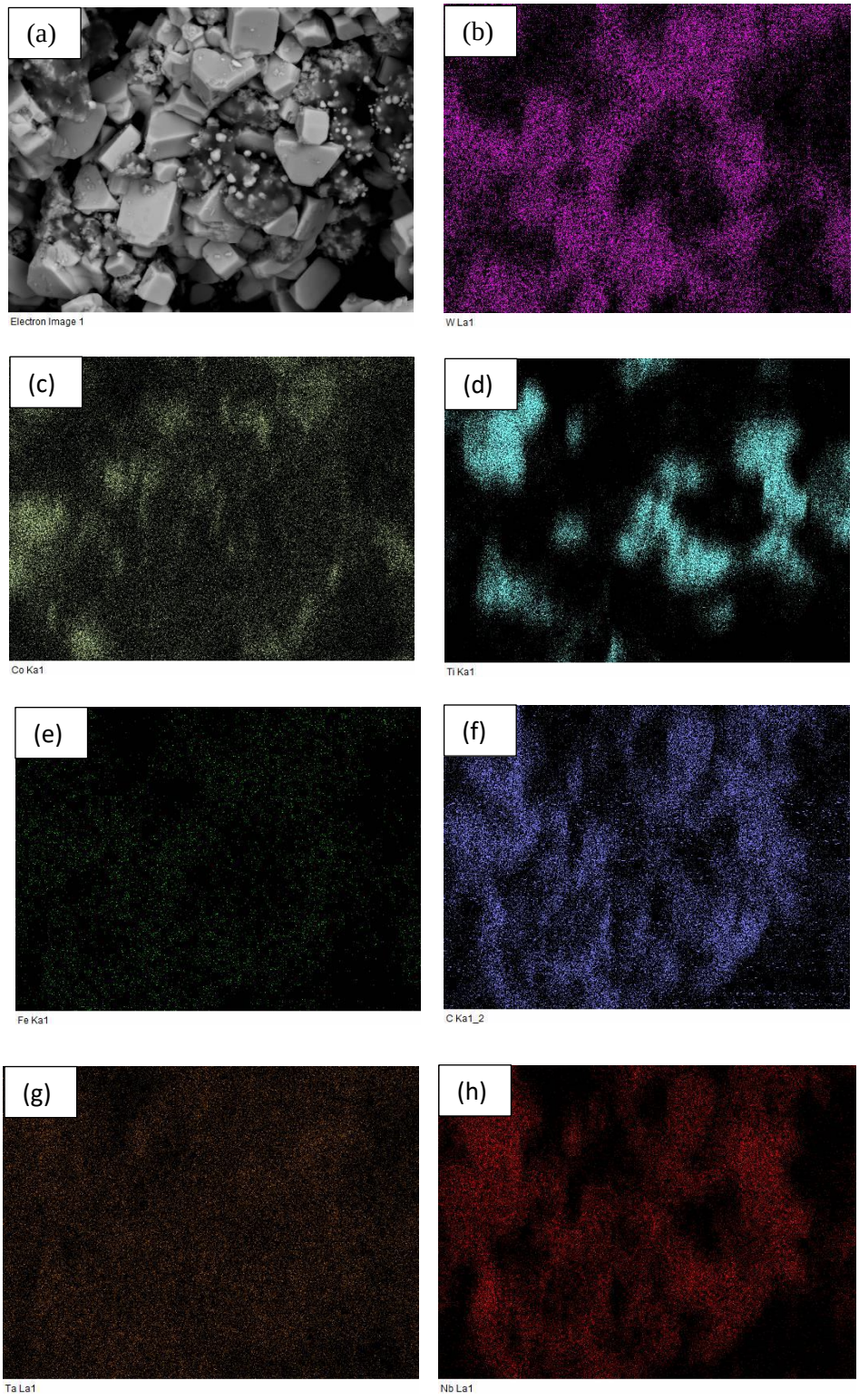



**Figure 4.5** (a) FESEM micrograph of oversize particle, and FESEM elemental distribution maps of (b) $W_L$, (c) Co, (d) Ti, (e) Fe, (f) C, (g) $Ta_L$ and (h) Nb. All elements except Ti are generally evenly distributed.

Table 4.2 shows the results of EDS and micro-PIXE analysis of the oversize particles. EDS analysis indicated 13.17 wt % Co, and micro-PIXE analysis indicated 9.77 wt % Co, and these values were higher compared to the expected stoichiometric Co content of 6.6 wt% in the scrap material before recycling. This indicated possible concentration of Co in the oversize particles as zinc was distilled out of the scrap material during zinc recycling. In addition to the major elements, micro-PIXE analysis detected Fe, S, Ca, K and Cl as the major impurities, and Ni, Cr and Mn as the trace impurities in the oversize particles. The Fe content was higher in the oversize particles compared to the recycled powder, whose composition from ICP-OES is shown in Table 4.4. Impurities such as Ca Cl and K were most likely introduced as residues from ore processing, while S was introduced together with carbon black during powder processing [7]. Powder NS, used to produce cutting tools which were later zinc recycled, is milled in stainless steel mills at Pilot Tools Pty Ltd. Therefore, there is a possibility that Ni, Cr and Mn were introduced into the powder NS during milling, and reported to the oversize particles after zinc recycling.

**Table 4.2** EDS and micro-PIXE analysis results for oversize particles.

| Element | EDS /wt % | Micro-PIXE / wt % |
|---|---|---|
| W | 68.53 | 66.72 |
| Ti | 5.99 | 5.33 |
| Ta | 2.54 | 2.32 |
| Nb | 0.51 | 0.189 |
| Co | 13.17 | 9.77 |
| C | 5.46 | - |
| O | 3.63 | - |
| Fe | 0.16 | 0.20 |
| S | - | 0.889 |
| Ca | - | 0.32 |
| K | - | 0.16 |
| Cl | - | 0.40 |
| Ni | - | 329 ppm |
| Cr | - | 128 ppm |
| Mn | | 37 ppm |

Figure 4.6 shows the micro-PIXE distribution maps of the major elements in the oversize particles. Co was segregated towards the centre of the oversize particle, while slight segregation of W towards the edge was also evident. Ti, Ta and Nb were evenly distributed throughout the oversize particle.

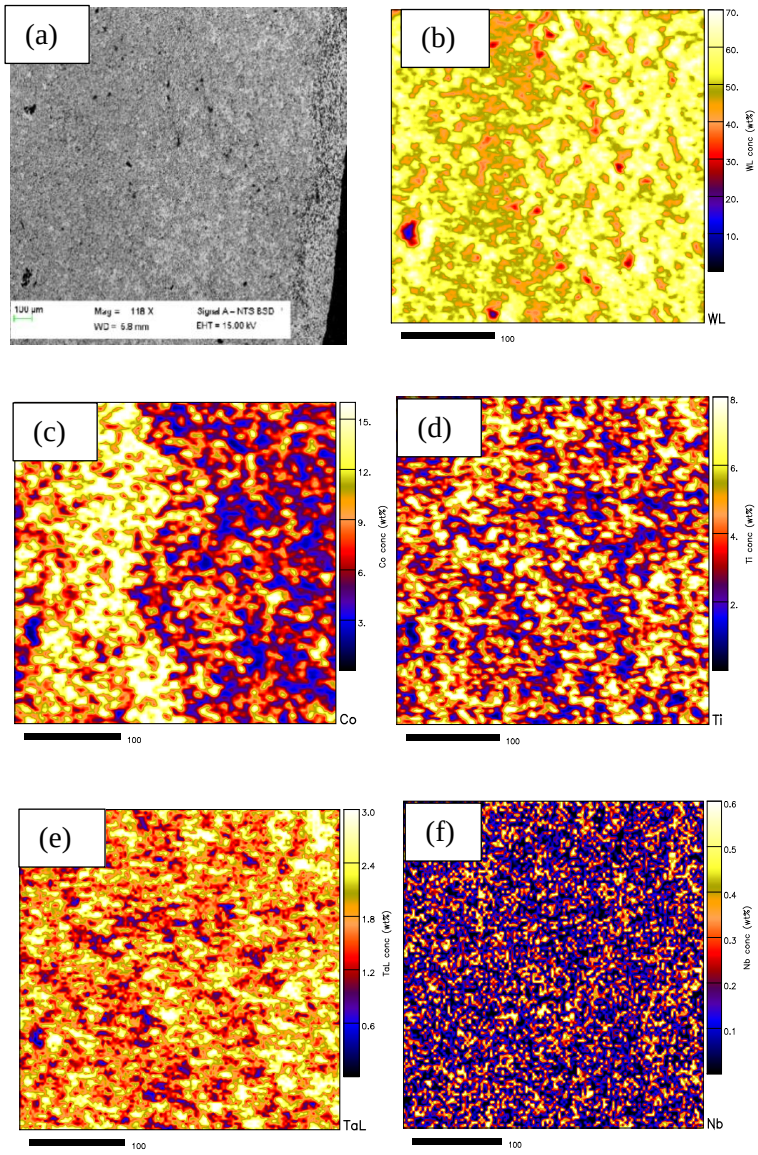



**Figure 4.6** (a) FESEM micrograph of oversize particle. Micro-PIXE elemental distribution maps of (b) $W_L$, (c) Co, (d) Ti, (e) $Ta_L$ and (f) Nb. Yellow areas indicate regions of high concentration, and blue to dark areas show regions of low concentration of a given element.

Figure A1 in Appendix A shows the micro-PIXE distribution maps of the major and impurity elements in an area zoomed into the centre of the oversize particle. The Fe, Ca, S and K impurities were segregated towards the centre of the particle. The Co pools that had a maximum of 20 wt% were also observed; further indicating Co concentration in the oversize particles during the recycling process. Ti pools were also observed.

Subjecting the oversize particles to a second recycling session resulted in the agglomeration of the particles to form a hard cemented tungsten carbide mass. Figure 4.7 shows that the material had a shiny surface and a dark grey core after the second recycling session, and Figure 4.8 shows the SEM micrograph of a piece of material that was taken from the chipped area in Figure 4.7. The light grey phase is the carbide, while the dark grey phase is the cobalt binder, and the black regions are pores within the material. Despite the material having a lot of pores, the carbide particles were still strongly held together by the binder material, which made it difficult to disintegrate the material.



**Figure 4.7** Material from the second zinc recycling session, showing a shiny outer layer and a dark core.

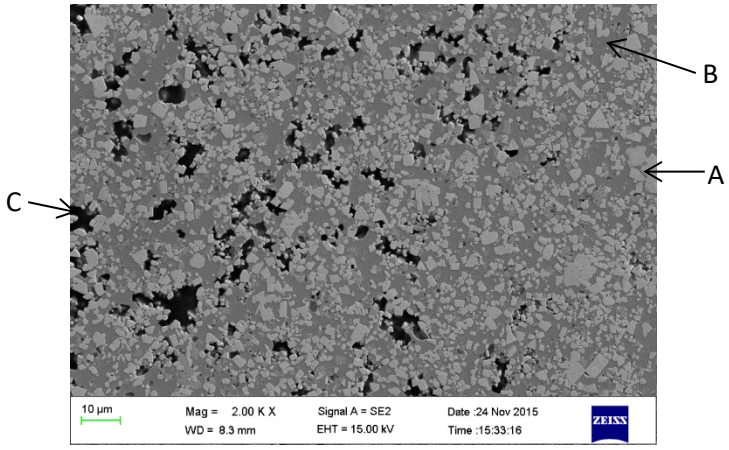



**Figure 4.8** FESEM micrograph of the material subjected to a second recycling session, showing (A) light grey WC phase, (B) dark grey Co binder phase, and the (C) pores.

Table 4.3 shows the EDS analysis results of the material subjected to a second recycling session. EDS indicated a high Co concentration towards the surface of the material, while the W concentration was slightly lower compared to the concentrations in the oversize particles obtained in the first recycling session. (Refer to Table 4.2). The W, Ti, and Nb contents remained within the same ranges as in the oversize particles. The Fe content was slightly higher, while the Ta content was slightly slower in the material subjected to the second recycling session compared to the oversize particles.

**Table 4.3** EDS analysis of the material subjected to a second recycling process.

| Element | Wt % |
|---|---|
| W | 62.38 |
| Co | 23.25 |
| Ti | 4.18 |
| Ta | 0.91 |
| Nb | 0.43 |
| Fe | 1.28 |
| C | 6.03 |
| O | 1.55 |

Figure 4.9 shows the micro-PIXE elemental distribution maps of the major elements W, Co and Ti, and the trace elements Fe and Zn in the material subjected to a second recycling session. The $W_L$ map shows higher concentration towards the edge, while Co and Fe were concentrated away from the surface. The elements Ti and Zn were evenly distributed. Figure 4.10 provides further information on the distribution of elements through FESEM elemental maps. Concentration of Co in the oversize material is quite apparent, thus confirming the high concentration of Co in the oversize material.

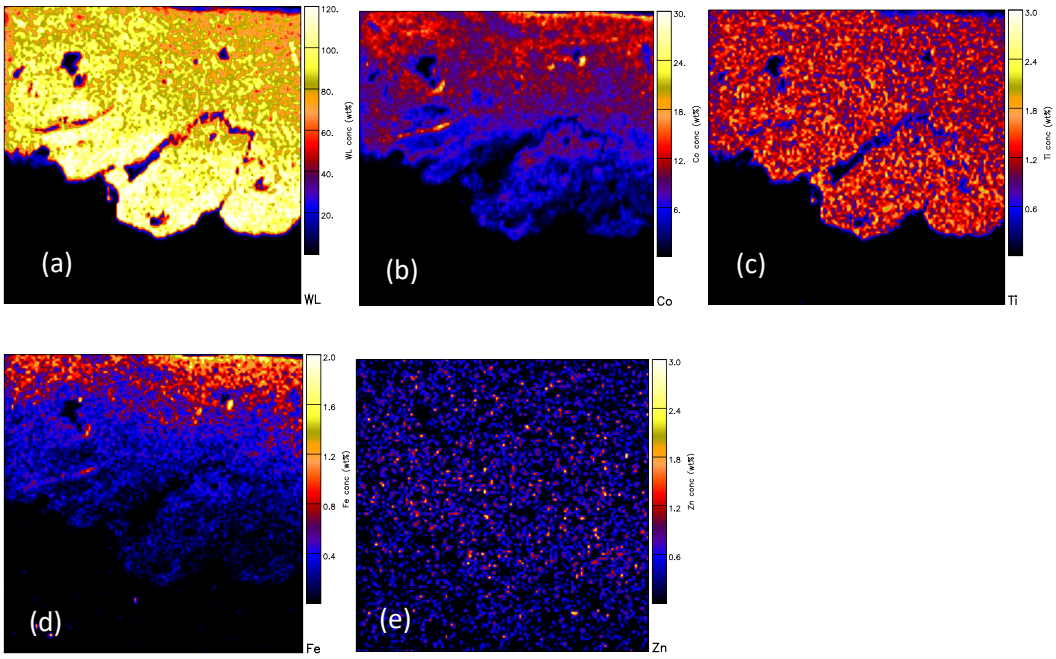



**Figure 4.9** Micro-PIXE elemental distribution maps of (a) $W_L$, (b) Co, (c) Ti, (d) Fe, and (e) Zn. Yellow areas indicate regions of high concentration, and dark areas indicate regions of low concentration.

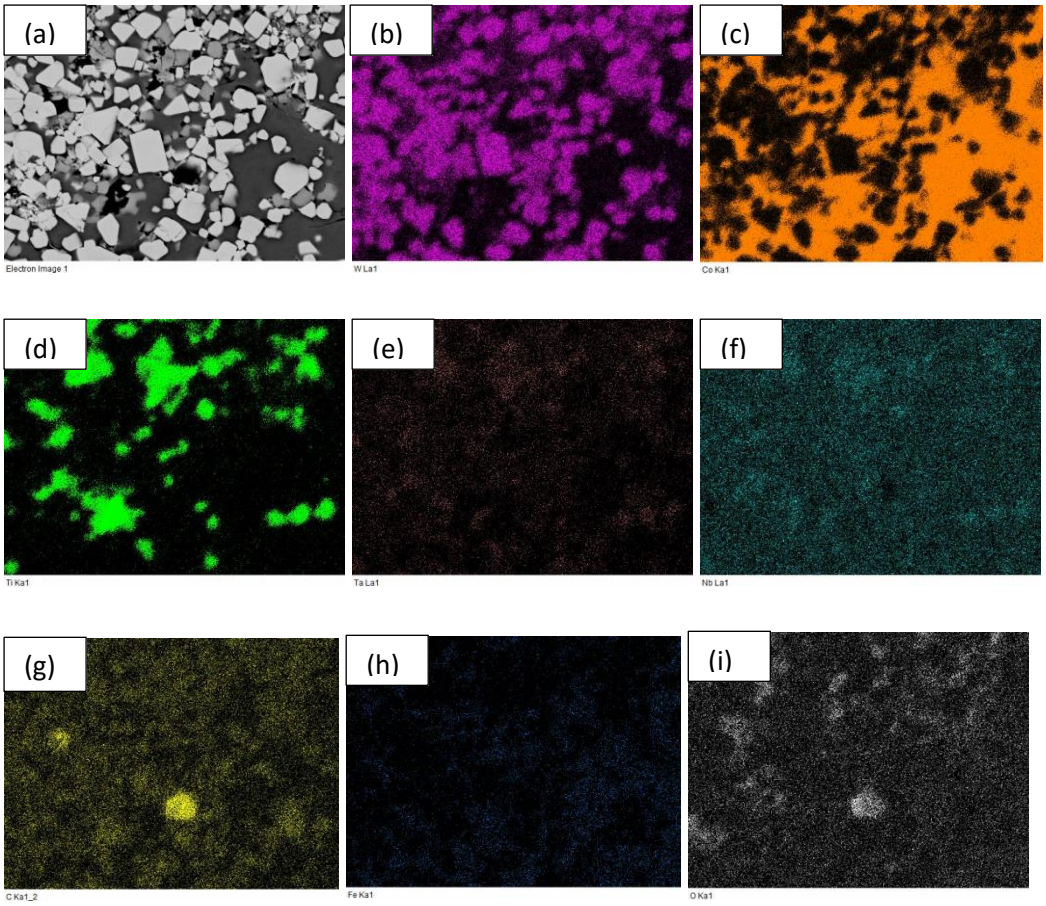



**Figure 4.10** (a) FESEM micrograph of material subjected to second recycling process, and FESEM elemental distribution maps of (b) $W_L$, (c) Co, (d) Ti, (e) $Ta_L$, (Nb, (g) C (h) Fe and (i) O. The material appears as if it was sintered, and concentration of Co in the material is quite apparent.

## 4.4 Recycled Powder Characterization

This section presents the findings on the processing and characterization tests carried out on the recycled and un-recycled powders. The section includes results from FESEM, ICP-OES and micro-PIXE analyses, as well as the milling data for the powders.

Figure 4.11 shows the morphology of the zinc recycled powder as recovered after crushing the zinc recycled inserts. The grains were largely angular in shape, and the powder showed a wide particle size distribution, ranging from 0.5 – 8 µm. Table 4.4 shows the ICP-OES analysis results of the recycled powder. In addition to the major elements, trace elements were also detected. W and Ti were generally within the expected levels (about 80 wt % and 3 wt% respectively). About 2 wt % Ta and 5.84 wt % Co were detected, and were close to the expected values. For Nb, 0.68 wt % was detected in the recycled powder, and was almost double the expected amount. The carbon content was also found to be 5.59 wt %, which was lower than the expected 6.32 wt %, as carbon is lost due to oxidation reactions that take place during sintering [7]. Impurities were also detected in the recycled powder, with Si, Fe, Mn and S being the major impurities. Traces of Zn, Cr, Ni and V were also detected in the powder.

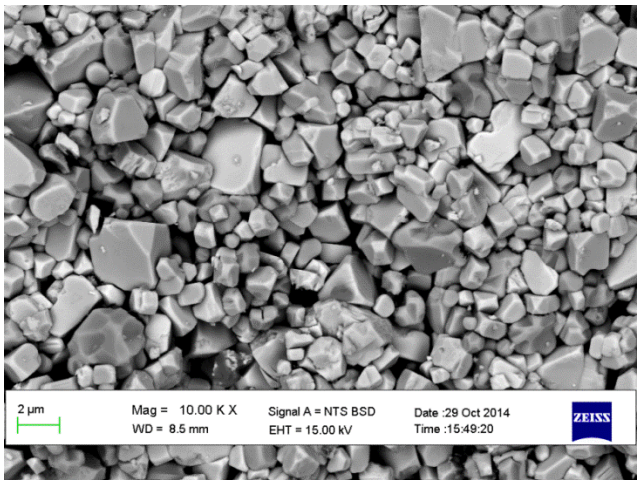



**Figure 4.11** Morphology of the recycled powder showing a wide particle size distribution of angular grains.

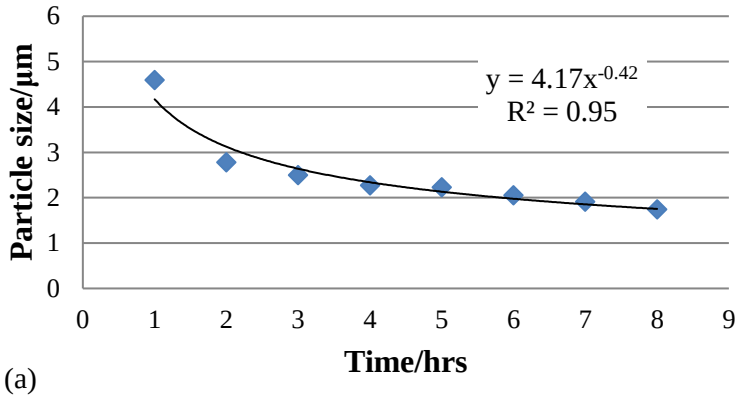
**Table 4.4** ICP-OES analysis of recycled powder.

| Element | Weight % |
|---|---|
| W | 80.5 |
| Ti | 3.35 |
| Ta | 1.99 |
| Nb | 0.68 |
| Co | 5.84 |
| C | 5.59 |
| S | 0.014 |
| Fe | 0.064 |
| Mn | 0.03 |
| Si | 0.27 |
| Mo | ≤ 0.005 |
| Cr | 185 ppm |
| Ni | 330 ppm |
| Zn | 55 ppm |
| V | 92 ppm |

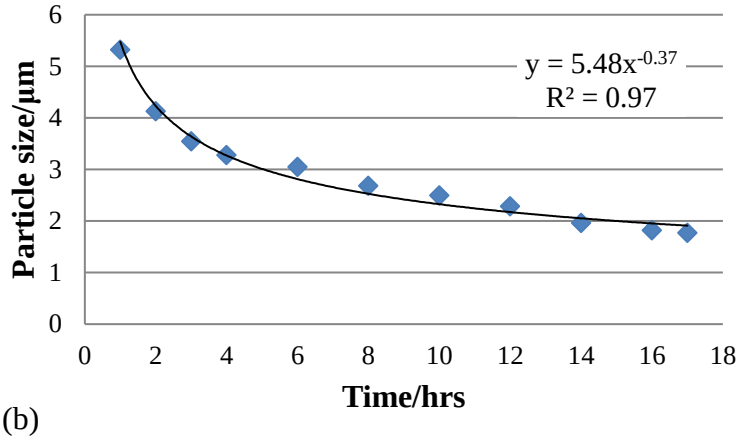
Table 4.5 shows the milling data of un-recycled powder (N), and recycled powders R and RA. The corresponding milling curves are shown in Figure 4.12. The milling curve for the commercial un-recycled powder, NS, is not included as it is a commercial grade, and Pilot Tools Pty Ltd Plant Manager, Dr C.S. Freemantle, confirmed that the milling behaviour of the un-recycled powder N closely matches that of the commercial powder NS. The total milling time for un-recycled powder N and recycled powders R and RA was 8 hours and 17 hours respectively, and the powders were milled down to 1.7-1.8 μm. The milling curves show significant size reduction in the first two and four hours respectively for the un-recycled powder N and the recycled powders R and RA, and then size reduction became more gradual as milling proceeded.

**Table 4.5** Milling data for powders of grade N, R and RA.

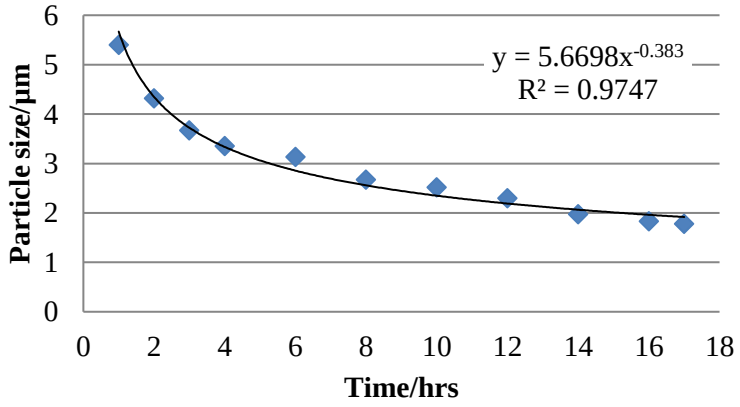
| | **Particle size/ µm** | | |
|---|---|---|---|
| **Time/ hrs** | **Grade N** | **Grade R** | **Grade RA** |
| 1 | 4.590 | 5.320 | 5.400 |
| 2 | 2.780 | 4.130 | 4.320 |
| 3 | 2.498 | 3.550 | 3.670 |
| 4 | 2.270 | 3.280 | 3.351 |
| 5 | 2.230 | - | - |
| 6 | 2.049 | 3.050 | 3.132 |
| 7 | 1.908 | - | - |
| 8 | 1.744 | 2.684 | 2.672 |
| 10 | | 2.496 | 2.520 |
| 12 | | 2.284 | 2.298 |
| 14 | | 1.967 | 1.972 |
| 16 | | 1.824 | 1.830 |
| 17 | | 1.770 | 1.779 |




(a)




(b)




(c)

**Figure 4.12** Milling curves of powders (a) N, (b) R and (c) RA, showing longer milling times for the recycled powders R and RA compared to the un-recycled powder N.

Figures 4.13A and 4.13B show the particle size distribution of the un-recycled and zinc recycled powders respectively, and Table 4.6 summaries the D10, D50 and D90 values. The commercial powder, NS, had the lowest D10 and D50 values, and had the largest span, indicating a wider particle size distribution. The zinc recycled powder, R, had the highest D10 and D90 values, indicating a larger proportion of coarser particles compared to the other powders. Table B1 in Appendix B summaries the particle size distribution of the powders.

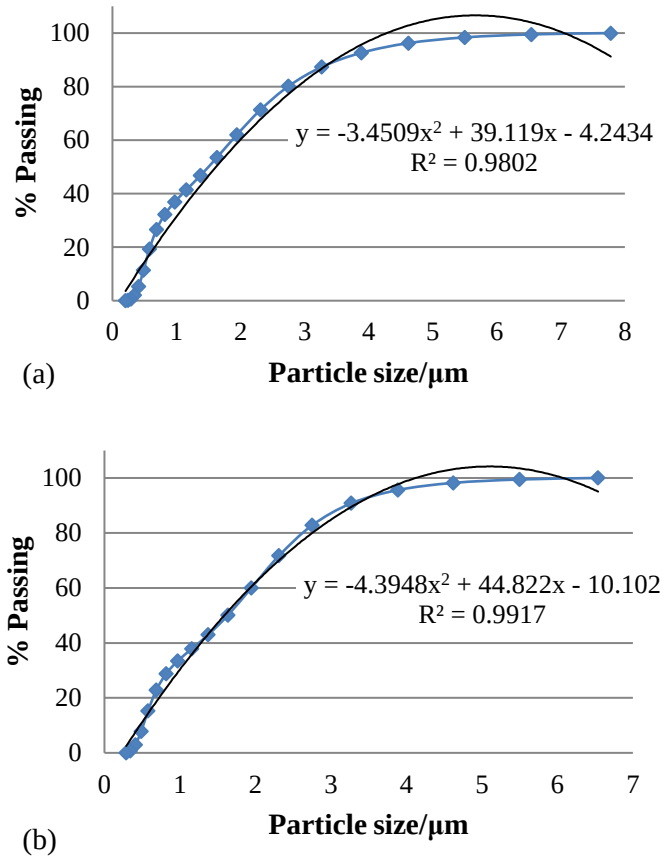



**Figure 4.13A** Particle size distribution of the virgin powders (a) NS and (b) N.

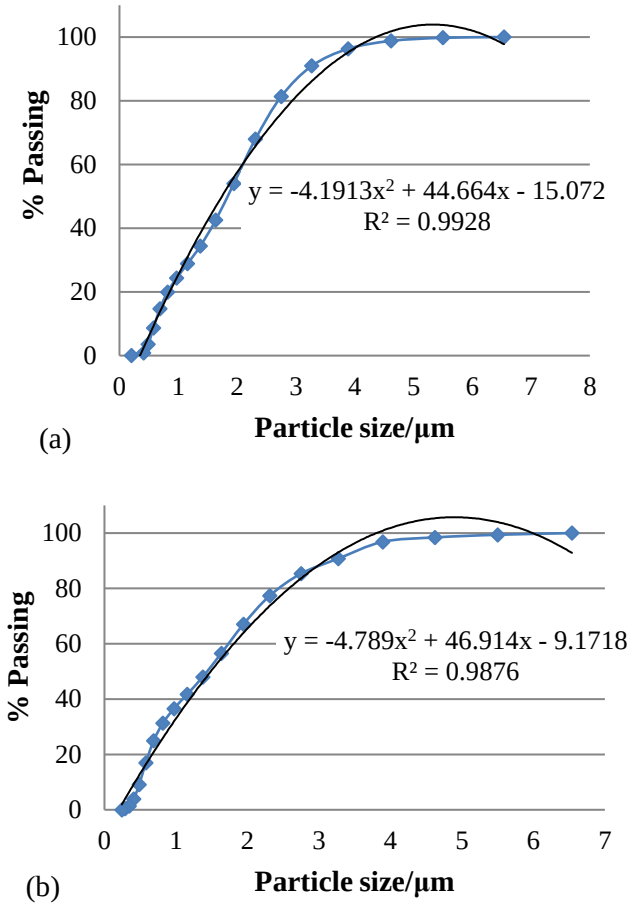



**Figure 4.13B** Particle size distribution the zinc recycled powders (a) R and (b) RA.

**Table 4.6** $D_{10}$, $D_{50}$ and $D_{90}$ values for the milled powders.

| **Parameter/µm** | **NS** | **N** | **R** | **RA** |
|---|---|---|---|---|
| **$D_{10}$** | 0.377 | 0.470 | 0.595 | 0.427 |
| **$D_{50}$** | 1.617 | 1.588 | 1.742 | 1.487 |
| **$D_{90}$** | 3.473 | 3.031 | 3.506 | 3.086 |
| **Mean** | 1.720 | 1.770 | 1.744 | 1.779 |
| **Span ($D_{90} - D_{10}$)** | 3.096 | 2.561 | 2.911 | 2.659 |

Table 4.7 summarises the chemical composition of the milled powders obtained from ICP-OES analysis. The recycled powders R and RA had a slightly higher W content than the virgin powders NS and N. The recycled powders R and RA had the lowest and highest Co contents respectively, while RA had a lower Ti content and higher Nb content compared to the other powders. Impurities S and Si were detected in all the powders, and traces of Ca, Cr, Cu, Fe, Ni and V were also detected in all powders. Traces of Zn were also found in both recycled powders. Although the quantities of Fe detected in the powders were generally low, the amount of Fe in the recycled powders was higher than in the virgin powders, and had a high standard deviation, indicating uneven distribution of Fe in all the powders. The virgin powders had more traces of Cr compared to the recycled powders.

**Table 4.7** ICP-OES Analysis results for the powders.

| **Element/ wt%** | **NS** | **N** | **R** | **RA** |
|---|---|---|---|---|
| W | 78.17 ±0.12 | 78.60 ± 0.36 | 81.13 ± 0.06 | 82.23 ± 0.84 |
| Co | 6.07 ± 0.11 | 6.05 ± 0.27 | 5.18 ± 0.04 | 7.06 ± 0.10 |
| Ti | 5.91 ± 0.01 | 5.54 ± 0.36 | 5.51 ± 0.05 | 3.76 ± 0.05 |
| Ta | 2.91 ± 0.03 | 2.84 ± 0.27 | 2.97 ± 0.01 | 1.85 ± 0.02 |
| Nb | 0.28 ± 0.01 | 0.27 ± 0.01 | 0.30 ± 0.01 | 0.75 ± 0.01 |
| C | 5.92 ± 0.17 | 6.05 ± 0.08 | 6.40 ± 0.06 | 6.00 ± 0.02 |
| S | 0.011 ± 0.003 | 0.015 ± 0.004 | 0.013 ± 0.006 | 0.021 ± 0.002 |
| Si | 0.13 ± 0.01 | 0.13 ± 0.06 | 0.22 ± 0.08 | - |
| Ca/ ppm | ≤ 10 | ≤ 10 | ≤ 10 | ≤ 10 |
| Cr/ ppm | 401 ± 1 | 468 ± 25 | 144 ± 6 | 259 ± 18 |
| Cu/ ppm | 79 ± 17 | 86 ± 17 | 103 ± 11 | 44 ± 52 |
| Fe/ ppm | 351 ± 131 | 413 ± 184 | 624 ± 231 | 581 ± 234 |
| Ni/ ppm | 311 ± 7 | 345 ± 14 | 363 ± 3 | 342 ± 5 |
| V/ ppm | 14 ± 1 | ≤ 10 | ≤ 10 | 31 ± 1 |
| Zn/ ppm | - | - | 83 ± 7 | 40 ± 9 |

The powder morphology of the four powders is shown in Figure 4.14. The zinc recycled powders, R and RA, generally had predominantly large angular particles compared to the virgin powders NS and N, which had isolated large angular particles amongst the smaller, more rounded particles.

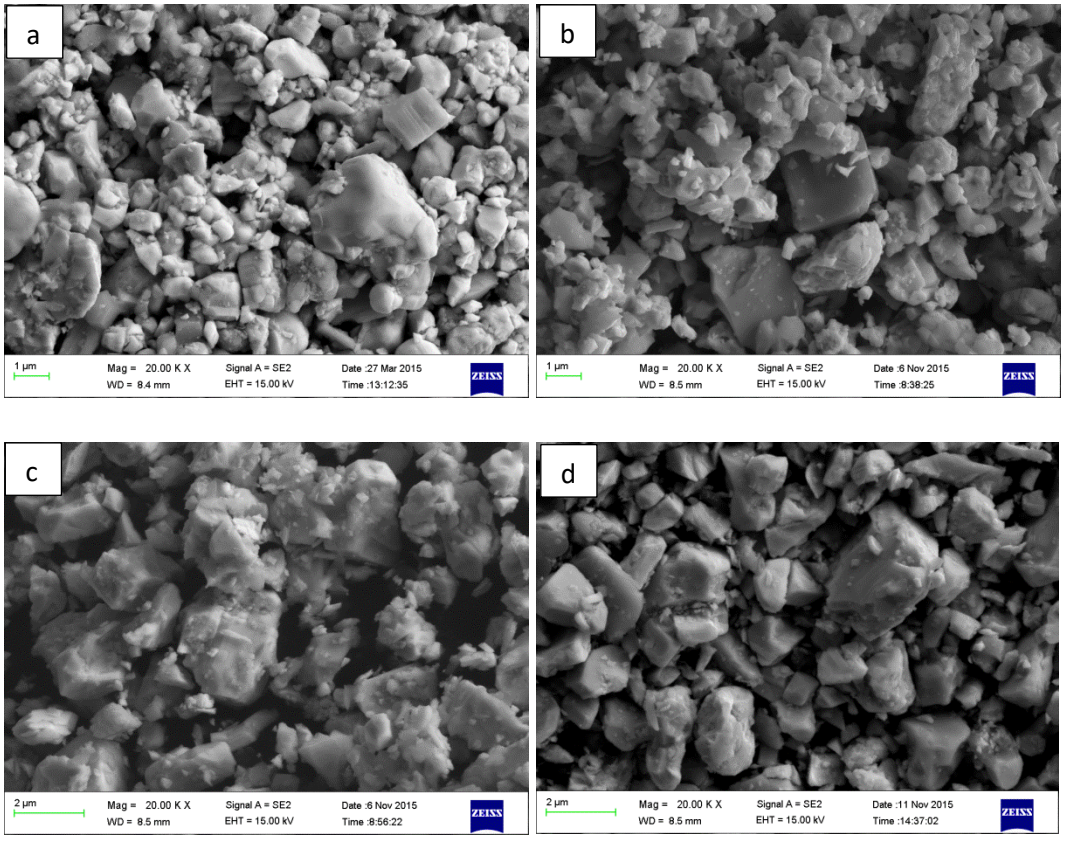



**Figure 4.14** Morphology of un-recycled powders (a) NS and (b) N showing isolated large angular particle, and recycled powders (c) R and (d) RA, showing predominantly large angular particles.

Table 4.8 summarises the composition of the powder determined by EDS. The virgin powder NS had a higher Co content, while RA had a lower W content compared to the other powders. The EDS technique also detected O as a impurity in all powders, and RA had the highest concentration of O. Iron was also detected in higher quantities in the recycled powders R and RA, and a small amount of Fe were detected in the virgin powder NS.

**Table 4.8** EDS analysis results for the powders.

| Element / wt% | NS | N | R | RA |
|---|---|---|---|---|
| **W** | 67.42 ± 0.26 | 69.68 ± 0.13 | 66.71 ± 0.43 | 61.35 ± 0.82 |
| **Co** | 10.83 ± 0.29 | 7.02 ± 0.95 | 6.30 ± 0.11 | 8.06 ± 0.32 |
| **Ti** | 5.81 ± 0.05 | 5.70 ± 0.11 | 4.72 ± 0.06 | 4.44 ± 0.18 |
| **Ta** | 2.48 ± 0.08 | 1.88 ± 0 | 2.35 ± 0.09 | 1.60 ± 0.14 |
| **Nb** | 0.60 ± 0.08 | 0.67 ± 0 | 0.65 ± 0.13 | 0.47 ± 0.08 |
| **O** | 2.72 ± 0.23 | 3.36 ± 0.03 | 3.42 ± 0.17 | 5.86 ± 0.26 |
| **Fe** | 0.04 ± 0 | - | 0.11 ± 0.03 | 0.13 ± 0 |

Figure 4.15 shows the XRD plots of the powders. The major phases that were identified in all the powders include WC, TiC and Co. The XRD technique confirmed Fe build up in the recycled powders R and RA, which identified FeO as an additional phase in the recycled powders.

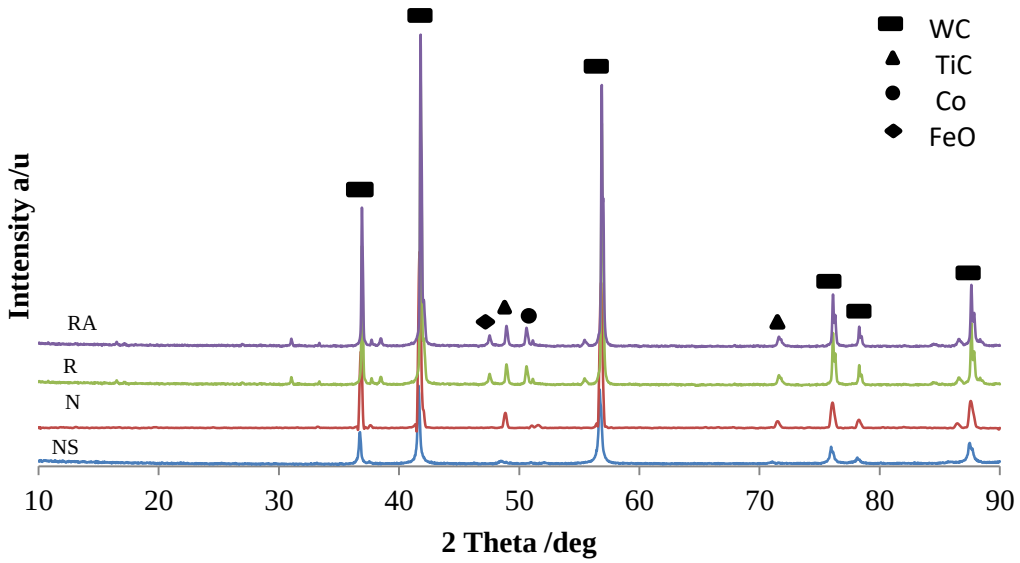



**Figure 4.15** The XRD plots of the powders showing WC, TiC, Co and FeO peaks.

Table 4.9 summarises the quantities of major, impurity and trace elements that were detected by the micro-PIXE technique, while Figures 4.16 - 4.19 show the micro-PIXE elemental distribution maps of the major and trace elements within the virgin powders NS and N and recycled powders R and RA for 2.3 x 2.3 mm regions that were selected in the compacted powder. On a large scale, there was general homogeneity of the major elements W, Co, Ti, Ta and Nb, as well as the impurity and trace elements in all the powders.

**Table 4.9** Micro-PIXE elemental analysis of powders

| **Element** | **NS** | **N** | **R** | **RA** |
|---|---|---|---|---|
| $W_L$/ wt% | 75.46 | 70.63 | 73.94 | 69.47 |
| Co/ wt% | 6.47 | 7.45 | 4.88 | 6.45 |
| Ti/ wt% | 5.23 | 5.38 | 5.14 | 4.44 |
| $Ta_L$/ wt% | 2.47 | 2.34 | 2.44 | 2.27 |
| Nb/ wt% | 0.19 | 0.02 | 0.20 | 0.12 |
| S/ wt% | 0.67 | 0.67 | 0.77 | 0.72 |
| Cr/ wt% | 0.1386 | 0.1341 | 0.28 | 0.02 |
| Fe/ wt% | 0.0533 | 0.0298 | 0.90 | 0.09 |
| Mn/ ppm | 37 | 17 | 265 | 37 |
| Ni/ ppm | <337 | <355 | 638 | 191 |
| K/ ppm | 104 | - | 150 | - |
| Ca/ ppm | 81 | 310 | 152 | 154 |
| Cl/ ppm | 427 | - | <223 | - |
| Zn/ ppm | - | - | - | 757 |

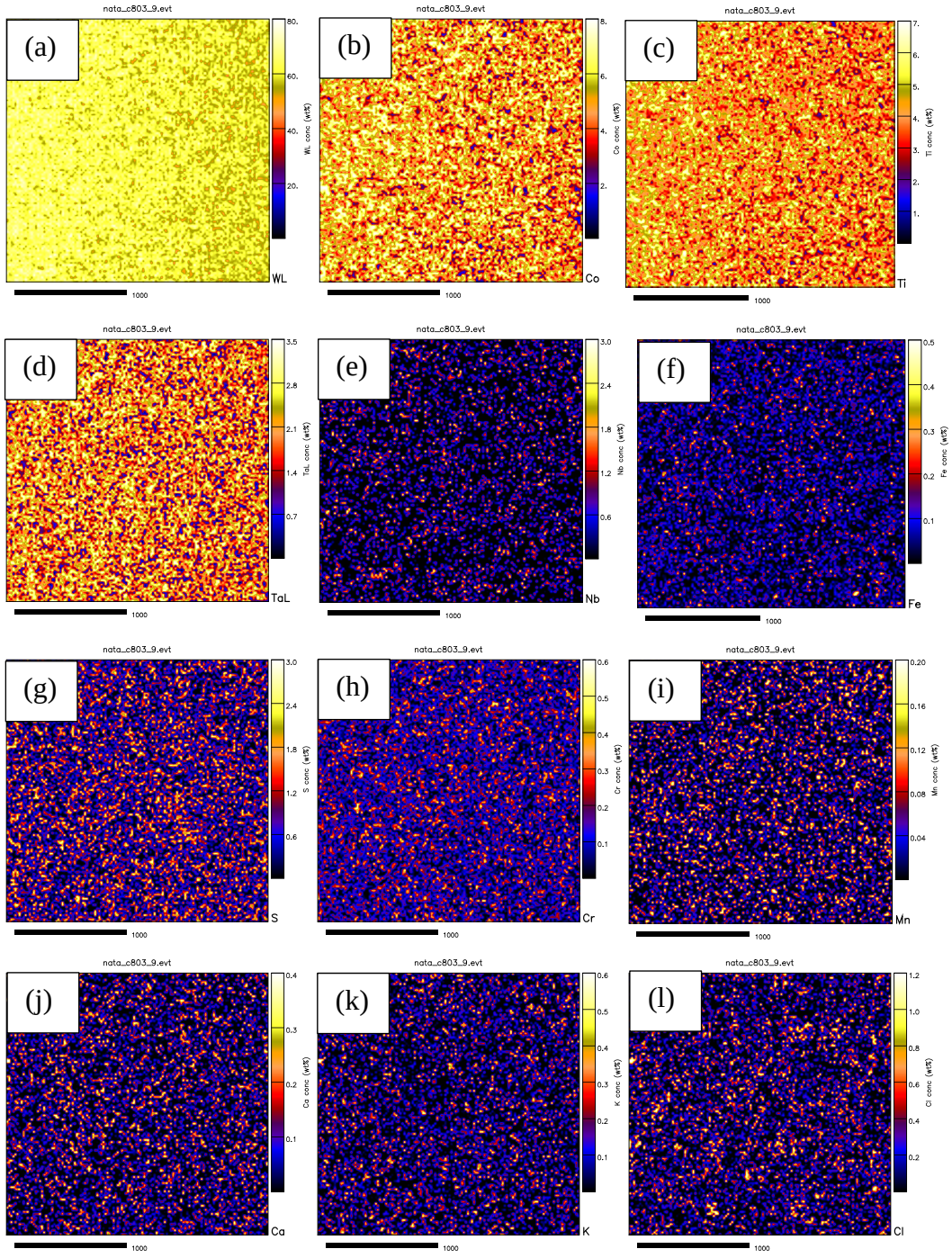



**Figure 4.16** Micro-PIXE elemental distribution maps on a 2.3 mm x 2.3 mm area in the virgin powder NS, showing the major elements (a) $W_L$, (b) Co, (c) Ti, (d) $Ta_L$ and (e) Nb, and impurities (f) Fe, (g) S, (h) Cr, (i) Mn, (j) Ca, (k) K and (l) Cl. Yellow areas indicate regions of high concentration and dark areas indicate region of low concentration of a given element.

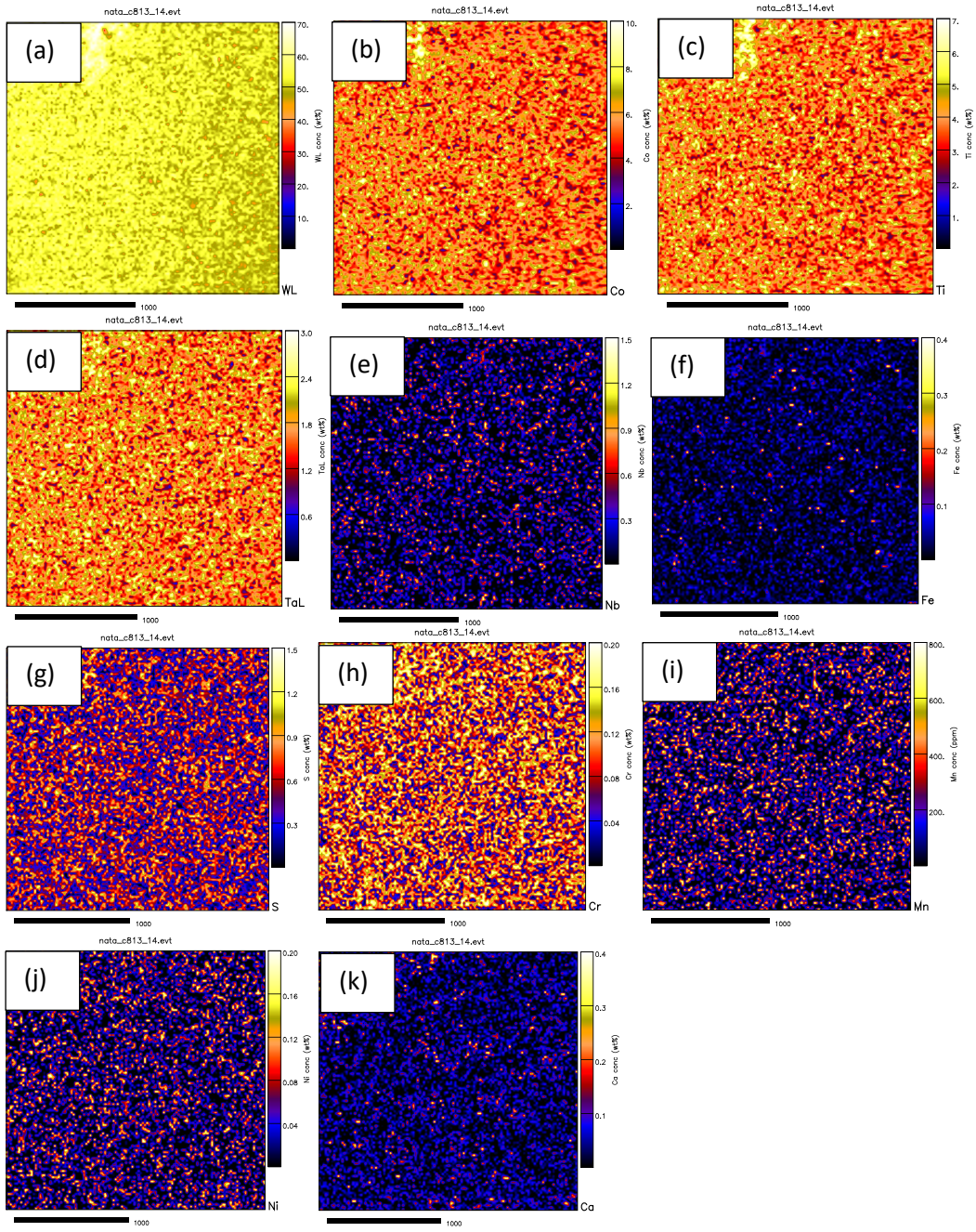



**Figure 4.17** Micro-PIXE elemental distribution maps on a 2.3 mm x 2.3 mm area in the virgin powder N, showing the major elements (a) $W_L$, (b) Co, (c) Ti, (d) $Ta_L$ and (e) Nb, and impurities (f) Fe, (g) S, (h) Cr, (i) Mn, (j) Ni and (k) Ca. Yellow areas indicate regions of high concentration and dark areas indicate region of low concentration of a given element.

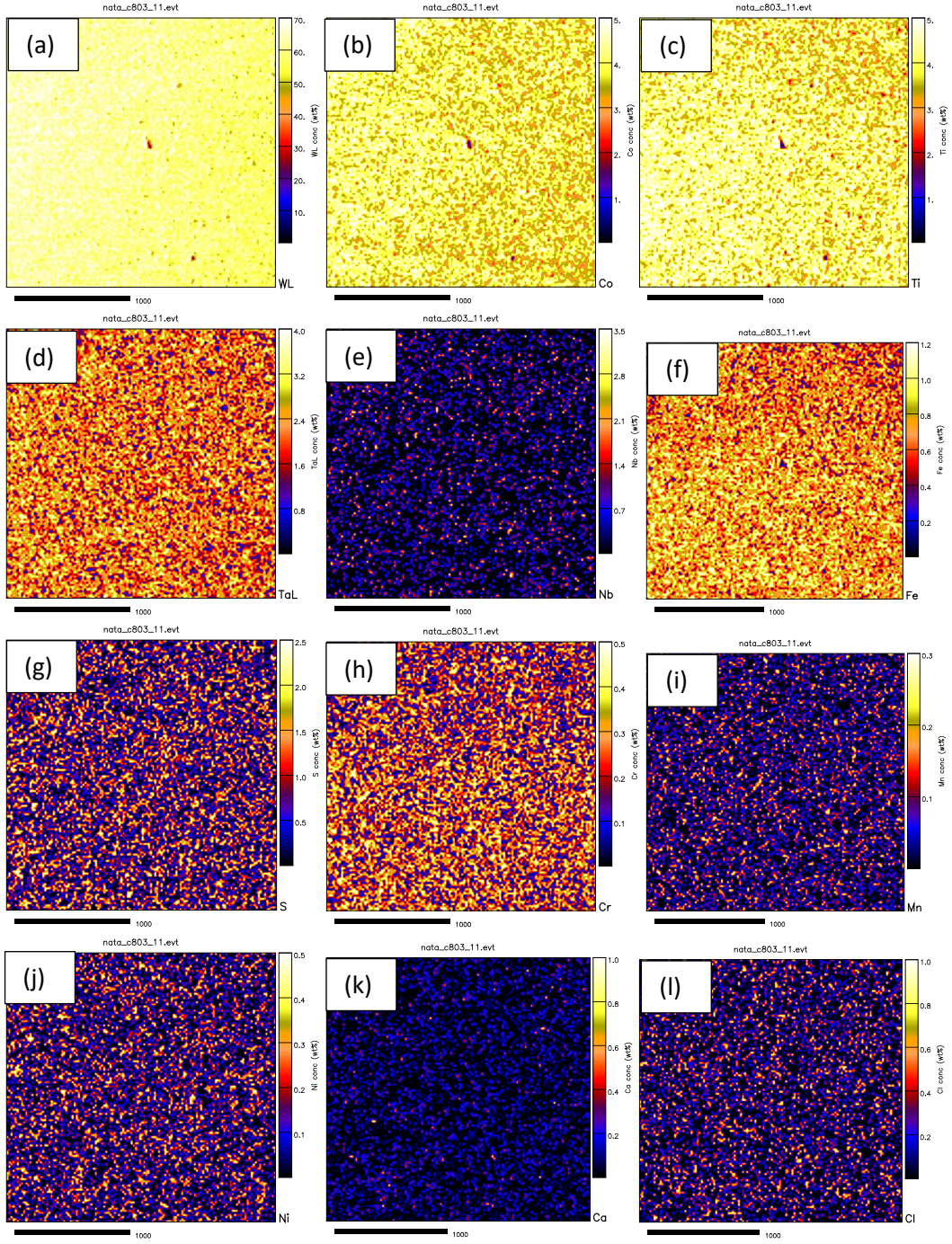



**Figure 4.18** Micro-PIXE elemental distribution maps on a 2.3 mm x 2.3 mm area in the recycled powder R, showing the major elements (a) $W_L$, (b) Co, (c) Ti, (d) $Ta_L$ and (e) Nb, and impurities (f) Fe, (g) S, (h) Cr, (i) Mn, (j) Ni and (k) Ca and (l) Cl. Yellow areas indicate regions of high concentration and dark areas indicate region of low concentration of a given element.

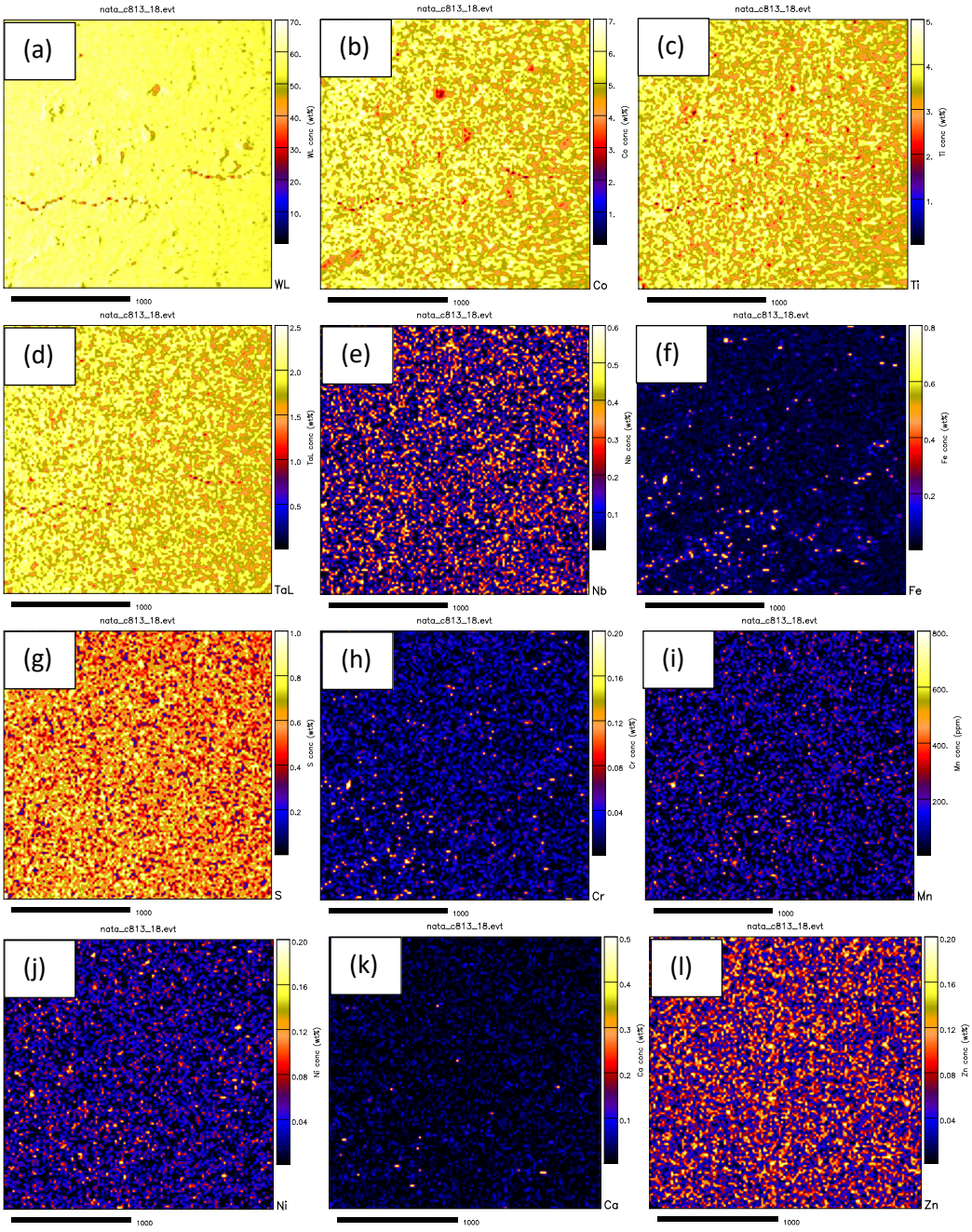



**Figure 4.19** Micro-PIXE elemental distribution maps on a 2.3 mm x 2.3 mm area in the recycled powder RA, showing the major elements (a) $W_L$, (b) Co, (c) Ti, (d) $Ta_L$ and (e) Nb, and impurities (f) Fe, (g) S, (h) Cr, (i) Mn, (j) Ni and (k) Ca and (l) Zn. Yellow areas indicate regions of high concentration and dark areas indicate region of low concentration of a given element.

Figures 4.20 – 4.23 show smaller areas of about 86 x 86 μm selected for micro-PIXE elemental distribution in the powders. Better homogeneity of elements in the recycled powders R and RA was observed compared to the un-recycled powders NS and N. This is evident especially from Co and Ti maps in the un-recycled powders NS and N, where pools of Co and Ti were observed. The maps of impurity elements Fe, S, Cr, Mn, Ni, K, Ca, Cl and Zn are also included for the respective powders. Pools of Fe and Cr were observed in the un-recycled powder N, and the impurity elements were generally evenly distributed in all the other powders.

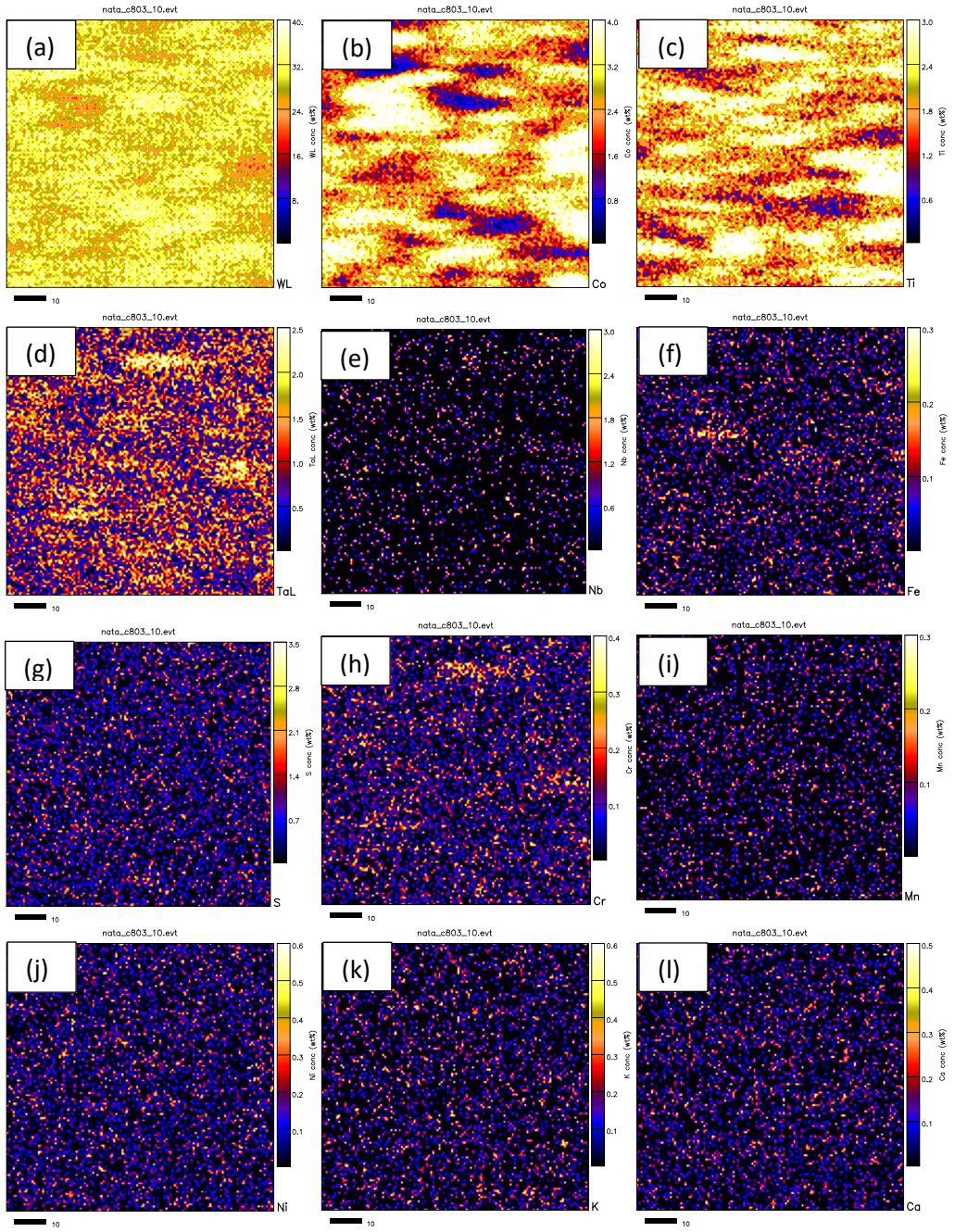



**Figure 4.20** Micro-PIXE elemental distribution maps on a 86 μm x 86 μm area in the virgin powder NS, showing the major elements (a) $W_L$, (b) Co, (c) Ti, (d) $Ta_L$ and (e) Nb, and impurities (f) Fe, (g) S, (h) Cr, (i) Mn, (j) Ni, (k) K and (l) Ca. Yellow areas indicate regions of high concentration and dark areas indicate region of low concentration of a given element.

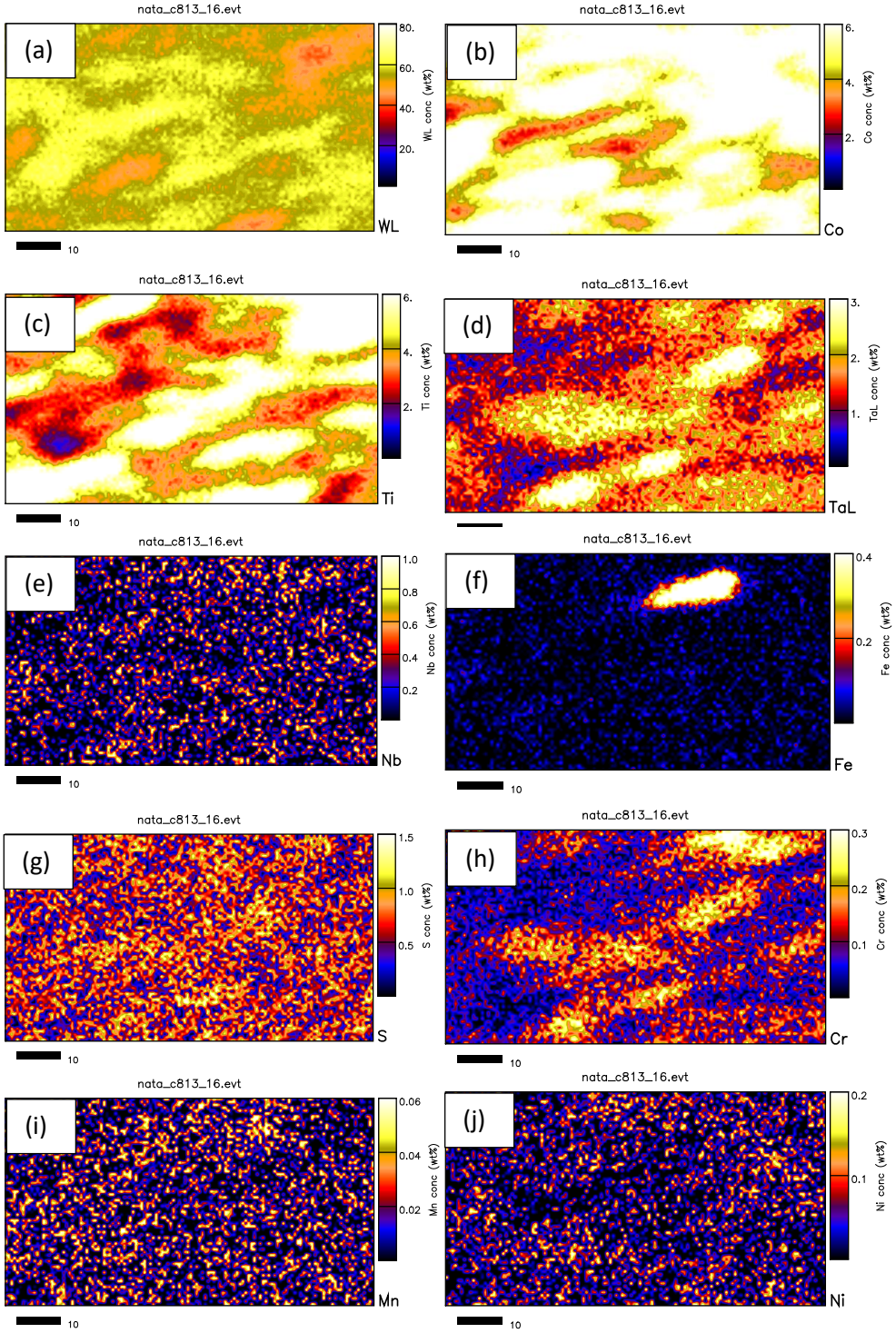



**Figure 4.21** Micro-PIXE elemental distribution maps on a 86 µm x 46 µm area in the virgin powder N, showing the major elements (a) $W_L$, (b) Co, (c) Ti, (d) $Ta_L$ and (e) Nb, and impurities (f) Fe, (g) S, (h) Cr, (i) Mn and (j) Ni. Yellow areas indicate regions of high concentration and dark areas indicate region of low concentration of a given element.

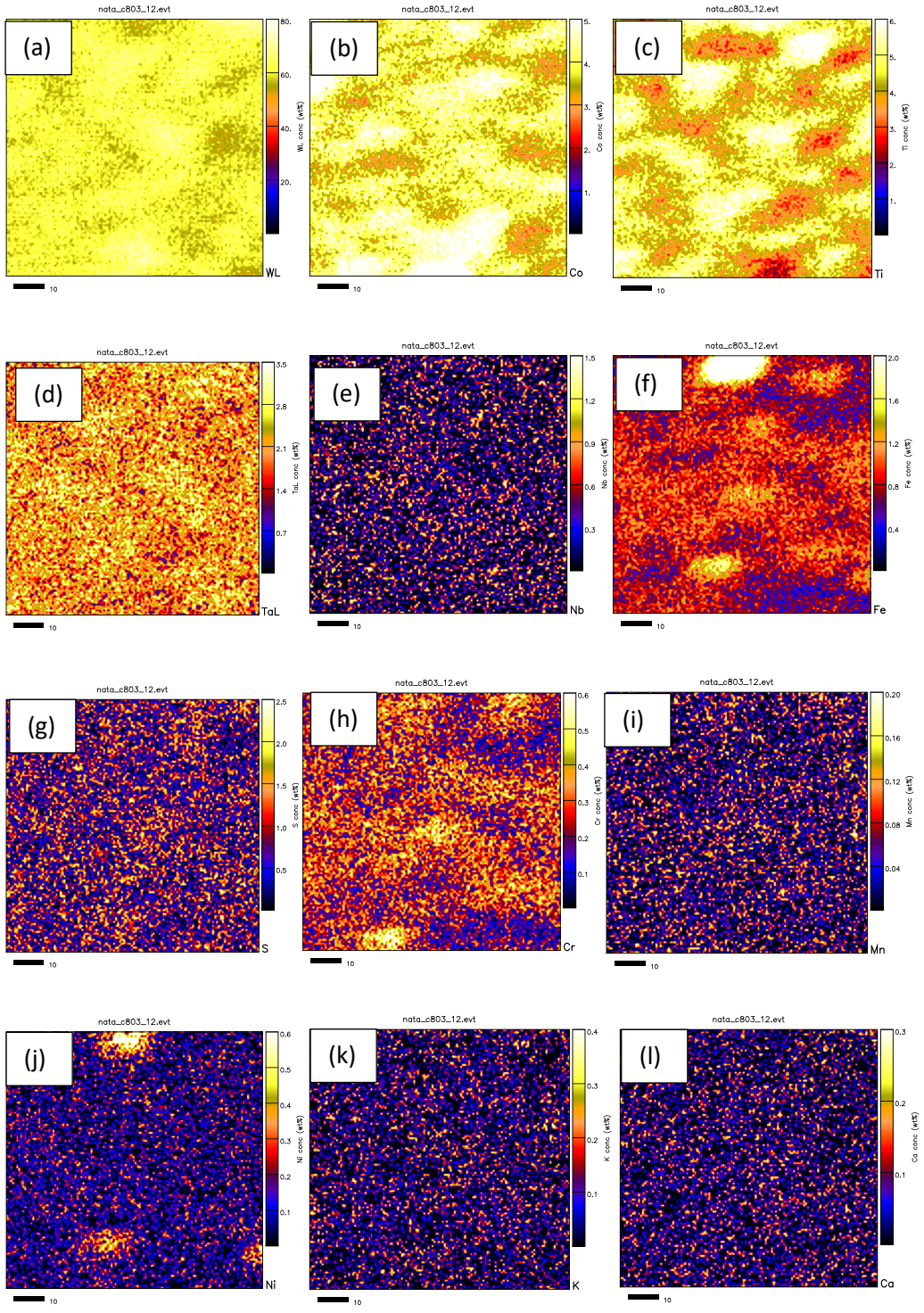



**Figure 4.22** Micro-PIXE elemental distribution maps on a 86 μm x 86 μm area in the recycled powder R, showing the major elements (a) $W_L$, (b) Co, (c) Ti, (d) $Ta_L$ and (e) Nb, and impurities (f) Fe, (g) S, (h) Cr, (i) Mn, (j) Ni and (k) K and (l) Ca. Yellow areas indicate regions of high concentration and dark areas indicate region of low concentration of a given element.

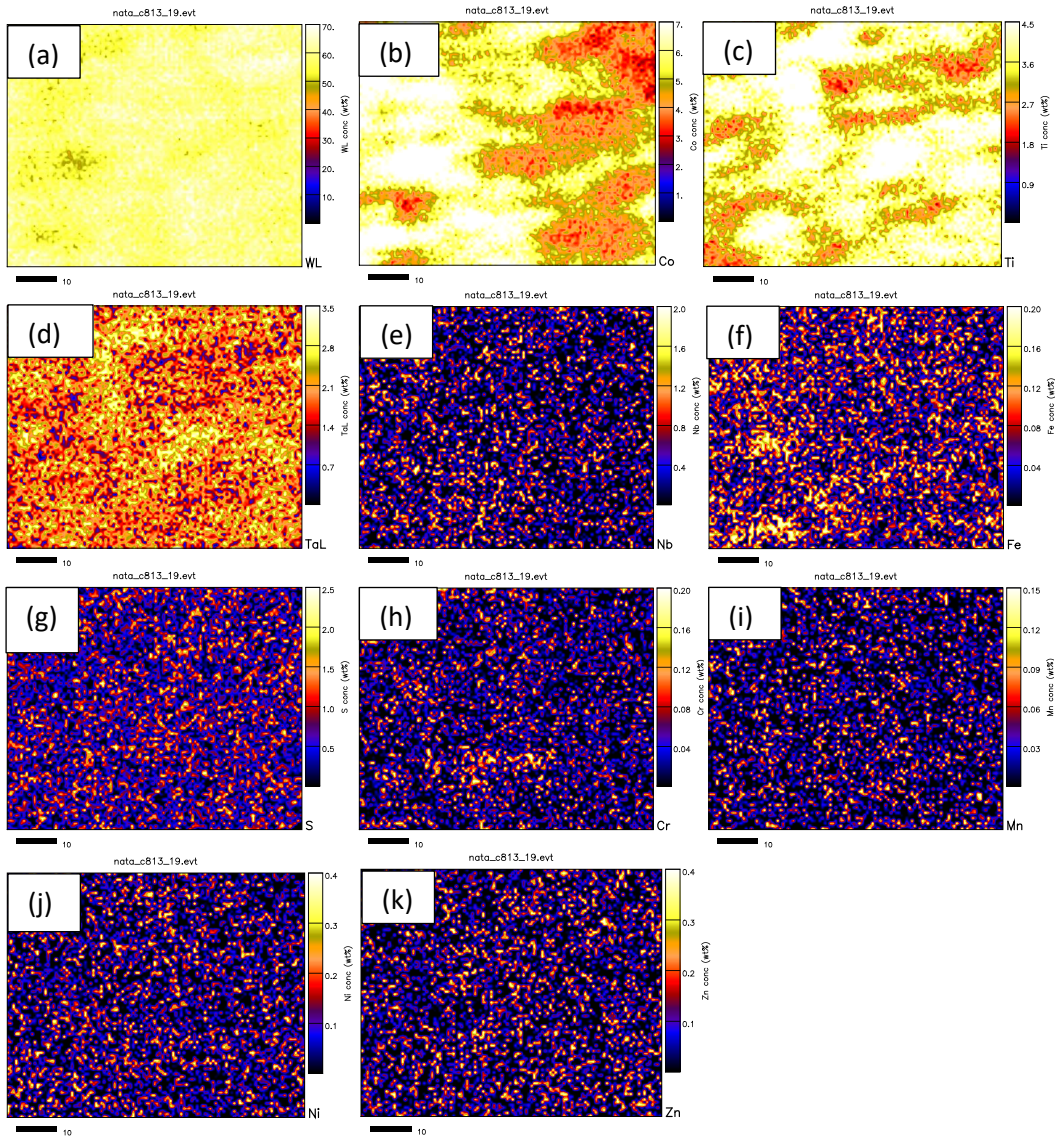



**Figure 4.23** Micro-PIXE elemental distribution maps on a 86 μm x 61 μm area in the recycled powder RA, showing the major elements (a) $W_L$, (b) Co, (c) Ti, (d) $Ta_L$ and (e) Nb, and impurities (f) Fe, (g) S, (h) Cr, (i) Mn, (j) Ni and (k) Zn. Yellow areas indicate regions of high concentration and dark areas indicate regions of low concentration of a given element.

### 4.4.1 Green density of compacted powders

The green densities of the compacted powders were determined according to standard ASTM B610-08 [70]. Table 4.10 presents the average green densities of the compacted powders, and Table B1 in Appendix B shows the dimensions of the green compacts for the four powders. The green densities ranged from 6.7 – 7.8 g/cm$^3$, and the recycled powder RA had the lowest green density. The standard deviations of the green densities of recycled powders R and RA were about 40 % higher than those for the virgin powders NS and N, indicating more variation in the green densities of the recycled powders R and RA.

**Table 4.10** Green densities of compacted powders.

| **Powder** | **Green density/ gcm$^{-3}$** |
|---|---|
| **NS** | 7.529 ± 0.087 |
| **N** | 7.846 ± 0.090 |
| **R** | 7.743 ± 0.163 |
| **RA** | 6.757 ± 0.130 |

## 4.5 Characterization of sintered alloys

This section presents the findings from the characterization processes that were carried out on the sintered alloys. Detailed microstructural, physical, mechanical and magnetic characterization was carried out to evaluate the properties of the sintered alloys.

### 4.5.1 Microstructural characterization

The FESEM was used to characterize the microstructure of the sintered alloys. Figure 4.24 shows the FESEM micrographs of the sintered samples. The EDS technique identified the light grey phase as WC with cubic carbides concentrated around the edges, while the dark areas were identified as the Co binder. The un-recycled alloys NS and N, shown in Figure 4.24 (a) and (b), had isolated large WC grains surrounded by smaller WC grains. The recycled alloys, R and RA, shown in Figure 4.24 (c) and (d), also had large isolated WC grains, but the surrounding WC smaller grains were coarser compared to the un-recycled alloys.

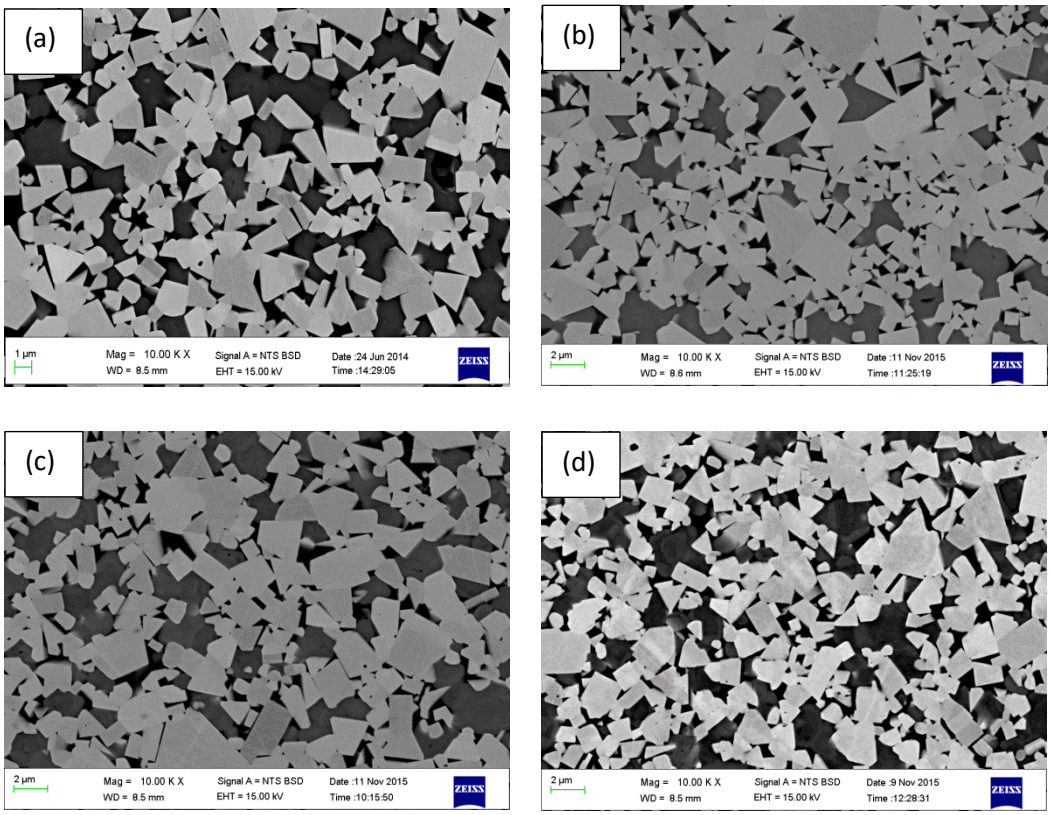



**Figure 4.24** FESEM micrographs of (a) NS, (b) N, (c) R and (d) RA, showing the light WC phase and the dark Co binder.

Table 4.11 shows the composition of each alloy determined by EDS. The quantities of the major elements (W, Co, Ti, Ta and Nb) had generally similar values in all the alloys. For instance, W was about 80 wt % in all the alloys. About 0.1 wt % of Fe were detected in the recycled alloys R and RA.

**Table 4.11** EDS analysis of sintered alloys.

| Element/ wt% | NS | N | R | RA |
|---|---|---|---|---|
| **W** | 78.12 ± 0.43 | 78.11 ± 0.25 | 80.82 ± 0.29 | 79.41 ± 0.12 |
| **Co** | 6.87 ± 0.07 | 6.81 ± 0.10 | 5.84 ± 0.14 | 7.47 ± 0.11 |
| **Ti** | 4.73 ± 0.05 | 4.76 ± 0.08 | 4.64 ± 0.01 | 4.51 ± 0.03 |
| **Ta** | 1.49 ± 0.08 | 1.57 ± 0.14 | 1.20 ± 0.03 | 1.08 ± 0.11 |
| **Nb** | 0.76 ± 0.06 | 0.61 ± 0.01 | 0.68 ± 0.11 | 0.68 ± 0.14 |
| **C** | 8.03 ± 0.47 | 8.09 ± 0.15 | 6.78 ± 0.30 | 6.77 ± 0.27 |
| **Fe** | - | - | 0.10 ± 0.00 | 0.08 ± 0.00 |

Micrographs taken by FESEM to incorporate the edge of each sample, shown in Figure 4.25, revealed a variation in microstructure from the edge moving into the bulk of the samples. The surface layer of each sample had closely packed WC grains such that very small isolated Co binder areas were visible. Smaller isolated binder areas were visible in the surface layer of the un-recycled alloys NS and N, compared to the recycled alloys, R and RA. The EDS analysis results, shown in Table 4.12, confirmed that this layer had a high Co concentration in all alloys, and had none or low concentrations of the cubic carbide formers Ti and Ta, indicating that a carbide free layer (CFL) was formed.

Niobium was not detected in the CFL of the un-recycled alloy NS, and was about 0.3 wt % in alloys N, R and RA. Fe was detected as an impurity in the CFL of the recycled alloys R and RA, and traces of Ni were detected in the CFL of R. Table 4.12 shows the average width of the CFL in each alloy. The CFL for the un-recycled alloys NS and N was about 10 µm wider than the CFL for the recycled alloys R and RA.

**Table 4.12** CFL width and EDS analysis results.

| | NS | N | R | RA |
|---|---|---|---|---|
| **Average CFL width/ µm** | 32.35 ± 1.91 | 32.56 ± 2.29 | 22.88 ± 1.41 | 21.29 ± 1.76 |
| | **Element/ wt%** | | | |
| **Element/ wt%** | **NS** | **N** | **R** | **RA** |
| **W** | 81.14 ± 1.60 | 81.33 ± 0.48 | 82.58 ± 1.10 | 82.70 ± 0.22 |
| **Co** | 9.79 ± 1.37 | 9.92 ± 0.25 | 10.90 ± 0.99 | 10.62 ± 0.13 |
| **Ti** | 0.29 ± 0.00 | 0.09 ± 0.00 | 0.49 ± 0.26 | 0.06 ± 0.02 |
| **Ta** | - | - | - | - |
| **Nb** | - | 0.30 ± 0.00 | 0.38 ± 0.18 | 0.29 ± 0.09 |
| **C** | 7.82 ± 2.00 | 8.36 ± 0.62 | 5.46 ± 0.18 | 6.17 ± 0.11 |
| **Fe** | 0.07 ± 0.03 | - | 0.12 ± 0.03 | 0.15 ± 0.04 |
| **Ni** | - | - | 0.06 ± 0.00 | - |

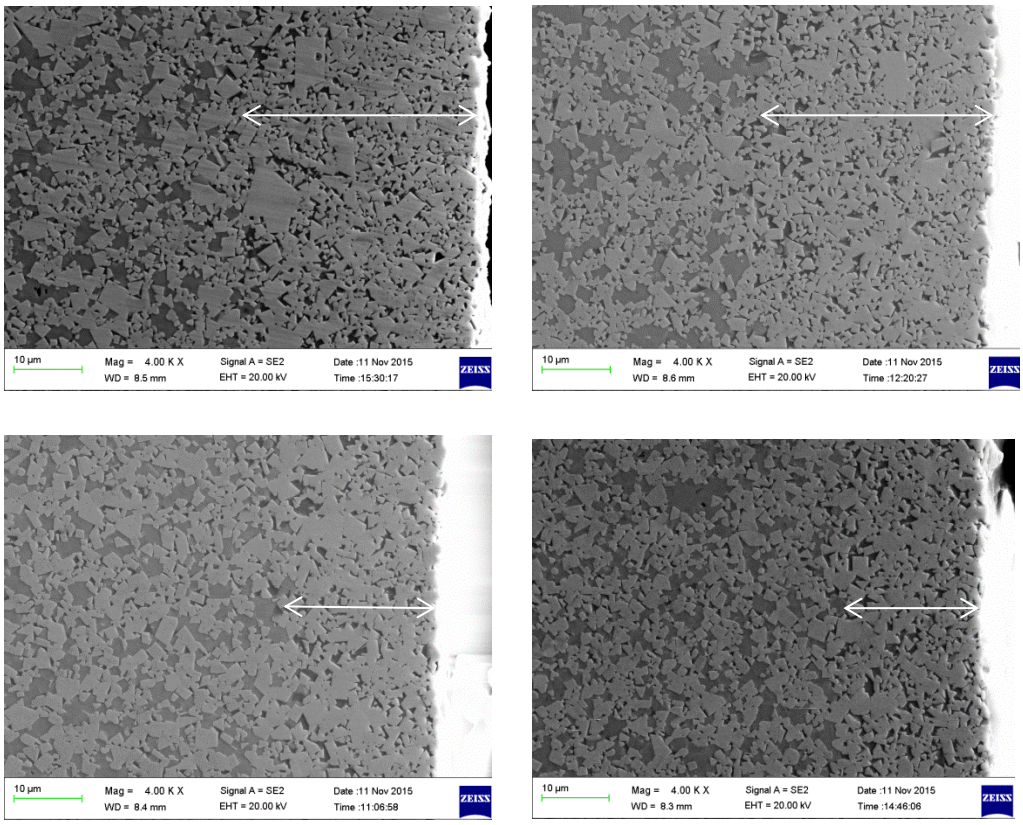



**Figure 4.25** FESEM micrographs showing the cubic free layer in (a) NS, (b) N, (c) R and (d) RA. The arrows indicate the thickness of the cubic free layer in each sample.

Figure 4.26 shows the XRD patterns for the sintered alloys. A similar pattern was obtained for all four alloys, and the major peaks were identified as WC and the minor peaks as TiC and Co. The phases TaC and NbC, which were part of the composition in all the alloys, were not detected. This was because, from EDS (refer to Table 4.11), the Ta concentration was about 1 wt% and the Nb concentration was about 0.3 wt % in all the alloys. These concentrations fell below the detection limit of the XRD machine, which requires at least 1 wt % concentration of a given phase. For the same reason, no impurity phases were detected in all samples.

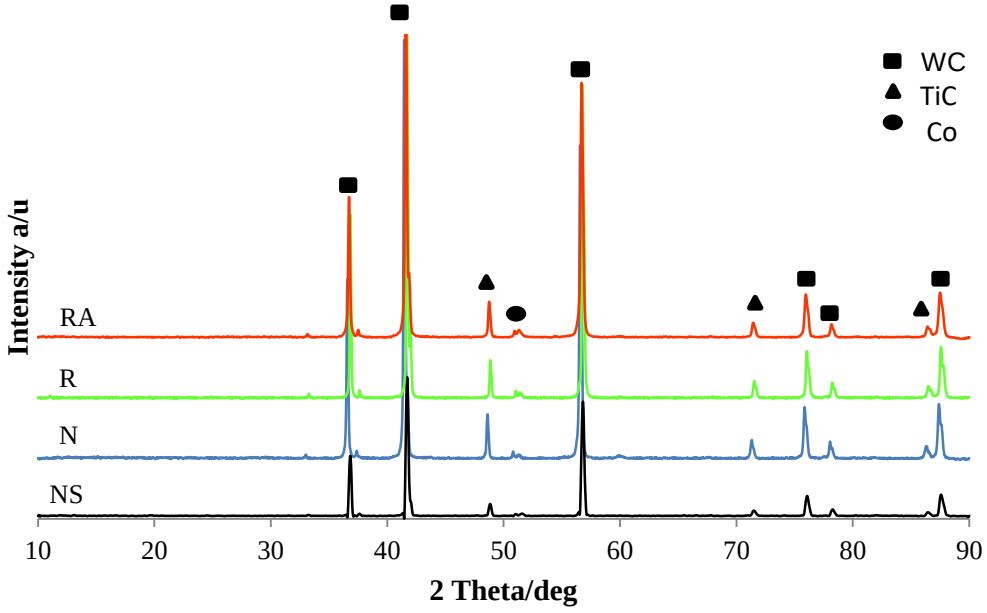



**Figure 4.26** XRD patterns for alloys NS, N, R and RA showing the WC, TiC and Co peaks.

The microstructural parameters, namely WC grain size, WC contiguity and binder mean free path are listed in Table 4.13. Although the FESEM micrographs showed coarser WC grains in the recycled alloys R and RA, the average carbide grain sizes were about 2 µm for the recycled alloys and recycled alloy N. Alloy NS had a slightly smaller average carbide grain (1.9 µm) size compared to the other alloys. The standard deviations for the respective grain sizes are significant,

indicating a wide variation in the carbide grain sizes in all the alloys. While alloys NS, R and RA had a carbide contiguity of about 0.52, alloy RA had a lower contiguity (0.46). There is also significant variation in the carbide contiguity values in all alloys, as indicated by the standard deviations. The binder mean free path of the alloys ranged from 0.12 -0.16 μm, and recycled alloy RA had the longest mean free path (0.16 um) compared to the other alloys.

**Table 4.13** Mean carbide grain size, carbide contiguity and binder mean free path of sintered alloys.

| Alloy | Mean carbide grain/ size/ μm | WC contiguity | Binder mean free path/ μm |
|---|---|---|---|
| **NS** | 1.90 ± 0.39 | 0.54 ± 0.12 | 0.12 ± 0.04 |
| **N** | 2.01 ± 0.33 | 0.53 ±0.14 | 0.14 ± 0.04 |
| **R** | 2.07 ± 0.33 | 0.52 ± 0.13 | 0.12 ± 0.04 |
| **RA** | 2.04 ± 0.31 | 0.46 ± 0.18 | 0.16 ± 0.04 |

Figures 4.27 – 4.30 show the optical micrographs of the sintered materials, as well as the PIXE elemental distribution maps of the major and impurity elements. The optical micrographs of all alloys showed the CFL as the light band at the edge of the samples, and the dark mixed crystal carbides concentrated away from the edge of the samples. The CFL in the recycled alloy RA, shown in Figure 4.30, indicated the presence of dark mixed crystal carbides, while the CFL in the alloys NS, N and RA did not show the presence of mixed crystal carbides. In the un-recycled alloys NS and N (Figure 4.27(a) and 4.28 (a)), the optical micrographs showed segregation of the mixed crystal carbides going into the bulk of the material, while the mixed crystal carbides were more evenly distributed in the recycled alloys R and RA (Figure 4.29 (a) and 4.30 (a)).

The PIXE elemental distribution maps show the exact location of individual elements in the materials. Bright areas show regions of high concentration, while dark areas show regions of very low concentration of elements. As shown in Figure 4.27(b) – 4.30(b), $W_L$ maps showed even distribution in both the recycled and un-recycled alloys. As shown in the Ti maps in Figures 4.27(d) – 4.30(d), there was no Ti in the CFL, while very small quantities of Ta and Nb were present in the CFL in both the recycled and un-recycled materials. The Co maps showed high concentrations of Co in the CFL in all the materials, depletion in regions next to the CFL, and an uneven distribution of small Co pools elsewhere within the alloys.

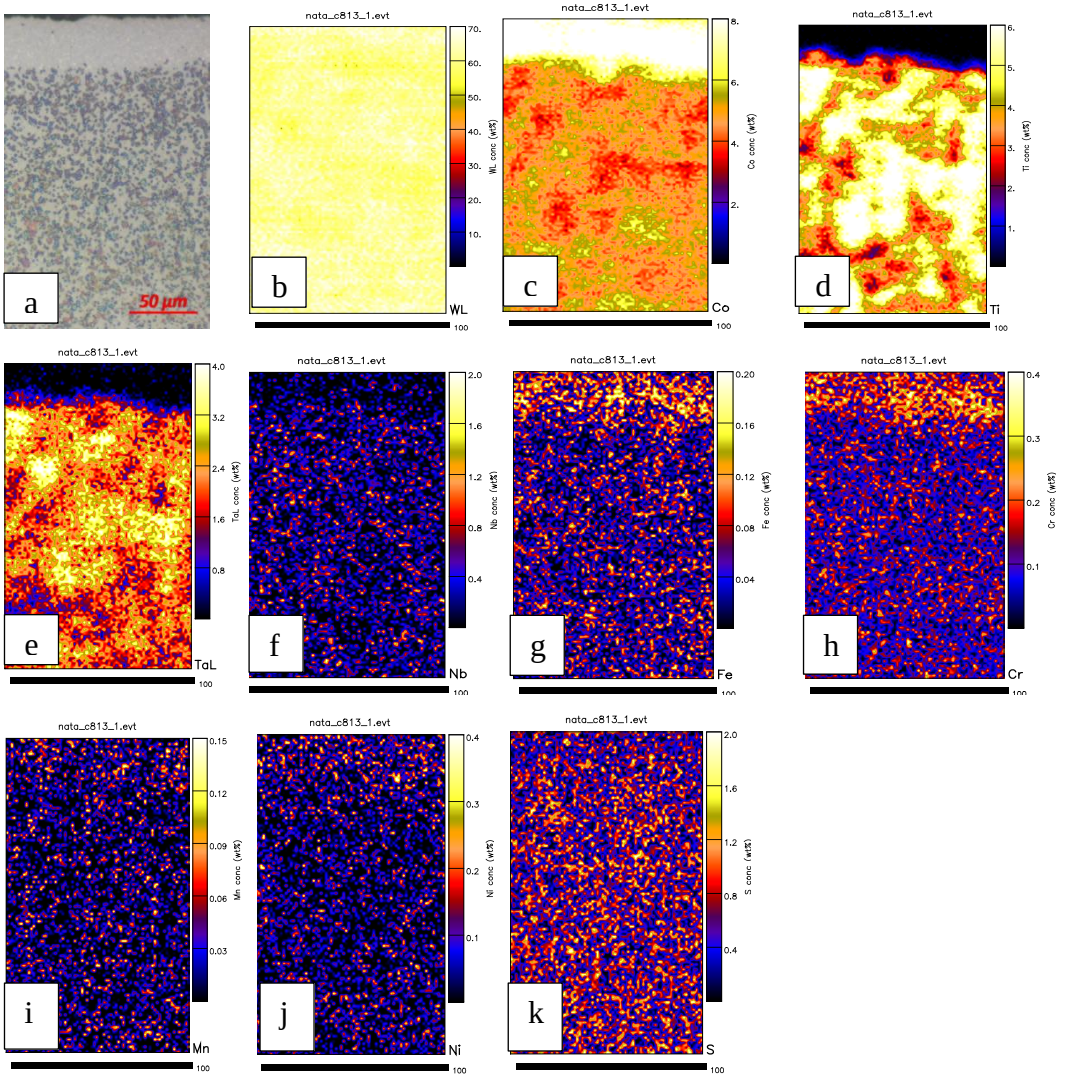



**Figure 4.27 (**a) Optical micrograph of alloy NS, and PIXE distribution maps of major elements (b) Tungsten 'L' ($W_L$), (c) Co, (d) Ti, (e) Tantalum 'L' ($Ta_L$), and (f) Nb, and impurities (g) Fe, (h) Cr, (i) Mn, (j) Ni and (k) S. Yellow areas indicate regions of high concentration and dark areas indicate regions of low concentration of a given element.

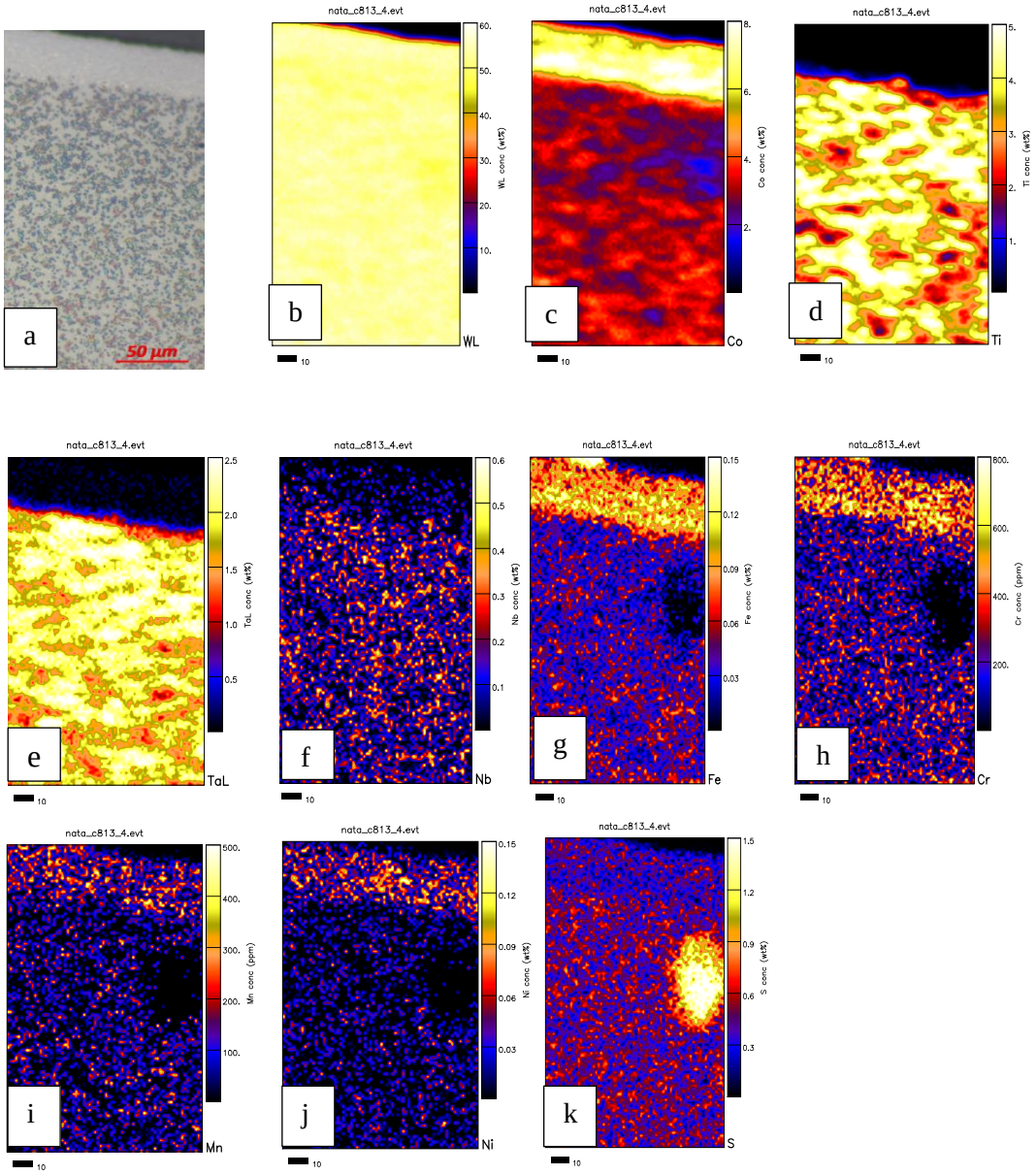



**Figure 4.28 (**a) Optical micrograph of alloy N, and PIXE distribution maps of major elements (b) Tungsten 'L' ($W_L$), (c) Co, (d) Ti, (e) Tantalum 'L' ($Ta_L$), and (f) Nb, and impurities (g) Fe, (h) Cr, (i) Mn, (j) Ni and (k) S. Yellow areas indicate regions of high concentration and dark areas indicate regions of low concentration of a given element.

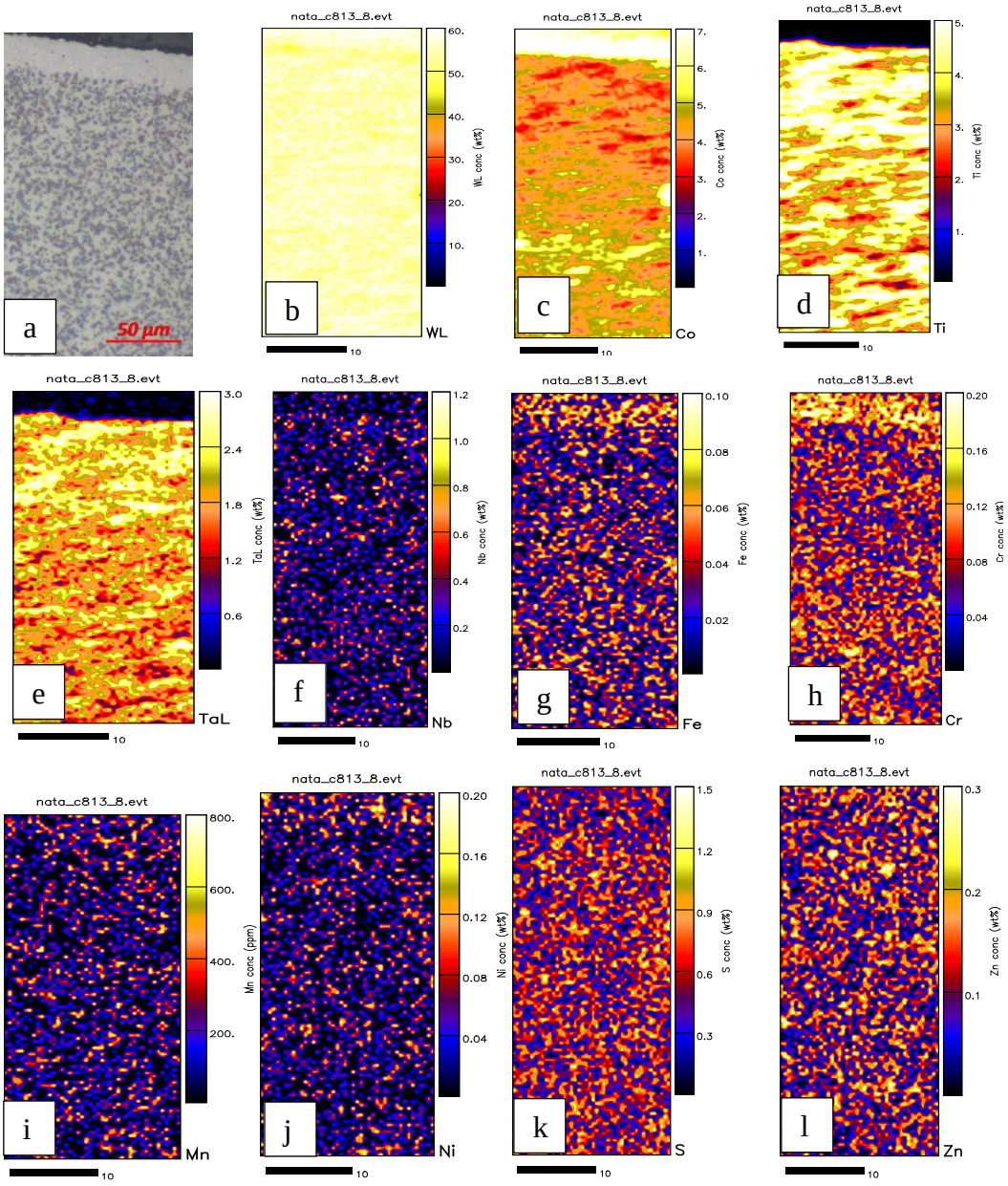



**Figure 4.29 (**a) Optical micrograph of alloy R, and PIXE distribution maps of major elements (b) Tungsten 'L' ($W_L$), (c) Co, (d) Ti, (e) Tantalum 'L' ($Ta_L$), and(f) Nb, and impurities (g) Fe, (h) Cr, (i) Mn, (j) Ni, (k) S and (l) Zn. Yellow areas indicate regions of high concentration and dark areas indicate regions of low concentration of a given element.

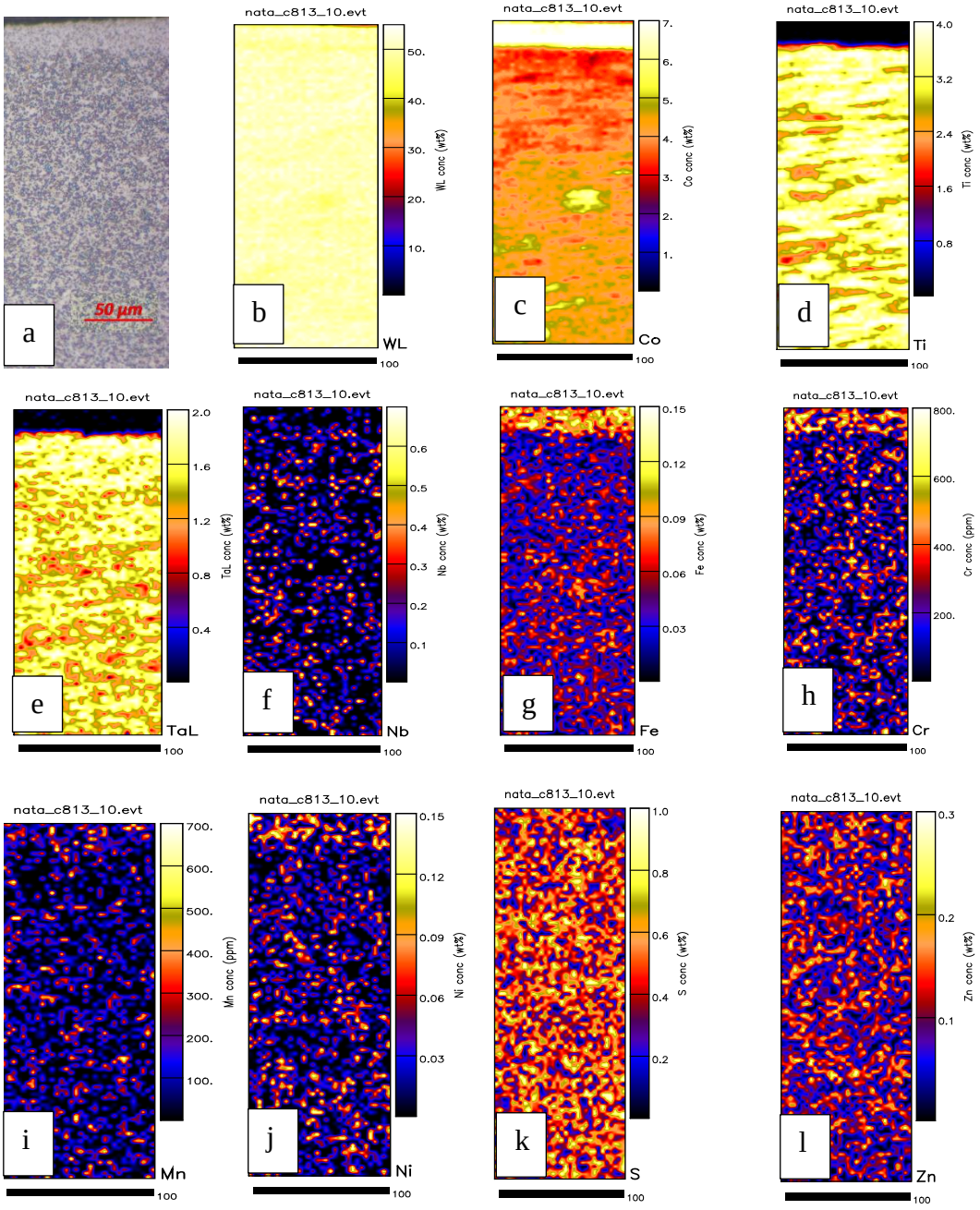



**Figure 4.30 (**a) Optical micrograph of alloy RA, and PIXE distribution maps of (b) Tungsten 'L' ($W_L$), (c) Co, (d) Ti, (e) Tantalum 'L' ($Ta_L$), (f) Nb, (g) Fe, (h) Cr, (i) Mn, (j) Ni, (k) S and (l) Zn. Yellow areas indicate regions of high concentration and dark areas indicate regions of low concentration of a given element.

Figure 4.31 shows points that were selected for spot elemental analysis in the PIXE Ti map of each alloy, starting from the CFL going into the bulk to about the same depth in all samples. Table 4.14 shows the amounts of Co at position one ($Co_1$) and Ti at position two ($Ti_2$) in Figure 4.31, as well as the $Co_1/Ti_2$ ratio. As expected, the cobalt content at position 1, ($Co_1$), was quite high, ranging from 6.23-9.67 wt % in the CFL (position 1). The titanium content, ($Ti_2$), had the highest amount just below the CFL, at position 2, for all the samples, ranging from 3.83 – 7.25 wt %. The elements Co and Ti were selected because they are most affected by the preferential diffusion process in response to nitrogen diffusion during sintering [19-24]. A $Co_1/Ti_2$ ratio of 1.3 was obtained for the un-recycled alloys NS and N and recycled alloy R, while recycled RA had a higher ratio of 1.84.

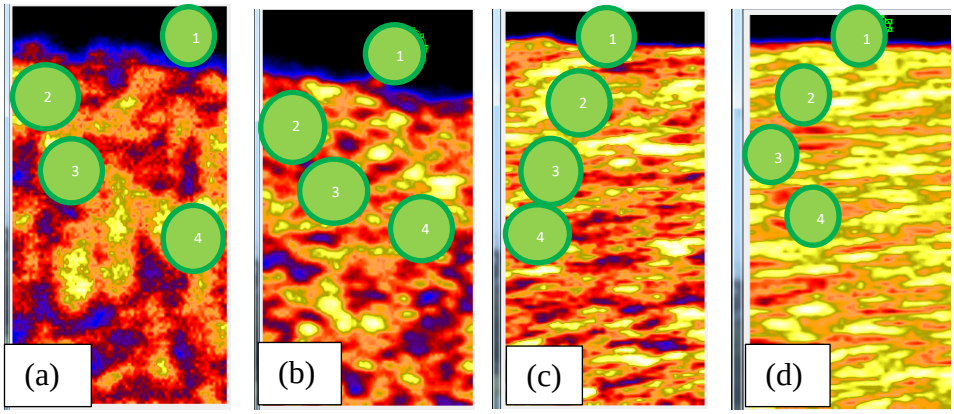



**Figure 4.31:** Micro-PIXE analysis of selected points on Ti maps, 1: in the CFL, 2: just below the CFL 3 and 4: into the bulk. Image sequence is (a) selected points in alloy NS, (b) selected points in alloy N, (c) selected points in alloy R, and (d) selected points in alloy RA.

**Table 4.14** Cobalt and titanium content in the CFL (point 1) and just below the CFL (point 2) respectively.

| Alloy | Co content in CFL ($Co_1$) / wt % | Ti content at B ($Ti_2$) / wt % | Ratio of $Co_1/Ti_2$ |
|---|---|---|---|
| **NS** | 9.67 | 7.25 | 1.33 |
| **N** | 6.23 | 4.67 | 1.33 |
| **R** | 7.32 | 5.43 | 1.34 |
| **RA** | 7.07 | 3.83 | 1.84 |

Figure 4.32 shows the plot of Co content against the corresponding Ti content at points one to four. A linear inverse relationship between the Co and Ti contents of the alloys moving from the CFL into the bulk of the materials just below the CFL was shown to exist. The linear inverse relationship holds for a depth just below the CFL, and becomes non-linear moving into the bulk in both the recycled and un-recycled alloys, as shown by the non-linear sections of the plots in Figure 4.32. The plots for alloy NS, N and R are almost parallel, implying a similar relationship between the Co and Ti contents. The plot for RA, however, shows a steeper gradient.

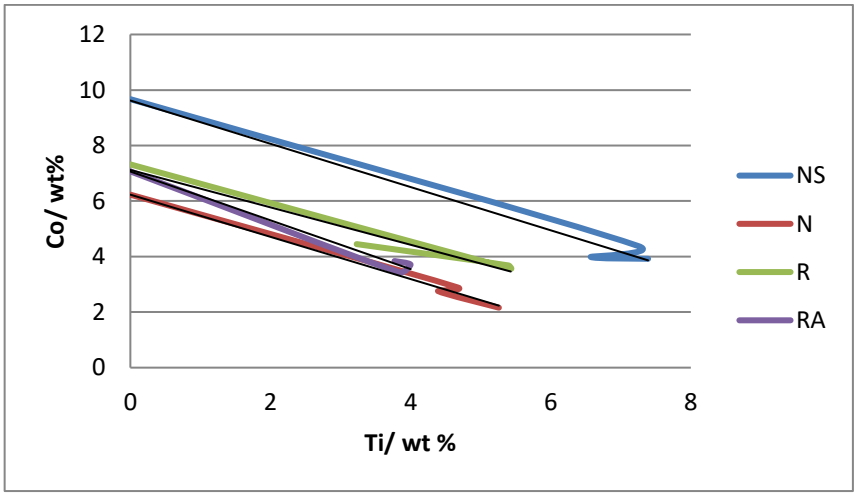



**Figure 4.32** Plot of Co and Ti contents from the CFL (origin) into the bulk (right), showing an inverse linear relationship between the Co and Ti contents moving from the CFL to just below the CFL.

Figures 4.27 – 4.30 also include the PIXE distribution maps of impurity elements Fe, Cr, Mn, Ni, and S in all alloys, and Zn as an additional impurity in the recycled alloys R and RA. The elements Fe and Cr were concentrated in the CFL, while the other impurities were evenly distributed throughout the samples in all alloys. The elements Ni and Mn were also concentrated in the CFL in alloy N only. In alloy N, S was concentrated in one specific position, and all the other impurities were not present in that specific position. Table 4.15 shows the chemical composition of the alloys obtained by PIXE. The major elements W, Co, Ti, Ta and Nb generally fell within the same concentration ranges. The concentration of W ranged from 68.30 – 74.75 wt %, while Co ranged from 5.33 – 6.30 wt %. The concentrations of Ti, Ta and Nb ranged from 4.49 – 4.74 wt %, 2 – 2.29 wt % and 0.03- 0.17 wt % respectively. PIXE identified S, Cr and Fe as the major impurities in all alloys. The element Zn was also detected as an additional impurity in the recycled alloys R and RA. The elements Ni and Mn were detected as trace impurities in all alloys, and Ca was detected as an additional trace impurity in alloys NS and RA.

**Table 4.15** Micro-PIXE elemental composition of sintered alloys.

| **Element/ wt%** | **NS** | **N** | **R** | **RA** |
|---|---|---|---|---|
| **$W_L$** | 71.33 | 74.72 | 68.30 | 70.79 |
| **Co** | 6.30 | 5.33 | 5.81 | 6.31 |
| **Ti** | 4.74 | 4.60 | 4.52 | 4.49 |
| **$Ta_L$** | 2.29 | 2.16 | 2.18 | 2.00 |
| **Nb** | 0.17 | 0.06 | 0.04 | 0.03 |
| **S** | 0.66 | 0.72 | 0.65 | 0.65 |
| **Cr** | 0.129 | 0.025 | 0.102 | 0.023 |
| **Fe** | 449 ppm | 670 ppm | 325 ppm | 522 ppm |
| **Ni** | ≤ 373 ppm | ≤ 446 | ≤ 341 ppm | ≤ 325 |
| **Mn** | ≤ 33 ppm | ≤ 32 | ≤ 25 | ≤ 34 |
| **Ca** | 89 ppm | - | - | ≤ 93 |
| **Zn** | - | - | 0.1229 | 0.1080 |

### 4.5.2 Physical properties

This section presents the results obtained from the physical and magnetic property characterization tests. Density was determined based on Archimedes' Principle, percentage shrinkage was determined according to the ASTM B610-08 [70] standard, and the volume open porosity was determined based on the ASTM 373-88 [72] standard. The magnetic saturation and coercivity were also measured accordingly.

Table 4.16 summarizes the physical properties of the sintered alloys. Table D1 in appendix D shows the dimensions of the samples before and after sintering. The percentage shrinkage ranged from 20.64 – 22.57 %, and virgin alloy NS had the highest percentage shrinkage (22.57 %), while the percentage shrinkage for N, R densities of the five samples per alloy. The recycled alloy R had a density of 13.64 g/cm$^3$, while the other alloys had a density of about 13.55 g/cm$^3$. While the percentage open porosity in all alloys was generally low, recycled alloy RA had the highest volume percentage of open porosity (0.49), while recycled alloy R had the lowest percentage of open porosity (0.31). Alloys NS and RA, which had higher shrinkage (22.57 and 21.48 % respectively), also had higher open porosity (0.42 and 0.49 respectively), compared to alloys N and R.

Table 4.16 also shows the magnetic properties of the sintered alloys. The theoretical magnetic saturation for each alloy was calculated based on equation 3.4 [58]. The actual magnetic saturation values for the alloys, which ranged from 9.62 – 11.39 μTm$^3$kg$^{-1}$, were lower than the theoretical magnetic saturation values, which were expected to range from about 12.0 – 15.0 μTm$^3$kg$^{-1}$. This indicated that some W dissolved in Co solid solution [58]. The average magnetic saturation value of the recycled alloy RA was about 73 % of the theoretical value (15.09 μTm$^3$kg$^{-1}$) [56], indicating that larger amounts of W were dissolved in Co

solid solution compared to the other alloys. The average magnetic saturation for alloys NS, N and R were about 82 % of the theoretical values. The recycled alloy R had a lower coercivity compared to the other alloys, which was expected because it had a lower Co content than the other alloys [56]. Alloys NS, N and RA had coercivity values within the same range, but the standard deviation for RA was significant, indicating variations in the measured coercivity values.

**Table 4.16** Physical properties of sintered alloys.

| **Alloy** | **NS** | **N** | **R** | **RA** |
|---|---|---|---|---|
| **% shrinkage** | 22.57 ± 0.83 | 20.64 ± 1.01 | 20.91 ± 0.62 | 21.48 ± 1.50 |
| **Density/ gmc$^{-3}$** | 13.56 ± 0.02 | 13.51 ± 0.06 | 13.64 ± 0.05 | 13.55 ± 0.04 |
| **Volume % open porosity** | 0.42 ± 0.06 | 0.35 ± 0.08 | 0.31 ± 0.08 | 0.49 ± 0.14 |
| **Coercivity/ kAm$^{-1}$** | 13.69 ± 0.03 | 13.85 ± 0.09 | 12.49 ± 0.09 | 13.71 ± 0.42 |
| **Magnetic Saturation/ μTm$^3$ kg$^{-1}$** | 11.39 ± 0.22 | 11.13 ± 0.20 | 9.62 ± 0.14 | 10.38 ± 0.35 |

### 4.5.3 Mechanical properties

This section presents the mechanical properties determined from hardness, fracture toughness and wear tests. Table 4.17 summarizes the hardness and fracture toughness values for all the alloys. The un-recycled alloys NS and N and recycled alloy R had average Vickers hardness values of about 1600 $HV_{30}$, while RA had an average Vickers hardness value of 1564 $HV_{30}$. A similar trend was observed using the Rockwell test, as indicated in Table 4.17. The fracture

toughness values ranged from 9.49 – 9.85 MPa.m$^{1/2}$, with the recycled alloy RA having the lowest fracture toughness value.

**Table 4.17** Hardness and fracture toughness values for the sintered alloys.

| **Alloy** | **Vickers Hardness ($HV_{30}$)** | **Rockwell A/ HRA** | **Fracture toughness/ MPa.m$^{1/2}$** |
|---|---|---|---|
| **NS** | 1601 ± 34 | 91.16 ± 0.05 | 9.68 ± 0.22 |
| **N** | 1606 ± 31 | 91.66 ± 0.05 | 9.85 ± 0.36 |
| **R** | 1608 ± 29 | 91.16 ± 0.05 | 9.55 ± 0.13 |
| **RA** | 1564 ± 20 | 90.66 ± 0.05 | 9.49 ± 0.19 |

The cumulative mass loss from the slurry abrasion tests is shown in Figure 4.33, and the raw data on mass loss is given in Appendix F. All the alloys had an average mass loss of about 3 mg in the first 30 minutes of the test, beyond which the average cumulative mass loss for alloy RA increased compared to the other alloys. Alloys NS, N and R continued to have similar average cumulative mass until after 120 minutes, when the cumulative mass loss for recycled alloy R increased compared to the mass loss for the un-recycled alloys NS and N. At the end of the test, alloy RA had the highest average cumulative mass loss (about 44 mg) while alloys NS, N and R had average cumulative mass loss between 35 and 40 mg. The cumulative mass loss for alloy RA was expected to be higher compared to the other alloys because alloy RA had lowest hardness and a highest binder content [51, 63, 64] compared to alloys NS, N and R.

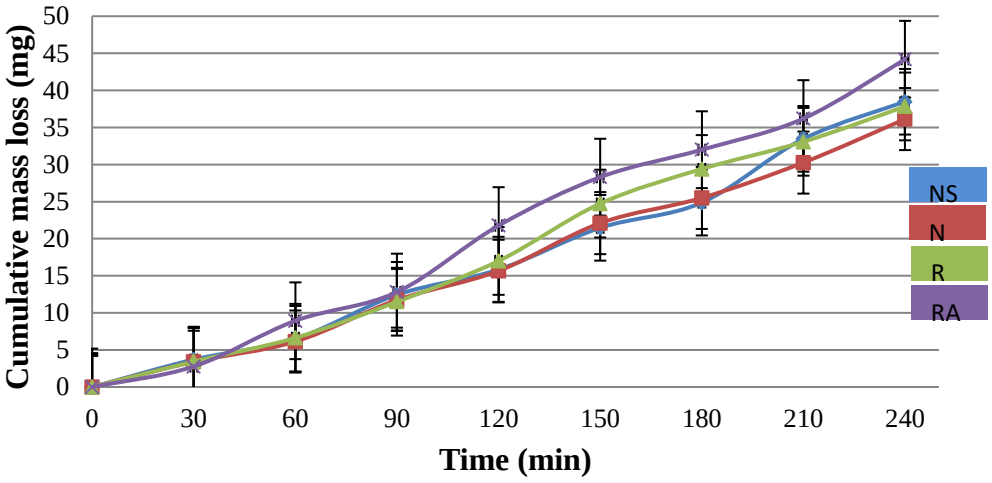



**Figure 4.33** Cumulative mass loss during slurry abrasion test.

Figure 4.34 shows the variation of the wear rate throughout the tests for the four alloys. The wear rate rose to about 0.125 mg/min for alloys NS, N and R in the first 30 minutes of the test, and dropped to about 0.1 mg/min from 30 to 60 minutes of the test. For alloy RA, the wear rate continued to rise to about 0.15 mg/min in the first 60 minutes of the test, and dropped to about 0.125 mg/min between 60 and 90 minutes of the test. After the first 30 minutes of the test, the wear rate for the un-recycled alloys NS and N, stayed in the range of about 0.125-0.15 mg/min. The wear rate of alloy R rose to just above 0.15 mg/min after 120 minutes at stayed almost constant, while the wear rate of alloy RA rose to 0.175-0.2 mg after 90 minutes at stayed within that range for the remaining part of the test.

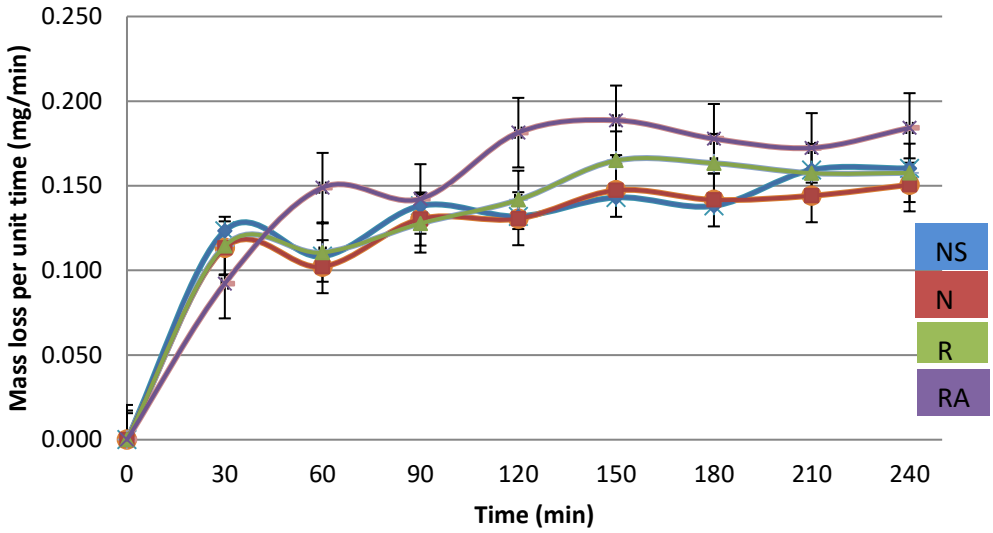



**Figure 4.34** Variation of wear rate during slurry abrasion test.

Figure 4.35 shows the average wear rate of the alloys. Alloy RA had the highest average wear rate (about 0.18 mg/min), which was expected because alloy RA had the lowest hardness (1564 $HV_{30}$) and the highest binder content (7.47 wt %) [51, 63, 64]. Alloys NS, N and R had an average wear rate of about 0.15 mg/min, although alloy R was expected to have the lowest wear rate because the alloy had the lowest binder content (5.84 wt %).

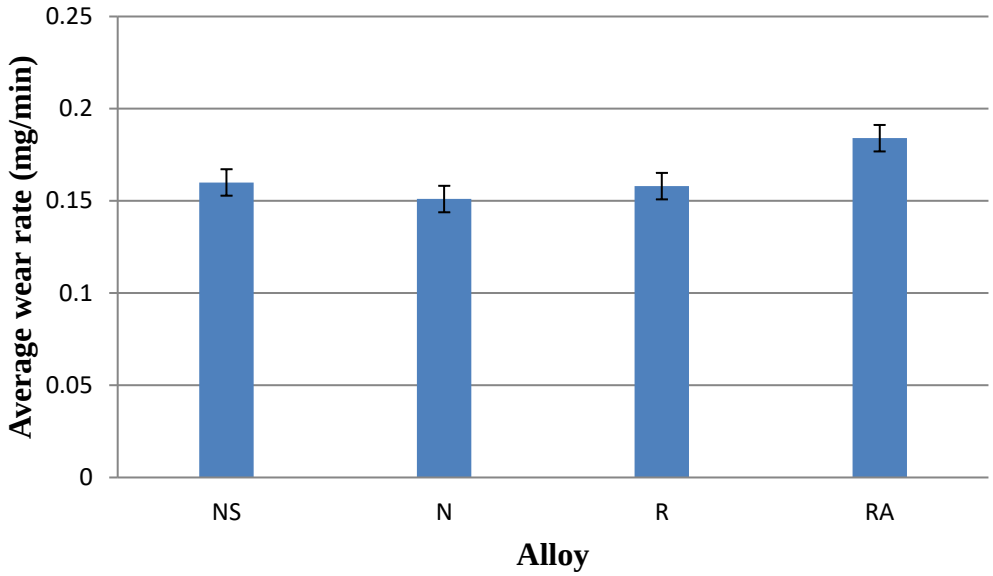



**Figure 4.35** Average wear rates of the alloys.

Figures 4.36 – 4.40 show FESEM micrographs of the worn surfaces of the un-recycled and recycled alloys respectively after the slurry abrasion tests. Binder phase removal was one of the major wear mechanisms observed, and there was pronounced damage on the carbide grains, as well as carbide grain pull-out in all the alloys. Single grain micro-cracks were observed on the large carbide grains, and micro-polishing of the large carbide grains was apparent in all grades. Small carbide fragments were also observed in alloys NS, N and RA. The cross-sectional view of the worn surfaces is shown in Figure 4.41, in which the micrographs further confirmed binder removal and grain pull-out as the major wear mechanisms during the slurry abrasion tests.

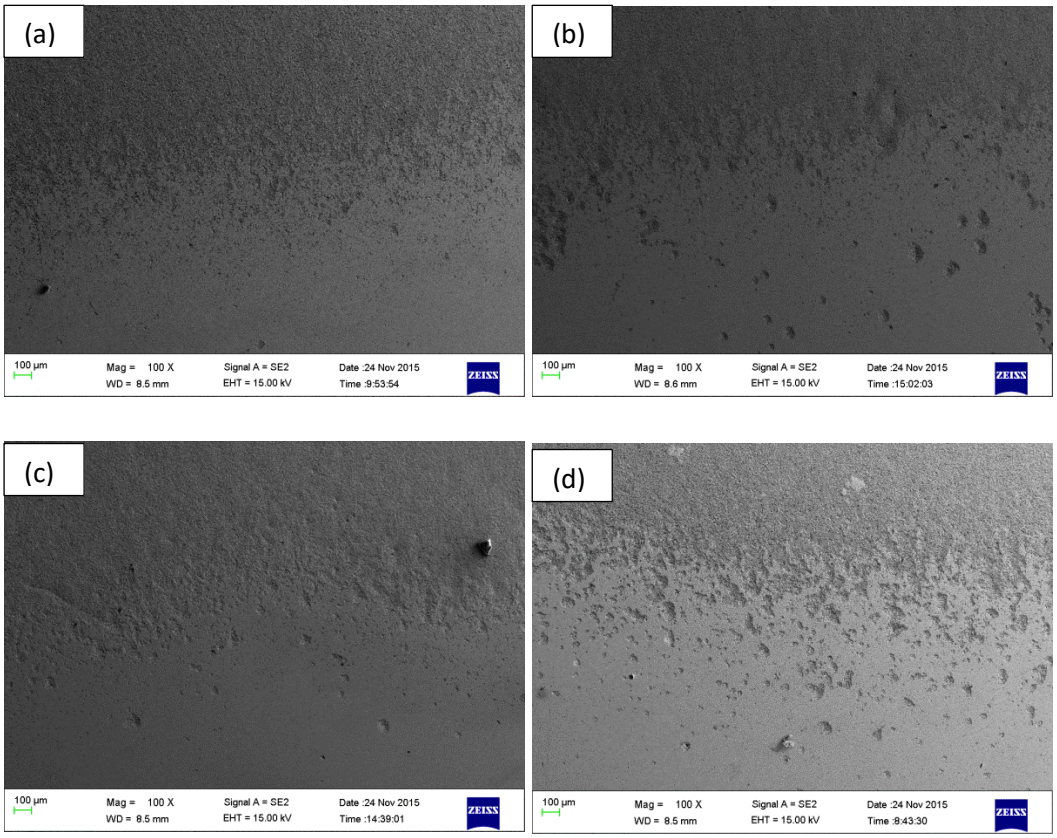



**Figure 4.36** FESEM images of wear scars of unrecycled alloys (a) NS and (b) N, and recycled alloys (c) R and (d) RA (100x) after slurry abrasion test. Alloys N and RA show more wear compared to NS and R.

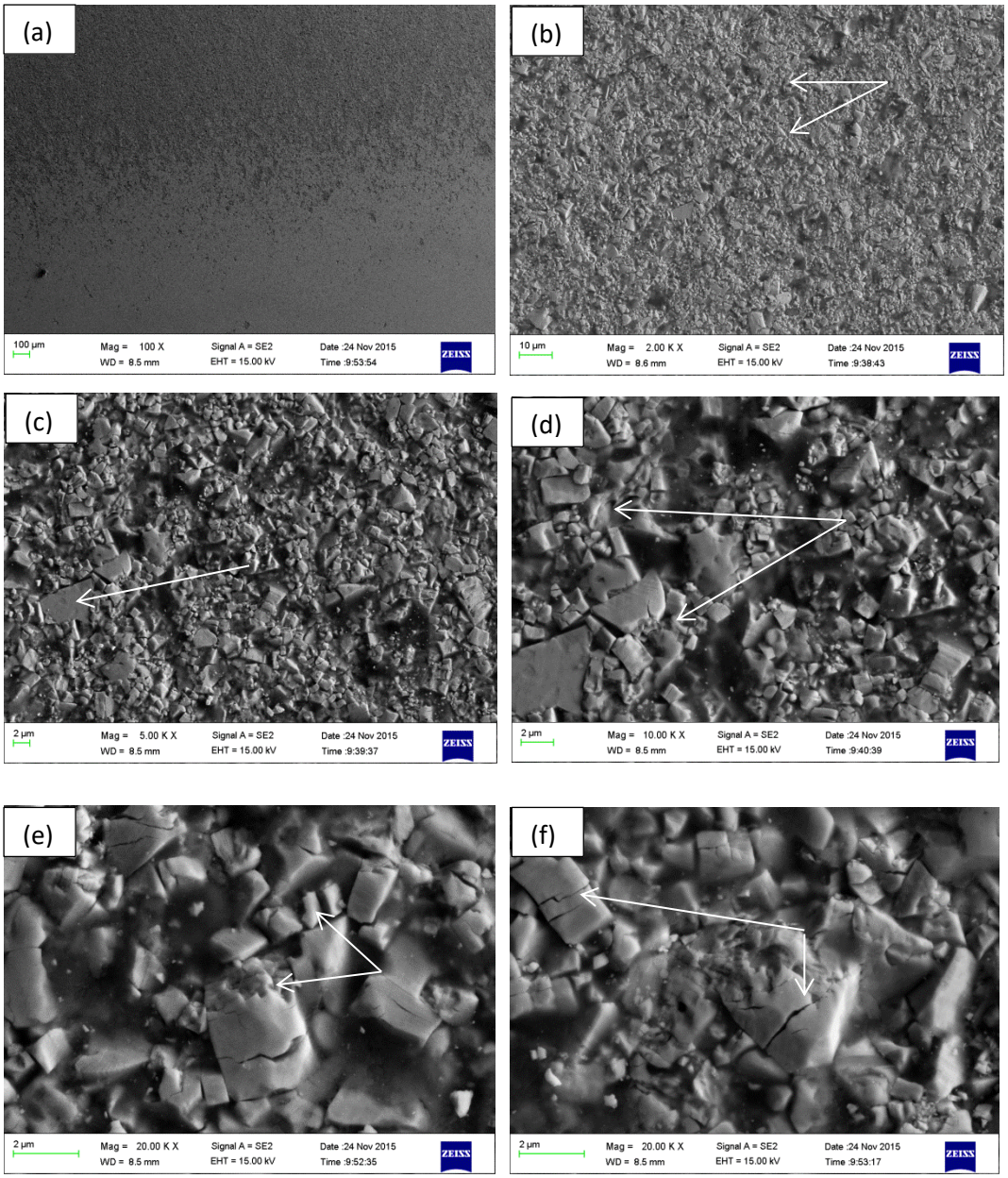



**Figure 4.37** FESEM images of wear scars after slurry abrasion test of un-recycled alloy NS showing (a) general loss of surface material (100x), (b) small groves from ductile binder displacement (2000x), (c) micro-polishing of large WC grains (5000x), (d) WC grain pull-out (10000x) (e) carbide grain disintegration (20000x), and (f) micro-cracking of WC grains (20000x).

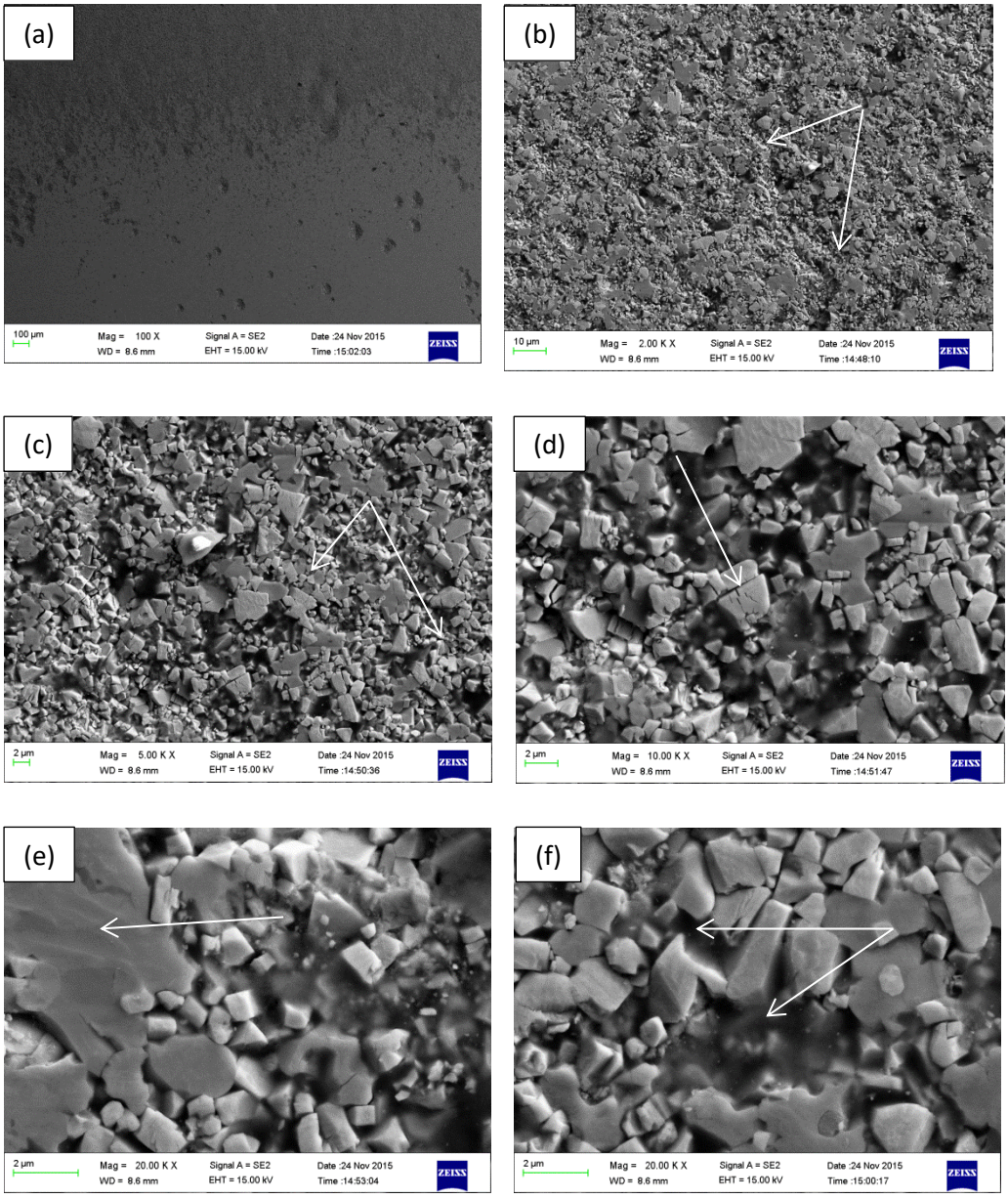



**Figure 4.38** FESEM wear scars after slurry abrasion test of un-recycled alloy N showing (a) general loss of surface material (100x), (b) pits as a result of grain pull-out (2000x), (c) carbide grain disintegration (5000x), (d) micro-cracking of carbide grains (10000x) (e) micro-polishing of carbide grains (20000x), and (f) carbide grain pull-out (20000x).

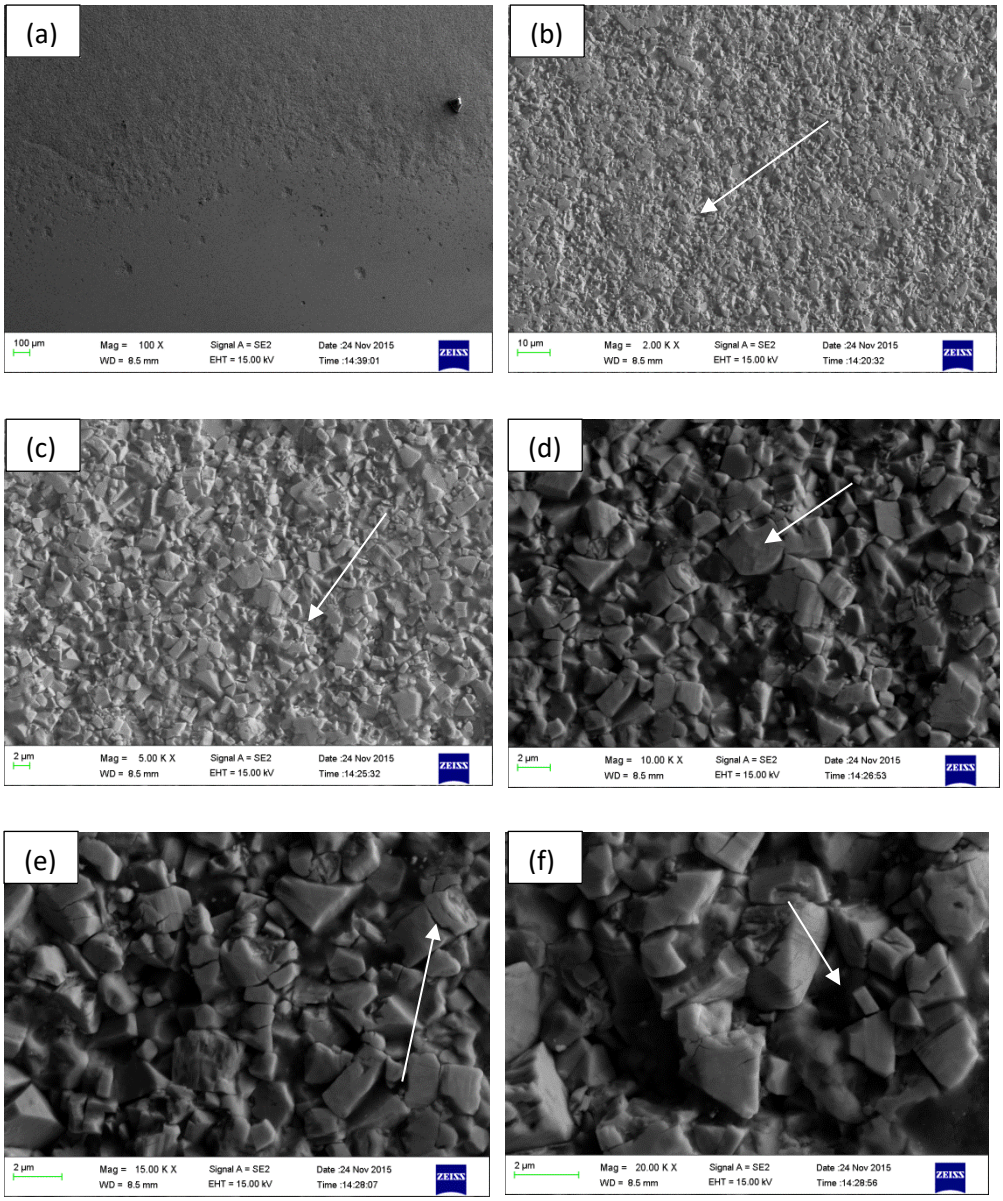



**Figure 4.39** FESEM images of wear scars after slurry abrasion test of recycled alloy R showing (a) general loss of surface material (100x), (b) small grooves from ductile binder displacement (2000x), (c) small pits from material displacement (5000x), (d) micro-polishing of carbide grains (10000x), (e) micro-cracking of carbide grains (15000x), and (f) carbide grain pull-out (20000x).

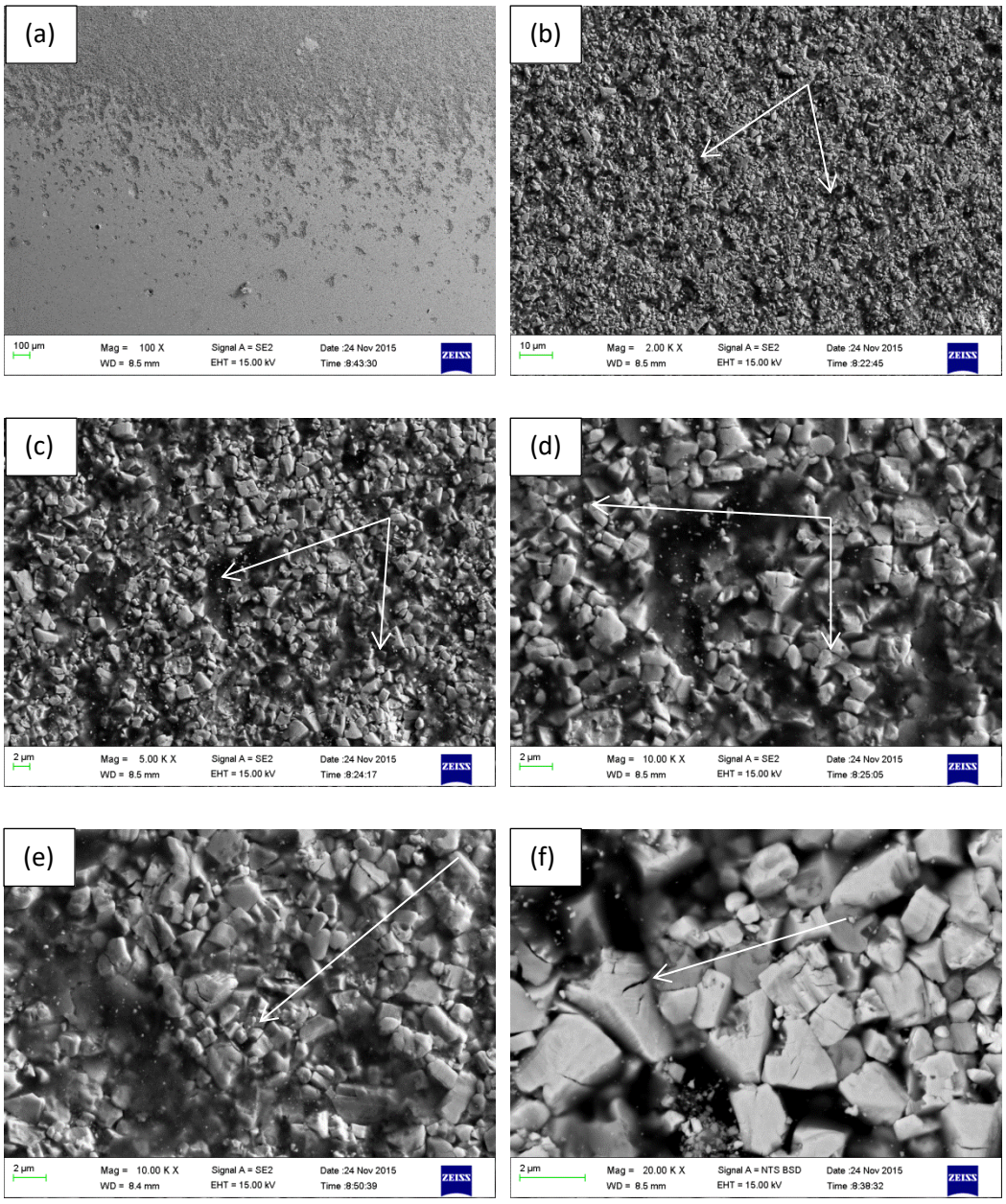



**Figure 4.40** FESEM images of wear scars after slurry abrasion test of recycled alloy RA showing (a) general loss of surface material (100x), (b) pits from material displacement (2000x), (c) carbide grain pull-out (5000x), (d) and (e) carbide grain disintegration (10000x), (e) and (f) micro-cracking of carbide grains (20000x).

.

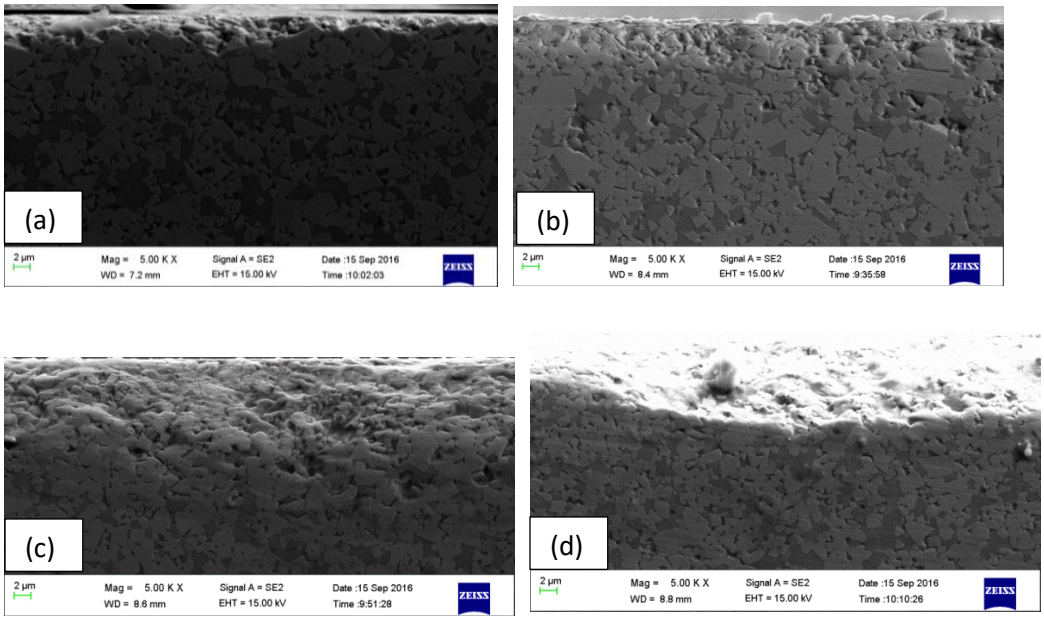



**Figure 4.41** FESEM micrographs of the cross sections of the worn surfaces after slurry abrasion of (a) NS, (b) N, (c) R and (d) RA. The micrographs show grain pull-out and binder removal during slurry abrasion.

Table 4.18 shows an EDS analysis comparison of the sample surfaces before and after slurry abrasion for all the alloys. The reduction in W, C, Co and Ti contents detected in all the alloys after slurry abrasion is further evidence that binder phase removal and carbide grain pull-out were the dominant wear mechanisms in all alloys. The amount of Ta detected after slurry abrasion increased, which can be evidence of exposure of new surfaces because of abrasive wear. The O content increased significantly after abrasive wear, and EDS also confirms the presence of Si and Al on the sample surfaces after abrasive wear. This is because of residual silica ($SiO_2$) and alumina ($Al_20_3$) that came from the sand used for slurry abrasion. The significant increase in O content also affected the quantities of the other elements after abrasive wear.

**Table 4.18** EDS analysis comparison on the surface of the alloys before and after slurry abrasion.

| Alloy / Element \ Wt % | NS | | N | | R | | RA | |
|---|---|---|---|---|---|---|---|---|
| | **Before** | **After** | **Before** | **After** | **Before** | **After** | **Before** | **After** |
| W | 77.32 | 56.18 | 77.84 | 57.02 | 80.76 | 61.74 | 79.83 | 57.13 |
| Co | 3.32 | 2.14 | 3.40 | 2.14 | 2.29 | 1.17 | 2.82 | 1.52 |
| Ti | 5.45 | 4.14 | 5.24 | 4.06 | 4.86 | 4.06 | 4.63 | 3.45 |
| Ta | 2.72 | 4.22 | 2.56 | 3.37 | 1.99 | 3.83 | 1.79 | 3.30 |
| Nb | 0.51 | 0.31 | 0.55 | 0.46 | 0.40 | 0.52 | 0.51 | 0.15 |
| C | 8.00 | 4.32 | 7.5 | 4.67 | 7.12 | 6.12 | 7.6 | 5.00 |
| O | 2.68 | 23.72 | 3.26 | 23.97 | 2.57 | 18.80 | 2.82 | 23.65 |
| Al | - | 2.27 | - | 2.28 | - | 1.38 | - | 3.57 |
| Si | - | 2.18 | - | 2.0 | - | 1.88 | - | 1.69 |

# 5 Discussion

## 5.1 Introduction

This chapter presents a general discussion of all the results obtained in this study. It discusses the products of the zinc recycling process, the properties of the un-recycled and zinc recycled powders and the sintered alloy properties.

## 5.2 Zinc recycling

A comparison between the microstructures of the inserts before and after zinc recycling revealed that the Co binder phase was not readily visible in the microstructure of the zinc recycled insert. This indicated effective binder disintegration in the inner layers of the inserts during the zinc recycling process, leaving loosely bound carbide particles. However, due to the nature of the zinc process, Co was deposited onto the already Co-rich surface CFL layers of the recycled inserts during zinc distillation. The high Co content made the surface layers tough, which explains why the recycled inserts maintained their general shape after zinc recycling.

The surface layers from the zinc recycled scrap inserts mainly formed the Co-rich oversize particles, which reduced the yield to 70%, instead of at least 97 %, as suggested by Upadhyaya [7]. The high Co content in the oversize particles made them softer and tougher, and therefore more difficult to crush and mill. Iron is known to occur in solid solution in the Co binder phase [60], which explains the higher wt% of Fe found in the oversize particles where the high Co content was found.

The second recycling session resulted in further concentration of Co in the surface layer of the resultant material, which agglomerated the carbide particles together, making it difficult to crush and mill. Yomaguchi and Okada [81], suggest that the friability of the zinc recycled cemented tungsten carbide is favoured by a lamella structure, which is difficult to obtain when the Co content of the scrap material is too high, or the grain size is too coarse. Hence the second recycling session could not easily disintegrate the material because the lamella structure was not readily formed due to high Co contents.

## 5.3 Powder Characterization

The recycled powders R and RA took twice as much time to mill to the desired particle size as the un-recycled powders NS and N. This can be attributed to the fact that the starting particle size for the recycled powders R and RA was larger (about 8μm), compared to the un-recycled powders NS and N, which had the WC starting particle size ranging between 4 and 5 μm. Significant particle size reduction in the un-recycled and recycled powders took place during the first two hours and four hours of milling respectively, and slowed down thereafter. Coarse carbides, above 2 μm, are usually polycrystalline, and have certain weak grain boundaries along which the grains fracture during the initial stages of milling [7]. This explains the rapid initial particle size reduction which was observed in the powders. As the particle size goes below 2 μm, particle size reduction is believed to be mainly due to attrition, which results in the formation of fines, and particle size reduction becomes much slower [7]. This explains the decreases in the rate of particle size reduction that was observed in all the powders.

Milling the recycled powders R and RA to 1.7-1.8 μm resulted in powders which had larger spans compared to the un-recycled powders NS and N, indicating a wider particle size distribution. After the initial significant particle size reduction

to about 3 μm, particle size reduction slowed down, and it took another 13 hours and 6 hours respectively for the recycled and un-recycled powders to be reduced from about 3μm to about 1.7 μm. It is during this period that particle size reduction was predominantly by attrition, resulting is the generation of fine particles. Hence more fine particles were produced in the recycled powders R and RA because of longer milling times, compared to the un-recycled powder N, explaining the wide particle size distribution in the recycled powders.

The powder produced from crushing the zinc recycled inserts had angular grains and a wide particle size distribution. This was due to the mechanical crushing process that the zinc recycled inserts were subjected to, which was largely by impact. After milling to 1.7 – 1.8 μm, the zinc recycled powders R and RA still had predominantly large angular grains. This is expected for zinc recycled powders as they are product of the disintegration of Co bound WC particles that are in the form of partially developed triangular prism with truncated edges [7]. Virgin powders are predominantly pseudomorphic aggregates of fine particles, especially when the milling starting particle size is small [7]. Therefore, milling the un-recycled powders NS and N largely separated the pseudomorphic aggregates, which explains the isolated large angular grains amongst the more rounded smaller particles which were found in the un-recycled powder.

After milling, small selected areas indicated better homogeneity in the recycled powders R and RA compared to the un-recycled powders NS and N, where Co and Ti pools were observed. Better homogeneity in the recycled powders can be attributed to repeated processing and longer milling times, which ensured the even distribution of all the elements.

The slight differences in weight percentages of the major elements between the milled recycled and un-recycled powders can be explained by the uneven

distribution of elements between the initial recycled powder and oversize particles after the first zinc recycling session. For instance, more Co reported to the oversize particles, resulting in Co content which was lower than the stoichiometric value in the recycled powder R. Sulphur and silicon were the major impurities detected in all the powders, and were thought to be introduced together with carbon black which was added to all the powders to compensate for C loss during sintering [60]. The C content of the recycled powder was also found to be lower than the stoichiometric value due to losses via oxidation during sintering of the inserts from which the recycled products were produced [7]. The XRD plots for the powders, shown in Figure 4.15, show the presence of FeO as an impurity phase in the recycled powders R and RA, which confirms the occurrence of oxidation reactions during sintering.

Some impurities such as Fe and Ni can be present in the cemented carbides in considerable amounts without negatively affecting the properties [53]. However, elements such as Ca, Na, P and O give rise to non-metallic inclusions and porosity [53], and the quantities of such elements should be kept in check. Milling of powders N, R and RA was done in tungsten carbide lined mills, which minimized contamination of the powders by impurity elements such as Fe, Ni and Cr. Therefore, the traces of Ca, Cr, Cu, Fe, Ni and V which were detected in all powders were most likely entrained in the starting raw materials [53] for new powders NS and N. These impurities also possibly found their way into the virgin powder NS during milling, which was done in commercial stainless steel mills, and were carried over to the recycled powders R and RA since the zinc recycling process does not have any purification effect [1]. More impurities were also possibly introduced in the recycled powders during the crushing process from the stainless steel hammer and vessel that were used. Traces of Zn from the zinc recycling process were also found in recycled powders R and RA.

The XRD analysis identified WC, TiC and Co as the major phases in all the powders. This was expected as W had the highest weight percentage, followed by Co and Ti, and their phases were easily detected by the XRD machine. The phases NbC and TaC were not detected, most likely because they were below the detection limits of the XRD machine. The only impurity phase detected in the recycled powders R and RA was FeO, confirming Fe build up due to repeated processing.

The green densities for both the recycled and un-recycled powders, shown in Table 4.10, ranged from 6.757 – 7.846 g/cm$^3$. This indicates a small difference in the green densities, even though un-recycled powder NS was the only spray dried powder. Therefore, the sieving method used to regulate the agglomerates in the powders N, R and RA produced powder agglomerates that were comparable in properties to the spray dried agglomerates in NS.

## 5.4 Sintered Alloy Characterization

German [27], and Qvick [82] suggest that the percentage shrinkage of sintered cemented carbides with fine to medium carbide grain sizes (~2µm) ranges from 16-20 %. The percentage shrinkage of both the recycled and un-recycled powders, shown in Table 4.16, ranged from 20.64 – 22.57 %. These values were within the ranges expected for this grade of materials, indicating good dimensional control during the sintering process [27]. The sintered density of the alloys, also shown in Table 4.16, ranged from 13.51 – 13.64 g/cm$^3$, and these values are within the expected range for the grade of material [13] (refer to Table 2.1). The recycled alloy R had a highest sintered density, and this can be explained by the fact that alloy R had a higher carbide volume fraction and lower Co content compared to alloys NS, N and RA, accounting for the higher density. The expected porosity in cemented tungsten carbides is about 0.2 % [7]. The porosity in the sintered alloys

ranged from 0.31 – 0.49 %, and was slightly higher than expected. However, the densities and percentage shrinkage for the sintered alloys were within the expected ranges for the grade of material, indicating high densification [27].

Generally, a low magnetic saturation value implies higher W solubility in Co due to a low C content, with the possible formation of eta phase [56]. Alloy R had a lower magnetic saturation (9.62 $\mu Tm^3kg^{-1}$) compared to the other materials, which was expected because the alloy had less Co in its starting formulation. Alloy RA, despite having the stoichiometric Co content, had a lower magnetic saturation than expected. Alloy RA had 73 % of the theoretical magnetic saturation (calculated from Equation 3.4), while alloys NS, N and R had about 82 % of the theoretical magnetic saturation. This was because alloy RA had a slightly higher W content than the other alloys, and about the same C content as in the other alloys in its starting formulation. Therefore, this resulted in excess W, which dissolved in Co, reducing the amount of ferromagnetic Co [58]. Despite the fact that the magnetic saturation for RA was about 73% of the theoretical value, which is very close to the range in which eta phase forms [56], no eta phase was observed in alloy RA. Coercivity generally increases with a decreasing binder mean free path and/or a fine grain size [56]. Alloys NS, N and RA had similar coercivities, shown in Table 4.16, which was expected because they had similar binder mean free paths and grain sizes. Alloy R had the lowest coercivity (12.49 $kAm^{-1}$) because it had the coarsest carbide grain size (2.07 µm) and less Co (5.84 wt %) in its starting formulation compared to the other alloys.

Literature [22-24] suggests that the formation of a functional gradient in TiCN containing tool grade cemented tungsten carbides depends on the diffusion direction of N, which is produced from the irreversible decomposition of TiCN. Sintering a TiCN containing cemented carbide in a vacuum promotes the outward diffusion of N because the pressure in the furnace atmosphere is lower than the equilibrium partial pressure of N. This N diffusion process is coupled by the

inward diffusion of Ti, Ta and Nb (high affinity for N) and the outward diffusion of Co (low affinity for N) [22]. In this study, sintering was done in a vacuum, and a cubic free layer (CFL) was formed in the microstructure of both the recycled and un-recycled alloys. The formation of a CFL in R and RA is evidence that TiCN, which decomposes to supply the N to drive the diffusion process, was still present in the scrap material from which the recycled alloys were produced, and was recovered during the zinc recycling process. The narrower CFL in recycled alloys R and RA shows that the TiCN recovered from the scrap materials is less than in the un-recycled powders because the width of the CFL is directly proportional to the nitrogen content in the starting formulation [24].

The microstructure of the un-recycled alloys NS and N showed large isolated carbide grains surrounded by much smaller grains, while the recycled alloys R and RA also had isolated large carbide grains, but the surrounding grains were much coarser compared to the ones in the un-recycled alloys. This carbide grain size distribution can be explained by the fact that the recycled powders R and RA had severely fragmented carbide particles due to longer milling times, which created more active surfaces for grain growth and possibly supported Ostwald ripening. This promoted faster growth kinetics during sintering, as suggested by Cherniavsky [48]. TaC and NbC are added to tool grade cemented carbides to control grain growth during sintering [14-17]. The recycled and unrecycled alloys had similar amounts of TaC and NbC in their composition, confirmed by the presence of Ta and Nb in EDS analysis (Table 4.11). The measured average carbide grain size for the alloys, shown in Table 4.13, ranged from 1.90 – 2.07 µm, which indicated that grain growth inhibition from TaC and NbC was effective in both the recycled and un-recycled alloys.

Carbide contiguity decreases as binder content increases [51, 52]. Alloy RA had the highest Co content (7.47 wt %), and the lowest carbide contiguity (0.46) Alloys NS, N and R had a contiguity of about 0.53, and had slightly lower Co

contents, shown in Table 4.11, compared to alloy RA. Binder mean free path increases with binder content and carbide grain size [7]. The binder mean free path of the alloys is shown in Table 4.13, and recycled alloy RA had the longest binder mean free path because the alloy had the highest Co content.

The PIXE elemental distribution maps of Co showed depletion just below the CFL, and was distributed in small Co pools elsewhere in the bulk of the material for all the alloys. The possible explanation for this observation is that diffusion of Co into the CFL from the regions just below the CFL occurred at a faster rate compared to the rate of Co diffusion from the regions deeper into the bulk towards the surface. Hence the Co near the surface diffused into the CFL, leaving an uneven Co distribution especially in alloys N, RA and R. The Ti, Ta and Nb PIXE distribution maps showed even distribution beneath the CFL into the bulk. This possibly shows that the diffusion of Co takes place in a mechanism different from Ti, Ta and Nb as suggested by Chen et al. [19]. In cemented carbides, Fe forms a solid solution with Co [60]. Therefore, PIXE and EDS detected Fe in higher amounts in the CFL, where Co was concentrated. The same impurity elements detected in the powders, as discussed in section 5.3, were found in the respective alloys.

There is a linear inverse relationship between the Co content in the CFL ($Co_1$) and the Ti immediately beneath the CFL ($Ti_2$) regardless of the composition of the material, provided there is enough Ti and nitrogen in the starting formulation [82]. Hence alloys NS, N and R had the same $Co_1/Ti_2$ ratio despite recycled alloy R having a lower Co content compared to the un-recycled alloys NS and N. Recycled alloy RA had stoichiometric adjustment of Co, which diluted the concentrations of other elements in the material. Therefore, the effect of nitrogen diffusion lost its strength faster in RA, resulting in less effective removal of the mixed crystal carbides from the CFL. In addition, Ti, Ta and Nb diffuse into the bulk due to their affinity for nitrogen, and the fast depletion of nitrogen in RA

implied that the driving force for the diffusion of the cubic carbide formers ceased to exist. This resulted in more Co reporting to the CFL as a result of nitrogen depletion in the CFL, than Ti that moved out of the CFL, resulting in a higher $Co_1$ and a lower $Ti_2$ values. This also explains the steeper gradient of Co-Ti plot for RA.

The major phases WC, TiC and Co were detected in the sintered alloys, and TaC and NbC, which were also part of the composition, were not detected possibly because they were below the detection limits of the XRD machine. Despite FeO being detected in the recycled powders R and RA, it was not detected in the sintered alloys possibly because it also fell below the detection limits of the XRD machine after sintering.

The hardness of cemented carbides decreases with increase in Co content and grain size [18, 32]. The Vickers and Rockwell hardness values for the sintered alloys, shown in Table 4.17, ranged from 1564 – 1608 $HV_{30}$ and 90.66 – 91.66 HRA respectively. As expected, recycled alloy RA had the lowest hardness value because it had the highest Co content. Alloys NS, N and R had similar hardness values, despite the fact that the recycled alloy R had the lowest Co content (5.84 wt %) and was expected to be significantly harder the un-recycled materials NS and N. This can be explained by the fact that the formation of a CFL concentrates the hard mixed crystal carbide phase in the bulk of the material [83]. Since recycled alloy R (and RA) had a narrower CFL compared to un-recycled alloys NS and N, the hard mixed crystal carbide phase was distributed over a larger area in the bulk of the recycled than the un-recycled alloys. Hence the hardness of recycled alloy R was similar to that of un-recycled alloys NS and N, which had a higher concentration of the mixed crystal carbide phase in the bulk, overshadowing the effect of a higher Co content.

Fracture toughness increases with increasing binder content, carbide grain size and binder mean free path [7]. Therefore, the fracture toughness of the recycled alloy RA was expected to have the highest value because the alloy had the highest Co content. Table 4.17 shows that recycled alloy RA had the lowest fracture toughness (9.49 $MPa.m^{1/2}$), even though the value was close to the fracture toughness values for the other alloys, and was within the range of expected fracture toughness values for the grade materials [13]. Based on the discussion on magnetic saturation, the C content in recycled alloy RA was lower than the stoichiometric value, and the amount of C affects the binder phase fluidity, such that excess carbon increases binder phase fluidity, which improves binder phase distribution [84]. Since alloy RA had a low C content, the binder phase distribution was negatively affected, which compromised the fracture toughness of alloy RA. Although the eta phase was not detected in alloy RA, the possibility of it forming during sintering was there, due to low C content, and may also explain why the fracture toughness was lower than expected. Alloy R had a lower Co content than the other alloys, and as expected, had lower fracture toughness compared to the un-recycled alloys NS and N.

Abrasive wear resistance increases with a decrease in binder content and carbide grain size, and increases with increase in hardness [51, 63, 64]. The average wear rate for the recycled alloy R was expected to be lower than the other alloys because of the lower binder content. Instead, it was within the same range as the un-recycled alloys NS and N. This can be explained in terms of the higher concentration of the cubic carbide phase in the bulk of the un-recycled alloys NS and N, which made them harder and more difficult to wear. The average wear rate for recycled alloy RA, which had a higher Co content, was higher than for the other alloys, which was expected since binder phase removal takes place quite early under most wear conditions [85].

Soft abrasion was experienced by all the alloys because the ratio of the hardness of the silica sand to the hardness of the alloys was less than 1.2 [61]. Preferential removal of the binder phase was believed to be the most likely major wear mechanism in the early stages of the experiment. In hardmetals, significant mass loss is believed to be a result of carbide removal from the material compared to binder removal [64]. Continued removal of the binder phase compromises the strength of the remaining carbide phase, and results in the build-up of plastic strain in the individual carbide grains. This often results in fracture and fragmentation of the carbide grains [86, 87]. Cracks can also develop within the carbide skeleton, resulting in the weakening of the structure and the possibility of individual carbide grains breaking away. This was consistent with the observations that were made on the wear scars on all the grades. Carbide grain pull-out may have accounted for the bulk of the mass loss that occurred in all the alloys.

Small fragments may remain within the structure of the carbide by either re-imbedding in the structure as further contact occurs, or attaching to the binder phase that is extruded through the cracks in the carbide skeleton [88]. The re-embedding is thought to reinforce surface layers of the carbide, a process believed to be ‘self-healing’, which increases the wear resistance of the layers and reduces the wear rate, particularly in hardmetals that have high binder content [77]. This explains why the wear rate of the un-recycled alloys NS and N, which had a higher Co content than alloy R, slowed down earlier. The small carbide grains likely re-imbedded into the pits left by the removed binder, as binder extrusion was not readily observed in all the alloys.

# 6 Conclusions

## 6.1 Zinc recycling

The recycled inserts did not form a ‘cake’ after zinc recycling as expected. Instead the recycled inserts showed a marked increase in volume and maintained their general shape. The recycled inserts yielded about 70 % recycled powder and 30% coarse oversize particles, which turned out to be predominantly fragments from the surface layers of the tool grade scrap inserts. The oversize particles had Co content higher than the scrap material and the recycled powder. This made it difficult to disintegrate them either by milling because they were tough, or by subjecting them to a second recycling session because the high Co content interfered with lamellar formation, which makes the material friable and easy to disintegrate. In the as recovered state, the recycled powder predominantly had angular grains which had a wide particle size distribution. The powder average particle size was 8 μm, which was about double the initial average particle size of the virgin powder. The recycled powder also had lower Co and C contents than desired.

## 6.2 Comparison of recycled and unrecycled powders

It took the recycled powders twice as much time as the un-recycled powders to mill down to 1.7 – 1.8 μm, due to a larger starting particle size. Due to longer milling times, the elemental distribution indicated better homogeneity of elements in the recycled powders compared to the new powder. After milling, the particles in the recycled powders remained predominantly angular, while the new un-recycled powders had smaller more rounded particles. The recycled powders picked up traces of zinc from the zinc recycling process, and had slightly higher

quantities of Fe and Cr compared to the new un-recycled powders. Both the recycled and un-recycled powders had S contents that were within the same range.

## 6.3 Characterization of sintered alloys

A functional gradient was formed during sintering, resulting in the formation of a cubic free layer [CFL] in all the alloys, although this CFL was narrower in the recycled alloys R and RA. The recycled alloy R had a slightly higher density, due to a lower binder volume fraction. The volume percent porosity was generally within the same range, indicating a similar amount of densification in all the alloys.

The recycled alloy R and the un-recycled alloys NS and N had hardness, wear resistance, contiguity and binder mean free path that were within the same range. RA had slightly different properties due to a higher Co volume fraction. Recycled alloy RA had a much lower magnetic saturation compared to R, NS and N, attributed to the low C content that the powder had before sintering.

# 7 Recommendations

Based on the conclusions drawn, the following recommendations for future work are presented:

- The tool grade scrap material should be immersed in the zinc melt for a longer period to ensure complete disintegration of the binder material bonds.
- Chemical recycling methods should be explored, for comparison with the zinc recycling process.
- The recycled powder should be mixed with new un-recycled powder to get a stoichiometric balance of all desired elements, and also to dilute effects of impurities and trace elements.
- Machining tests should be carried out as they are the most appropriate to properly evaluate the wear properties of the recycled alloys.

## References


1. K.J.A. Brookes. Reclaimed tungsten powders with virgin properties. Met Powder Report (1990); Feb: 131-2.

2. U.S Geological Survey. Mineral Commodity Summaries (2016).

3. T. Ishida, T. Itakura, H. Morguchi and A. Ikagaya. Development of technologies for recycling cemented carbide scrap and reducing tungsten use in cemented carbide tools. SEI Tech Rev (2012): 75.

4. S. Gurmen and B. Friedrich. Recovery of cobalt powder and tungsten carbide from cemented carbide scrap – Part 1: Kinetics of Cobalt Leaching. Insabul Technical University Turkey, IME Process Metallurgy and Metal Recycling, German. Erzmetall ,57, (2004) 113-17.

5. C.S. Freemantle, N. Sacks, M. Topic and C.A. Pineda-Vargas. PIXE characterization technique in the cutting tool industry. Nuclear Instruments and Methods in Physics Research, B318, (2014) 168 – 172.

6. C.S. Freemantle, N. Sacks, M. Topic and C.A. Pineda-Vargas. Impurity characterization of zinc-recycled WC-6 wt% Co cemented carbides. International Journal of Refractory Metals and Hard Materials, 44, (2014) 94 -102.

7. G.S. Upadhyaya. Cemented Tungsten Carbides: Production, Properties and Testing. New Jersey: Noyes Publications, (1995).

8. H. Engqvist, G.A. Botton, S. Ederyd, M. Phanuel, J. Fondelius, and N. Axên. Wear phenomena on WC-based face seal rings. International Journal of Refractory Metals and Hard Materials, 18, (2000) 39 – 46.

9. R. Edwards. Cutting Tools. Institute of Materials, (1993), 200.

10. S.Z.D. Luyckx. Nucleation and propagation of fracture in WC-Co alloys. PhD Thesis. (1967). University of the Witwatersrand, Johannesburg.

11. E. Lassner and W.D. Schubert. Tungsten. New York: Plenum Press, (1999), pp 321.

12. C. Barbatti, J. Garcia, P. Brito and A.R. Pyzall. Influence of WC replacement by Ti and (Ta, Nb)C on oxidation resistance of Co-based cemented carbides. International Journal of Refractory Metals and Hard Materials, 27, (2009) 768 – 776.

13. G.S. Upadhyaya. Material science of cemented carbides – an overview. Materials and Design, 22, (2001) 483 - 489.

14. J. Weidow, J. Zackrisson, B. Jansson and H. Andren. Characterization of WC-Co with cubic carbide additions. International Journal of Refractory Metals and Hard Materials, 27, (2009) 244 - 248.

15. K.H. Lee, S.I. Cha, B.K. Kim and S.H. Hong. Effect of WC/TiC grain size ratio on microstructure and mechanical properties of WC-TiC-Co cemented carbides. International Journal of Refractory Metals and Hard Materials, 24, (2006) 109- 114.

16. S.G. Huang, R.L. Liu, L. Li, O. Van der Biest, and J. Vleugels. NbC as a grain growth inhibitor and carbide in WC-Co hardmetals. International Journal of Refractory Metals and Hard Materials, 26, (2008) 389- 395.

17. C.W. Morton, D.J. Wills and K. Stjernberg. The temperature ranges for maximum effectiveness of grain growth inhibitors in WC-Co alloys. International Journal of Refractory Metals and Hard Materials, 23, (2005) 287- 293.

18. Z. Zak Fang, X. Wang, T. Ryu, K.S. Hwang and H.Y. Sohn. Synthesis, sintering, and mechanical properties of nanocrystalline cemented tungsten carbide – A review. International Journal of Refractory Metals and Hard Materials, 27, (2009) 288-299.

19. L. Chen, W. Lengauer and K. Dreyer. Advances in modern nitrogen-containing hardmetals and cermets. International Journal of Refractory Metals and Hard Materials, 18, (2000) 153- 161.

20. R. Frykholm and H.O. Andren. Development of the microstructure during gradient sintering of a cemented carbide. Materials Chemistry and Physics, 67, (2001) 203- 208.

21. L. Chen, W. Lengauer, P. Ettmayer, K. Dreyer, H.W. Daud and D. Kassel. Fundamentals of liquid phase sintering for modern cermets and functionally graded cemented carbonitrides (FGCC). International Journal of Refractory Metals and Hard Materials, 18, (2000) 307- 322.

22. M. Mohammadpour, P. Abachi and K. Pourazarang. Effect of cobalt replacement by nickel on functionally graded cemented carbonitrides. International Journal of Refractory Metals and Hard Materials, 30, (2012) 42-47.

23. R. Frykholm, M. Ekroth, B. Jansson, H.O. Andren and J. Agren. Effect of cubic phase composition on gradient zone formation in cemented carbides. International Journal of Refractory Metals and Hard Materials, 19, (2001) 527- 538.

24. W. Lengauer and K. Dreyer. Functionally graded hardmetals. Journal of Alloys and Compounds, 338, (2002) 194 – 212.

25. S.W.H. Yih and C.T. Wang. Tungsten: Sources, Metallurgy, Properties, and Applications. New York: Plenum Press, 1979.

26. K.J.A. Brookes, Cemented carbides for Engineers and Tool Users, International Carbide Data, UK (1983).

27. R. M. German, Liquid Phase Sintering, Plenum Press, New York, p. 65 (1985).

28. W. D. Kingery, Densification during sintering in the presence of a liquid phase 1: Theory. Journal of Applied Physics, 30, (1959) 301.

29. W. D. Kingery, E. Niki, and M.D. Narasimhan. Sintering of oxide and carbide-metal compositions in the presence of a liquid phase. Journal of American Ceramic Society, 44, (1961) 29.

30. R.J. Nelson and D.R. Milner. Powder Metallurgy, 15, (1972) 346-363.

31. P.G. Barnard, A.G. Starliper and H. Kenworthy. Reclamation of refractory carbides from carbide materials. US Patent 3595484. 1971.

32. E.M Trent. Process of separating hard constituents from sintered hard metals. US Patent 2407752. 1946.

33. E. Lassner and W.D. Schubert. Tungsten. New York: Plenum Press, 1999, pp 321.

34. ASM International Handbook. Powder Metal Technologies and Applications. Volume 7, 1999.

35. A.G. Hartline, J.A. Campbell and T.T. Magel. Process for reclaiming cemented metal carbide. US Patent 3953194. 1976.

36. M.G Faga, R. Mattioda, L. Settineri. Microstructural and mechanical characteristics of recycled hard metals for cutting tools. CIRP Annals – manufacturing Technology, (2010) 133 -136.

37. J. Lee, E. Kim, J. Kim, W. Kim, B, Kim and B. D. Pandey. Recycling of WC-Co hardmetal sludge by a new hydrometallurgical route. International Journal of Refractory Metals and Hard Materials, 29, (2011) 365 – 371.

38. W.G. Jung. Recovery of tungsten carbide from hard material sludge oxidation and carbothermal reduction process. Journal of Industrial and Engineering Chemistry, 20, (2014) 2384 - 2388.

39. H.E. Exner. Physical and chemical nature of cemented carbides. International Metals Review, 24, (1979) 149-173.

40. H. Schulze-Schreiber, P. Ettmayer, M. Schreiner and B. Lux. International Powder Metallurgy conference, Florence, (1982).

41. N.K. Sharma, I.D. Ward, H.L. Fraser and W.S. Williams. Journal of American Ceramic Society, 63, (1980) 194-196.

42. E. Lardner and D.J. Bettle. Isostatic hot pressing of cemented carbides. International Journal of Refractory Metals and Hard Materials, 7, (1973) 540-545.

43. S. Amberg and H. Doxner. Porosity in cemented carbides. Powder Metallurgy, 20, (1979) 1.

44. H.E. Exner, J. Freytag, G. Petzow and P. Walter. Planseeber Pulvermet, 26, (1978) 90.

45. M. Hellsing, A. Henjered, H. Norden, and H.O. Andren. Science of Hard Materals, (R. K. Viswanadham, D. J. Rowcliffe, and J. Gurland, eds.), Plenum Prss, New York, p. 93 (1983).

46. T. Johansson, B. Uhrenius. Phase equilibria, isothermal reactions, and a thermodynamic study in the Co-W-C system at 1150 $^{o}$C. Metal Science, 12, (1978) 83-94.

47. J. Freytag, and H.E. Exner. Influence of tungsten and carbon additions on the sintering and magnetic properties of WC-12Co cemented carbides. Modern Developments in Powder Metallurgy, MPIF, Princeton, 10, (1977) 511.

48. K.S. Cherniavsky, Proceedings of Powder Metallurgy Conference, France, 1 (1994).

49. E. Lardner. The control of grain size in the manufacture of sintered hard-metal. Powder Metallurgy, 13, (1970) 394-428.

50. J.W. Lee, D. Jaffery, and J.D. Browne. Influence of process variables on sintering of WC-25 wt-%Co. Powder Metallurgy, 23, (1980) 57-64.

51. J. Gurland. Microstructural aspects of the strength and hardness of cemented tungsten carbide, Brown University USA, (1969).

52. S. Luyckx and A. Love. The dependence of the contiguity of WC on Co content and its independence from WC grain size in WC-Co alloys. International Journal of Refractory Metals and Hard Materials, 24, (2006) 75-79.

53. B. Aronsson. Influence of processing on properties of cemented carbide. Powder Metallurgy, 30, (1987) 175 – 181.

54. J.H. Westbrook and E.R. Stover. High Temperature Materials and Technology, (I. E. Champbell, and E. M. Sherwood, eds.), John Wiley, and Sons, Inc., N. Y., p. 312 (1967).

55. S. Palmqvist. A method of determining the toughness of brittle materials, especially hardmetals. Jernkont. Ann., 141, (1957) 300-307.

56. K.J.A. Brookes. Hardmetals and other Hard Materials, International Carbide Data, Hertfordshire, UK (1975).

57. B. Roebuck and E.A. Almond. Recent Advances in Hardmetal Production, MPR Publications, Shrewsbury, UK (1979).

58 S.B. Luyckx. Precision matching of mating fracture surface of WC-Co Alloys. Fracture, ICF4, 2, (1977) 223-227.

59. B. Wittmann, W. Schubert and B. Lux. WC grain growth and grain growth inhibition in nickel and iron binder hardmetals. International Journal of Refractory Metals Hard Materials, 20, (2002) 51-60.

60. G.A. Good. Symposium on Quality Control and Production Processing in Powder Metallurgy (1970).

61. I.M. Hutchings. Tribology: Friction and wear of engineering materials, Edward Arnold, Cambridge, (1992).

62. D. Kopeliovich. Mechanisms of wear, Substance and Technology website, 2016. [Online]. Available from: http://www.substech.com. [Accessed 15 September 2016].

63. D.G.F. O'Quigley, S. Luyckx and M.N. James. An empirical ranking of a wide range of WC-Co grades in terms of their abrasion resistance measured by the ASTM Standard B611-85 test. International Journal of Refractory Metals and Hard Materials, 15, (1997) 73-79.

64. J. Larsen-Basse. Abrasive wear of tungsten carbide-cobalt composites. I. Rotary drilling tests. Journal of Material Science and Engineering, 13, (1974) 83-91.

65. J. Larsen-Basse. Wear of hard-metals in rock drilling: a survey of literature. Powder Metallurgy, 16, (1973) 1-32.

66. J. Larsen-Basse. Effect of composition, microstructure and service conditions on the wear of cemented carbides. Physical and Mechanical Metallurgy, 35, (1983) 35-42.

67. Adamas Carbide Corporation, Some Plain Talk about Carbides, American Machinist, (May 1978).

68. ISO 3878, Hardmetals – Vickers hardness test. 1983.

69. C.G. Ryan, D.N. Jamieson, C.L. Churms and J.V. Pilcher, A new method for on-line true elemental imaging using PIXE and the proton microprobe. Nuclear Instruments and Methods B, 104, (1995) 157 – 65.

70. ASTM B610-08. Standard test method for measuring dimensional changes associated with processing metal powders.

71. ASTM B311-08. Standard Test Method for Density of Powder Metallurgy (PM) Materials Containing Less Than Two Percent Porosity, (2008).

72. ASTM 373-88. Standard Test Method for Water Absorption Bulk Density Apparent Porosity and Apparent Specific Gravity of Fired Whiteware Product, (1955).

73. BS EN ISO 3326. Hardmetals - Determination of (the magnetization) coercivity, (2013).

74. J. Gurland. Practical applications of quantitative metallography. American Society for Testing Materials, Philadelphia (1984) 65.

75. R. Spiegler, S. Schmauder and S.S. Lorenz. Fracture toughness of WC-Co alloys by indentation. Journal of Hard Materials, 1 (3), (1990) 147 -158.

76. R.L. Smith and G.E. Sandland. An Accurate Method of Determining the Hardness of Metals, with Particular Reference to Those of a High Degree of Hardness, Process Instrumentation for Mechanical Engineering,1, (1922) 623–641.

77. ASTM E18-03E1. Rockwell Hardness and Rockwell Superficial Hardness of Metallic Materials (1932).

78. R Warren and H.J. Matzke, Proceedings of First International Conference on Science of Hard Materials (RK Viswanadham, D.J. Rowcliffe and J. Gurland, eds), Plenum Press, New York (1981), p. 563-582.

79. ASTM G105-02. 2002. Standard Test for Conducting Wet Sand/Rubber Wheel Abrasion Tests. ASTM International, West Conshohocken, NJ (2002).

80. N.B.S. Magagula, N. Sacks, and I. Botef, Slurry abrasion of WC-4wt%Ni coldsprayed coatings in synthetic minewater. The Journal of the Southern African Institute of Mining and Metallurgy, 116, (2016) 333-337.

81. T. Yamaguchi, and M. Okada. Formation of lamellar structures in the reaction between cemented tungsten carbide and molten zinc. Journal of the American Ceramic Society, 61, (1978) 529.

82. J. Qvick. Method of making cemented carbide powder with low sintering shrinkage and the powder obtained. US Patent. 20100260641 A1. 2010.

83. W. Lengauer and K. Dreyer. Tailoring hardness and toughness gradients in functional gradient hardmetals (FGHMS). International Journal of Refractory Metals and Hard Materials, 24, (2006) 155-161.

84. D. Bolton and R.J. Keely. Fracture toughness of cemented carbides. International Journal of Refractory Metals and Hard Materials, 1, (1982) 103.

85. R.I. Blombery, C.M. Perrot and P.M. Robinson. Abrasive wear of tungsten carbide-cobalt composites. I. Wear mechanisms, Materials Science and Engineering, 13, (1974) 93-100.

86. M.G. Gee, A. Gant and B. Roebuck. Wear mechanisms in abrasion and erosion of WC/Co and related hardmetals. Wear, 263, (2007) 137-148.

87. A.J. Gant and M.G. Gee. Abrasion of tungsten carbide hardmetals using hard counterfaces. International Journal of Refractory Metals and Hard Materials, 24, (2006) 189-198.

88. C.N. Machio. Preparation, Characterization and Testing of WC-VC-CO HP/HVOF Thermal Spray Coatings. PhD Thesis, University of Witwatersrand, 2005.

# Appendices

## Appendix A: Characterization of recycled oversize particles

**Table A1** Vickers hardness measurements for the recycled oversize particles.

| **Trial** | **$HV_{30}$** |
|---|---|
| 1 | 771.4 |
| 2 | 616.8 |
| 3 | 619.6 |
| 4 | 635.2 |
| 5 | 621.4 |
| **Average** | **653.3 ± 66.4** |

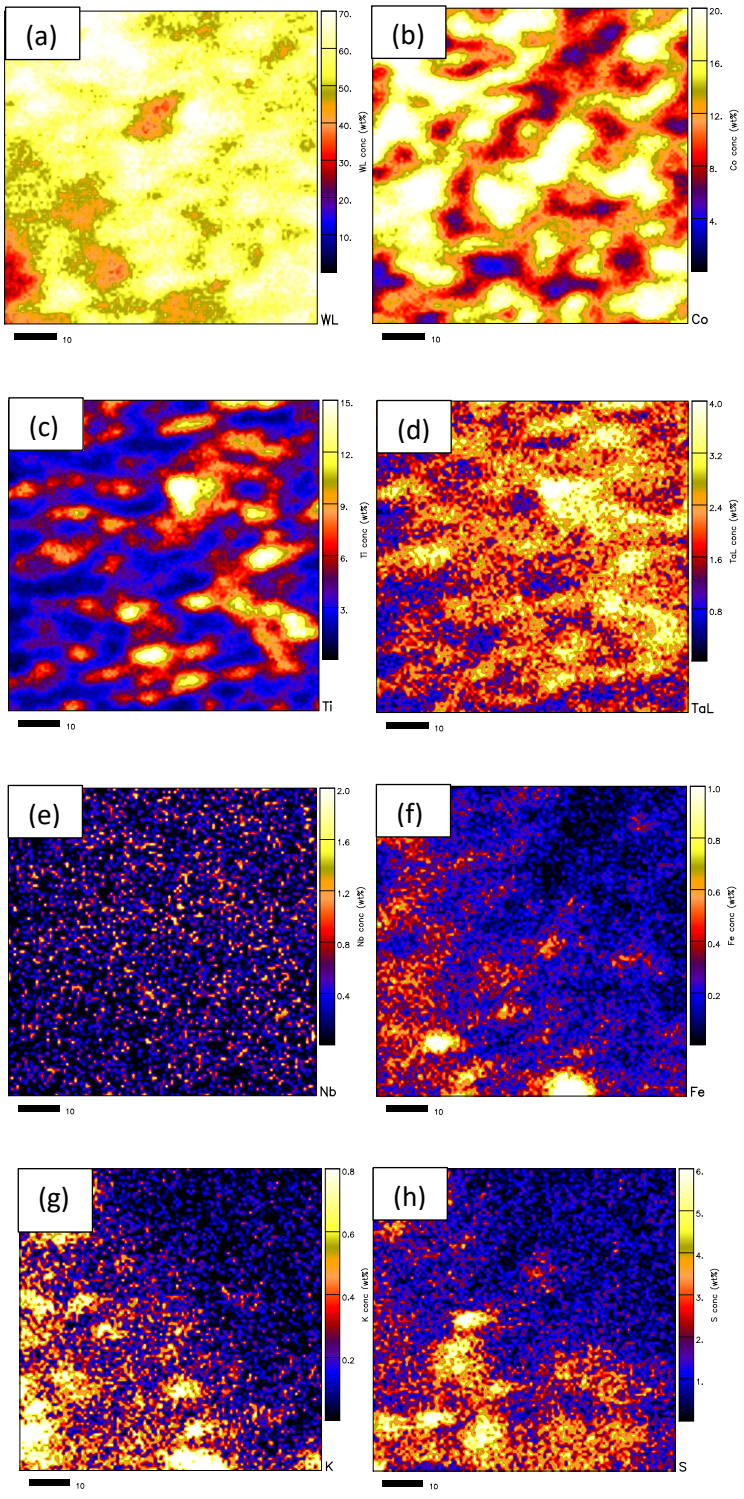



**Figure A1** Micro-PIXE elemental distribution maps of $W_L$, Co, Ti, $Ta_L$, Nb, Fe, K, S and Ca in an area towards the centre of the oversize particle. Light areas show regions of high elemental concentration, while dark areas show regions of low elemental concentration.

## Appendix B: Particle size distribution of milled powders

**Table B1** Particle size distribution of powders

| | % Passing | | | |
|---|---|---|---|---|
| **Particle size/µm** | **NS** | **N** | **R** | **RA** |
| 7.78 | 100 | - | | |
| 6.54 | 99.51 | 100 | 100 | 100 |
| 5.50 | 98.39 | 99.46 | 99.77 | 99.39 |
| 4.62 | 96.24 | 98.21 | 98.8 | 98.44 |
| 3.89 | 92.67 | 95.63 | 96.32 | 96.83 |
| 3.27 | 87.38 | 90.79 | 90.93 | 90.78 |
| 2.75 | 80.17 | 82.76 | 81.33 | 85.36 |
| 2.312 | 71.32 | 71.69 | 67.97 | 77.36 |
| 1.944 | 62.05 | 59.94 | 53.96 | 67.03 |
| 1.635 | 53.59 | 50.05 | 42.46 | 56.58 |
| 1.375 | 46.80 | 42.97 | 34.41 | 48.03 |
| 1.156 | 41.47 | 37.84 | 28.82 | 41.71 |
| 0.972 | 36.89 | 33.47 | 24.34 | 36.56 |
| 0.871 | 32.22 | 28.79 | 19.92 | 31.33 |
| 0.687 | 26.57 | 22.83 | 14.68 | 24.9 |
| 0.578 | 19.34 | 15.3 | 8.65 | 16.94 |
| 0.486 | 11.42 | 7.79 | 3.47 | 9.1 |
| 0.409 | 5.27 | 2.85 | 0.8 | 3.84 |
| 0.344 | 2.05 | 0.73 | 0 | 1.4 |
| 0.289 | 0.71 | 0 | | 0.43 |
| 0.243 | 0.13 | - | | 0 |
| 0.204 | 0 | - | | |

## Appendix C: Characterization of green compacts

**Table C1** Dimensions of green compacts.

| | | Mass/g | Length/mm | Width/mm | Thickness/mm | Green density ($gcm^{-3}$) |
|---|---|---|---|---|---|---|
| **NS** | **1** | 8.855 | 15 | 15 | 5.23 | 7.525 |
| | **2** | 9.0825 | 15 | 15 | 5.28 | 7.645 |
| | **3** | 9.0023 | 15 | 15 | 5.37 | 7.451 |
| | **4** | 8.9053 | 15 | 15 | 5.32 | 7.440 |
| | **5** | 8.9399 | 15 | 15 | 5.24 | 7.583 |
| | **Ave** | | | | | **7.529** |
| | **Stdv** | | | | | **0.087** |
| | | | | | | |
| **N** | **1** | 9.8039 | 15 | 15 | 5.51 | 7.908 |
| | **2** | 9.5631 | 15 | 15 | 5.48 | 7.756 |
| | **3** | 9.9675 | 15 | 15 | 5.58 | 7.939 |
| | **4** | 9.5668 | 15 | 15 | 5.49 | 7.745 |
| | **5** | 9.8795 | 15 | 15 | 5.57 | 7.883 |
| | **Ave** | | | | | **7.846** |
| | **Stdv** | | | | | **0.090** |
| | | | | | | |
| **R** | **1** | 9.5816 | 15 | 15 | 5.49 | 7.757 |
| | **2** | 9.9839 | 15 | 15 | 5.62 | 7.896 |
| | **3** | 9.5993 | 15 | 15 | 5.52 | 7.729 |
| | **4** | 9.9693 | 15 | 15 | 5.64 | 7.856 |
| | **5** | 9.1544 | 15 | 15 | 5.44 | 7.479 |
| | **Ave** | | | | | **7.743** |
| | **Stdv** | | | | | **0.163** |
| | | | | | | |
| **RA** | **1** | 8.0559 | 15 | 15 | 5.2 | 6.885 |
| | **2** | 7.7587 | 15 | 15 | 5.17 | 6.67 |
| | **3** | 7.6969 | 15 | 15 | 5.15 | 6.642 |
| | **4** | 7.7982 | 15 | 15 | 5.19 | 6.678 |
| | **5** | 8.1025 | 15 | 15 | 5.21 | 6.912 |
| | **Ave** | | | | | **6.757** |
| | **Stdv** | | | | | **0.130** |

## Appendix D: Characterization of sintered samples

**Table D1** Dimensions of green and sintered samples

| | | Green height/mm | Sinter height/mm | % Shrinkage |
|---|---|---|---|---|
| **NS** | **1** | 5.23 | 4.27 | 22.48 |
| | **2** | 5.28 | 4.35 | 21.38 |
| | **3** | 5.32 | 4.30 | 23.72 |
| | **4** | 5.24 | 4.27 | 22.72 |
| | **5** | 5.22 | 4.26 | 22.54 |
| | **Ave** | | | **22.568** |
| | **Stdv** | | | **0.832177866** |
| | | | | |
| **N** | **1** | 5.51 | 4.58 | 20.31 |
| | **2** | 5.48 | 4.48 | 22.32 |
| | **3** | 5.58 | 4.65 | 20 |
| | **4** | 5.58 | 4.62 | 20.78 |
| | **5** | 5.57 | 4.65 | 19.78 |
| | **Ave** | | | **20.638** |
| | **Stdv** | | | **1.012432714** |
| | | | | |
| **R** | **1** | 5.49 | 4.54 | 20.93 |
| | **2** | 5.62 | 4.69 | 19.83 |
| | **3** | 5.52 | 4.55 | 21.32 |
| | **4** | 5.64 | 4.65 | 21.29 |
| | **5** | 5.55 | 4.58 | 21.18 |
| | **Ave** | | | **20.91** |
| | **Stdv** | | | **0.622936594** |
| | | | | |
| **RA** | **1** | 5.20 | 4.23 | 22.93 |
| | **2** | 4.39 | 3.60 | 21.94 |
| | **3** | 4.16 | 3.48 | 19.54 |
| | **4** | 4.00 | 3.26 | 22.70 |
| | **5** | 4.21 | 3.50 | 20.29 |
| | **Ave** | | | **21.48** |
| | **Stdv** | | | **1.498515933** |

**Table D2** Density measurements of sintered samples

| $g/cm^3$ | NS | N | R | RA |
|---|---|---|---|---|
| 1 | 13.58 | 13.45 | 13.62 | 13.51 |
| 2 | 13.58 | 13.56 | 13.67 | 13.61 |
| 3 | 13.54 | 13.55 | 13.59 | 13.54 |
| 4 | 13.54 | 13.56 | 13.7 | 13.57 |
| 5 | 13.58 | 13.45 | 13.61 | 13.54 |
| **AVE** | **13.564** | **13.514** | **13.638** | **13.554** |
| **STDV** | **0.021909** | **0.058566** | **0.045497** | **0.037815** |

**Table D3** Volume percent open porosity of sintered samples

| | **Wet mass(W2)/g** | **Submerged mass (W3) /g** | **Dry mass (W1)/g** | **W2 - W1 /g** | **W2 - W3 /g** | **% porosity** |
|---|---|---|---|---|---|---|
| NS1 | 11.8027 | 10.9201 | 11.7994 | 0.0033 | 0.8826 | 0.373895 |
| NS2 | 8.674 | 8.0302 | 8.6708 | 0.0032 | 0.6438 | 0.497049 |
| NS3 | 8.7077 | 8.0596 | 8.7051 | 0.0026 | 0.6481 | 0.401173 |
| **AVE** | | | | | | **0.424039** |
| **STDV** | | | | | | **0.064683** |
| | | | | | | |
| N1 | 9.8094 | 9.0809 | 9.8063 | 0.0031 | 0.7285 | 0.425532 |
| N2 | 9.3731 | 8.6806 | 9.3712 | 0.0019 | 0.6925 | 0.274368 |
| N3 | 9.6829 | 9.0084 | 9.6805 | 0.0024 | 0.6745 | 0.355819 |
| **AVE** | | | | | | **0.351906** |
| **STDV** | | | | | | **0.075658** |
| | | | | | | |
| R 1 | 9.6888 | 8.9771 | 9.6866 | 0.0022 | 0.7117 | 0.309119 |
| R 2 | 8.8973 | 8.1854 | 8.8945 | 0.0028 | 0.7119 | 0.393314 |
| R 3 | 9.5232 | 8.8404 | 9.5216 | 0.0016 | 0.6828 | 0.234329 |
| **AVE** | | | | | | **0.312254** |
| **STDV** | | | | | | **0.079539** |
| | | | | | | |
| RA1 | 2.9342 | 2.2527 | 2.931 | 0.0032 | 0.6815 | 0.469552 |
| RA2 | 13.7833 | 12.7671 | 13.7796 | 0.0037 | 1.0162 | 0.364102 |
| RA3 | 7.0986 | 6.5745 | 7.0952 | 0.0034 | 0.5241 | 0.648731 |
| **AVE** | | | | | | **0.494128** |
| **STDV** | | | | | | **0.143897** |

Volume percentage open porosity = $\frac{W_2 - W_1}{W_2 - W_3}$ x 100.

## Appendix E: Silica sand characterization

To determine the average particle size of the sand, sieve analysis was carried out using a range of sieves from 750 μm to 75 μm. The morphology and average particle size of the sand particles was determined using a Carl Zeiss Sigma field emission scanning electron microscope (FESEM) at 15 keV in the backscattered mode (BSE). To improve the conductivity of the silica sand particles and the quality of the images, the sand particles were first coated with palladium-gold. Figure E1 shows the morphology of the sand particles, while Table E1 and Figure E2 summarize the particle size distribution.

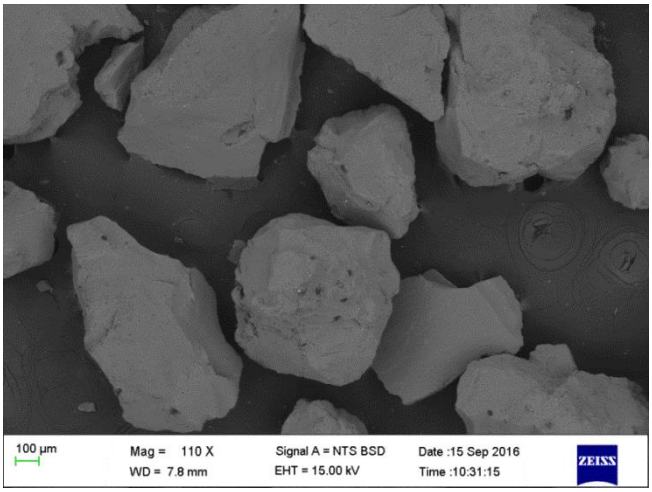



**Figure E1**: FESEM micrograph of silica sand used for slurry abrasion.

**Table E1** Sand particle size distribution from seive analysis

| Seive size (μm) | % mass |
|---|---|
| 750 | 0.00 |
| 500 | 42.47 |
| 425 | 26.22 |
| 300 | 21.14 |
| 212 | 6.29 |
| 150 | 2.11 |
| 106 | 0.58 |
| 90 | 0.07 |
| 75 | 0.05 |
| <75 | 0.09 |

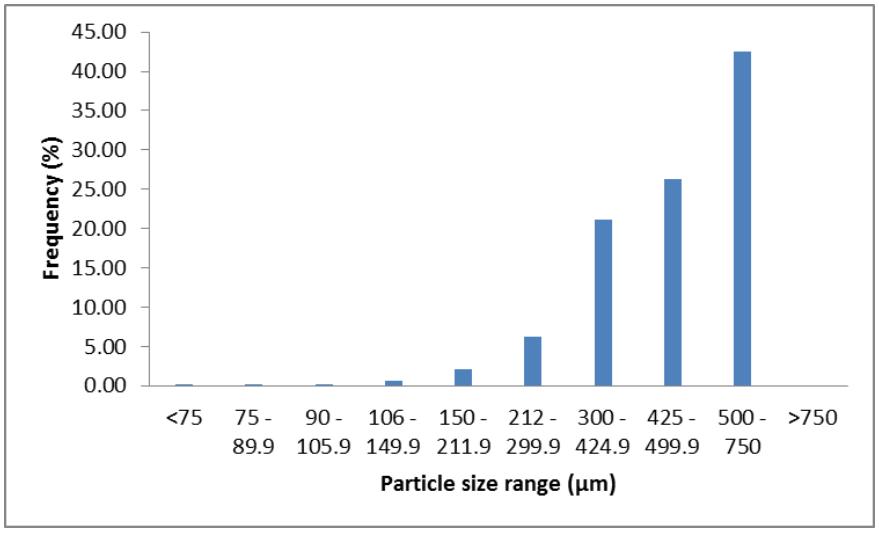



**Figure E2** Silica Sand particle size distribution fron seive analysis.

The ratio of the hardness of the silica sand ($H_a$) to that of the alloys ($H_s$) is shown in Table E2.

**Table E2** Ratio of hardness of silica sand to that of the alloys

| **Alloy** | **$H_a/H_s$** |
|---|---|
| NS | 0.677 |
| N | 0.675 |
| R | 0.674 |
| RA | 0.693 |

## Appendix F: Raw data of mass loss in slurry abrasion tests

**Table F1** Slurry abrasion mass losses for the un-recycled alloy NS and N

| **Time (min)** | **Mass losses (mg)** | | | | | |
|---|---|---|---|---|---|---|
| | **NS** | | | **N** | | |
| | **1** | **2** | **3** | **1** | **2** | **3** |
| 0 | 0 | 0 | 0 | 0 | 0 | 0 |
| 30 | 3.1 | 5.0 | 3.0 | 3.9 | 3.1 | 3.2 |
| 60 | 7.2 | 8.2 | 4.1 | 6.1 | 6.0 | 6.3 |
| 90 | 11.1 | 16.1 | 10.1 | 11.2 | 12.1 | 11.9 |
| 120 | 16.3 | 19.0 | 12.2 | 15.4 | 16.3 | 15.3 |
| 150 | 26.1 | 22.2 | 16.1 | 21.1 | 23.1 | 22.1 |
| 180 | 30.2 | 25.1 | 19.3 | 24.2 | 25.9 | 26.4 |
| 210 | 35.1 | 38.1 | 27.2 | 30.0 | 31.0 | 29.8 |
| 240 | 43.0 | 43.1 | 29.3 | 35.1 | 36.2 | 37.1 |

**Table F2** Slurry abrasion mass losses for the recycled alloys R and RA

| **Time (min)** | **Mass losses (mg)** | | | | | |
|---|---|---|---|---|---|---|
| | **R** | | | **RA** | | |
| | **1** | **2** | **3** | **1** | **2** | **3** |
| 0 | 0 | 0 | 0 | 0 | 0 | 0 |
| 30 | 3.1 | 2.4 | 4.8 | 2.3 | 3.1 | 2.9 |
| 60 | 6.0 | 6.3 | 7.6 | 8.7 | 9.1 | 9.0 |
| 90 | 11.2 | 11.1 | 12.2 | 11.9 | 12.4 | 14.1 |
| 120 | 19.3 | 15.4 | 16.3 | 19.1 | 22.1 | 24.1 |
| 150 | 23.1 | 26.0 | 25.1 | 27.8 | 27.3 | 29.8 |
| 180 | 27.2 | 29.1 | 31.9 | 32.4 | 31.3 | 32.3 |
| 210 | 31.1 | 32.9 | 35.2 | 36.3 | 35.2 | 37.1 |
| 240 | 35.7 | 38.1 | 39.7 | 43.0 | 42.9 | 46.7 |

s